Skoltech

Skolkovo Institute of Science and Technology

Skolkovo Institute of Science and Technology

CATHODE MATERIALS FOR METAL-ION BATTERIES BASED ON
ORTHOBORATE AND ORTHOPHOSPHATE

Doctoral Thesis

by

IVAN V. TERESHCHENKO

DOCTORAL PROGRAM IN MATERIALS SCIENCE AND ENGINEERING

Supervisor
Professor Artem M. Abakumov

Moscow - 2020

I hereby declare that the work presented in this thesis was carried out by myself at Skolkovo Institute of Science and Technology, Moscow, except where due acknowledgement is made, and has not been submitted for any other degree.

Candidate (Ivan V. Tereshchenko)

Supervisor (Prof. Artem M. Abakumov)

Abstract

Nowadays metal-ion batteries (MIB) look as one of the most promising option for electrical energy storage. Still, raising of their specific energy is an actual problem to solve. $LiCoBO_3$ represents an example of a cathode material with high theoretical energy density (>800 W*h/kg) but not achieved practically, and clarification of the reasons for that is a useful contribution to the field. The investigation of layered fluoride-phosphates of sodium and cobalt with formula Na_2MPO_4F (M=Co, Mn and others) is another direction for creation of next generation batteries with high energy density. Thus, techniques of combined solvo-hydrothermal synthesis for reproducible synthesis of cathode materials based on $LiCoBO_3$ and Na_2CoPO_4F have been proposed for the first time; synthesis and qualitative analysis of phase composition of $Na_2Co_{1-x}Mn_xPO_4F$ (x=0.2, 0.4, 0.6, 0.8) samples has been conducted. $Na_2Co_{1-x}Mn_xPO_4F$ (x=0.2, 0.4) samples were shown to adopt a layered structure similarly to Na_2CoPO_4F which leaves a certain direction for further research.

The theoretical insights in structure transformations in polyanion electrode materials help to better understand their behavior in MIBs. Na_2FePO_4F is an appropriate model for investigation of the role of oxygen atoms which have no redox active element in their coordination sphere in both electrochemical cycling and chemical ion exchange of sodium for lithium. Thus, using *operando* powder X-ray diffraction, γ-resonance spectroscopy with [57]Fe nuclei and density functional theory calculations the mechanism of cycling of $(Na,Li)_{2-x}FePO_4F$ has been described, and an explanation of the strong monotonic dependence of the deintercalation potential on x throughout the whole

compositional range $0 \leq x \leq 1$ was proposed. A novel electrochemical cell with single crystal sapphire windows has been successfully applied to drastically lessen the contribution of X-ray windows into synchrotron X-ray powder diffraction patterns. Mechanisms of cycling of Na_2FePO_4F and Na_2CoPO_4F in a sodium-ion half-cell have been clarified using synchrotron X-ray powder diffraction; structures of $Na_{1.55}FePO_4F$, $Na_{1.44}CoPO_4F$ and $NaCoPO_4F$ have been characterized.

Finally, a novel cathode material with formula $K_6(VO)_2(V_2O_3)_2(PO_4)_4(P_2O_7)$ was found to be a hypothetical alternative to $KVPO_4F$ and $KVOPO_4$. Using powder X-ray diffraction, a reversible electrochemical deintercalation of potassium from polycrystalline $K_6(VO)_2(V_2O_3)_2(PO_4)_4(P_2O_7)$ has been demonstrated; the obtained material has demonstrated more than 50% of the theoretical capacity of 88 mAh/g with the volume change not exceeding 0.9%. Using DFT+U approach the potassium diffusion barriers were estimated for basic crystallographic directions of the $K_6(VO)_2(V_2O_3)_2(PO_4)_4(P_2O_7)$ structure and the barrier for the direction b has been found to be below 0.31 eV. Though the theoretical specific capacity of $K_6(VO)_2(V_2O_3)_2(PO_4)_4(P_2O_7)$ is lower by a third than the same of $KVOPO_4$, the residual potassium in the former may positively affect chemical stability of the fully charged cathode towards the electrolyte.

List of Articles

1. Oleg A. Drozhzhin, Ivan V. Tereshchenko, Evgeny V. Antipov. Novel synthetic approaches to $LiCoBO_3$ cathode material and its electrochemical properties. Ceramics International, vol. 43, № 5, pp. 4670-4673 (2017). Available from https://www.sciencedirect.com/science/article/pii/S0272884216324178;

2. Ivan V. Tereshchenko, Dmitry A. Aksyonov, Oleg A. Drozhzhin, Igor A. Presniakov, Alexey V. Sobolev, Andriy Zhugayevych, Daniil Striukov, Keith J. Stevenson, Evgeny V. Antipov, Artem M. Abakumov. The Role of Semilabile Oxygen Atoms for Intercalation Chemistry of the Metal-Ion Battery Polyanion Cathodes. Journal of the American Chemical Society, vol. 140, № 11, pp. 3994-4003 (2018). Available from https://pubs.acs.org/articlesonrequest/AOR-YJh64uPKIstIQxXrxm5f;

3. Oleg A. Drozhzhin, Ivan V. Tereshchenko, Hermann Emerich, Evgeny V. Antipov, Artem M. Abakumov, Dmitry Chernyshov. An electrochemical cell with sapphire windows for operando synchrotron X-ray powder diffraction and spectroscopy studies of high-power and high-voltage electrodes for metal-ion batteries. Journal of Synchrotron Radiation, vol. 25, № 2, pp. 468-472 (2018). Available from https://journals.iucr.org/s/issues/2018/02/00/ve5080/index.html;

4. Ivan V. Tereshchenko, Dmitry A. Aksyonov, Andriy Zhugayevych, Evgeny V. Antipov, Artem M. Abakumov. Reversible electrochemical potassium deintercalation from >4V positive electrode material $K_6(VO)_2(V_2O_3)_2(PO_4)_4(P_2O_7)$. Solid State Ionics, vol. 357, p. 115468 (2020). Available from https://www.sciencedirect.com/science/article/abs/pii/S0167273820305221.

List of Conferences

1. Ivan V. Tereshchenko, Gregory A. Skorupsky, Oleg A. Drozhzhin, Nellie R. Khasanova, Evgeny V. Antipov. Hydrothermal synthesis of sodium and transition metals fluorophosphates as cathode materials for lithium- and sodium-ion batteries (Poster). International Conference "Condensed Matter Research at the IBR-2", Dubna, Moscow Oblast, Russia (2015);

2. Ivan V. Tereshchenko, Gregory A. Skorupsky, Oleg A. Drozhzhin, Nellie R. Khasanova, Evgeny V. Antipov. Катодные материалы для литий- и натрий-ионных аккумуляторов на основе фторидофосфатов натрия и переходных металлов, синтезированных гидротермальным методом (Poster). XIV Конференция молодых ученых "Актуальные проблемы неорганической химии: перспективные методы синтеза веществ и материалов", Zvenigorod, Russia (2015);

3. Ivan V. Tereshchenko. Синтез сольвотермальным методом и исследование электрохимических характеристик фторидофосфатов Na2MPO4F (M=Fe, Co) (Talk). XXIII International scientific conference of students and young scientists "Lomonosov-2016", Moscow, Russia (2016);

4. Oleg A. Drozhzhin, Vasily D. Sumanov, Ivan V. Tereshchenko, Anastasiya D. Grebenszhikova. Phase transformations behavior during operation of the phosphate and fluoride-phosphate cathode materials for Li(Na)-ion batteries (Talk). XIV International Conference "Topical Problems of Energy Conversion in Lithium Electrochemical Systems" (2016);

5. Ivan V. Tereshchenko, Gregory A. Skorupsky, Oleg A. Drozhzhin, Evgeny V. Antipov. Hydro- and solvothermal synthesis of Na2FePO4F as cathode materials for lithium- and sodium-ion batteries (Poster). XIV International Conference "Topical Problems of Energy Conversion in Lithium Electrochemical Systems", Suzdal, Russia (2016);

6. Ivan V. Tereshchenko, Gregory A. Skorupsky, Oleg A. Drozhzhin, Evgeny V. Antipov. Hydro- and solvothermal synthesis of Na2FePO4F as cathode materials for lithium- and sodium-ion batteries (Poster). 67th Annual Meeting of the International Society of Electrochemistry, The Hague, Netherlands (2016);

7. Ivan V. Tereshchenko. "Гидротермальный синтез катодных материалов на основе фторидофосфата натрия и переходных металлов для натрий-ионных аккумуляторов» (Talk). The conference of the Department of Electrochemistry, Lomonosov Moscow State University, Moscow, Russia (2017);

8. Ivan V. Tereshchenko, Oleg A. Drozhzhin, Igor A. Presniakov, Aleksei V. Sobolev, Daniil V. Striukov, Andriy Zhugayevych, Keith Stevenson, Evgeny V. Antipov, Artem M. Abakumov, Dmitry A. Aksyonov. The role of "dangling" oxygen atoms for intercalation chemistry of the metal-ion battery polyanion cathodes in the case of Na_2FePO_4F (Talk). 5th International Conference on Nanomaterials and Advanced Energy Storage Systems, Astana, Kazakhstan (2017);

9. Ivan V. Tereshchenko, Oleg A. Drozhzhin, Igor A. Presniakov, Aleksei V. Sobolev, Daniil V. Striukov, Andriy Zhugayevych, Keith Stevenson, Evgeny V. Antipov, Artem M. Abakumov, Dmitry A. Aksyonov. The role of "dangling" oxygen atoms

for intercalation chemistry of the metal-ion battery polyanion cathodes in the case of Na2FePO4F (Poster). II International Conference of Young Scientists "Topical Problems of Modern Electrochemistry and Electrochemical Materials Science", Vozdvizhenskoe park hotel, Russia (2017);

10. Evgeny V. Antipov, Oleg A. Drozhzhin, Ivan V. Tereshchenko, Vasily D. Sumanov, Maxim V. Zakharkin, Igor A. Presnyakov, Alexey V. Sobolev, Artem M. Abakumov. Non-equilibrium phase transitions in electrode materials of metal-ion batteries studied by operando diffraction and spectroscopic techniques (Invited talk). III Baikal Materials Science Forum, Ulan-Ude and v. Goryachinsk, Lake Baikal, Russia (2018);

11. Ivan V. Tereshchenko. Comprehensive structural investigation of layered fluoride-phosphates A2MPO4F (A=Na, Li; M=Fe, Co, Mn, Mg) (Poster). XV International Conference "Topical problems of energy conversion in lithium electrochemical systems", Saint Petersburg, Russia (2018);

12. Ivan V. Tereshchenko. Comprehensive structural investigation of layered fluoride-phosphates A2MPO4F (A=Na, Li; M=Fe, Co, Mn, Mg) (Poster). III International Conference of Young Scientists "Topical Problems of Modern Electrochemistry and Electrochemical Materials Science", Vozdvizhenskoe park hotel, Russia (2018).

Table of contents

Acknowledgements

List of abbreviations

DEGDME – diethylene glycol dimethyl ether

DFT – density functional theory

DMC – dimethyl carbonate

EC – ethylene carbonate

EDX – energy-dispersive X-ray

FE-SEM – field emission scanning electron microscope

HFP – hexafluoropropylene

ICP-MS – inductively coupled plasma mass spectrometry

LIB – lithium-ion battery

NEB – nudge elastic band

PAA – polyacrylate

PC – propylene carbonate

PEO – polyethylene oxide

PEDA – polyester diacrylate

PEG – polyethylene glycol

PEOMA – poly(ethylene oxide) methyl ether methacrylate

PMAA – poly(methacrylic acid)

PTFE – polytetrafluoroethylene

PVdF – polyvinylidene difluoride

PXRD – powder X-ray diffraction

RTIL – room temperature ionic liquid

SEI – solid electrolyte interface,

SEM – scanning electron microscope

SOC – states of charge

SXPD – synchrotron X-ray powder diffraction

TEGDME – tetraethylene glycol dimethyl ether

TFSI – N,N-bistrifluoromethane-sulphonamide anion $N(SO_2CF_3)_2^-$

V_{oc} – open-circuit potential

1. Literature review and formulation of the problem

1.1. Introduction

In connection with growing application of electrical transportation and of renewable energy (e.g. solar or wind energy), the problem of effective energy storage becomes more and more important in the modern world. Thanks to the intensive scientific research during seventies of the last century the concept of a lithium- and later the same of a lithium-ion battery (LIB) has emerged; the latter is the most widespread type of battery because of the following advantages: high specific energy (>250 W·h/kg) and energy density (>670 W·h/l), relatively good rate capability, low self-discharge and long cycle life (more than a thousand charge-discharge cycles with capacity fade less than 20%). In the present time LIBs are widely used both by consumers and industry, the latter including advanced power supply, transportation (air, marine and low-range public) and space satellites.

Industry of LIBs, which are the best among secondary batteries of multiple types, most probably will stop meeting growing requirements of the modern economy because of relative shortness of lithium supply in the world. That's why scientists look for new active compounds for electrode materials – based on sodium and potassium. Further development of electrochemical energy storage, particularly, of metal-ion batteries is a necessary step towards sustainable development.

The researchers' efforts are mainly directed to increasing specific energy of electrode materials in sodium-ion and potassium-ion batteries as well as in lithium-ion

ones, and this is mainly reached by increase of the specific coulombic charge available for reversible extraction, and by increase of the cell voltage (particularly by increase of the (de)intercalation potential of the cathode material). That's why search and complex investigation of new cathode materials for metal-ion batteries by itself is important for creation of the next generation of batteries. Thus, search of novel cathode materials for usage in sodium- or potassium-ion batteries was the goal of this work.

1.2. Overview of a lithium-ion battery

In general, electric battery is a device wherein the energy of chemical reaction turns into the electric energy. If this process is apparently or truly reversible, it can be repeated for many times and such electric battery is called secondary battery. Secondary batteries are used for accumulation of electrical energy and autonomous power supply of miscellaneous electrical devices and equipment [1]. Electric battery represents a set of electrochemical cells connected in series or in parallel or in both modes, or just one cell; in the latter case the cell actually is not a battery, but the term battery is conventionally used for separate cells as well. Electrochemical cell consists of a positive electrode (cathode) and a negative electrode (anode) divided by a layer of electrolyte allowing migration of cations from anode to cathode (during discharge) and backwards (during recharge if the battery is secondary) [2]. Also, one could distinguish such necessary components as the separator which is a mechanical barrier between electrodes impregnated with electrolyte in some way, the anodic and cathodic current collectors with their terminals and, finally, cell casing. Apparently, academic papers focusing on these components are much less

numerous than ones devoted to the above-mentioned three key constituents which in popular literature are referred to as the battery "chemistry".

The most important characteristics of a secondary battery are the following: the cell voltage or the open circuit potential V_{oc} defined as the difference between the redox potentials of cathode and anode materials: $V_{oc}=E_c-E_a$; the capacity C and the specific energy $Q=C\cdot<V_{oc}>$ representing the gravimetric values of the stored coulombic charge and energy respectively; the cycle life which is expressed as the number of cycles with preservation of an arbitrary percentage of the initial energy storage capability (let say, 80%); the maximal discharge rate (rate 1C denotes the current density which discharges a battery from its fully charged state in one hour); the temperature ranges of charge and discharge; the self-discharge caused by side electrochemical processes on the electrodes with partial irreversible loss of active mass and the related capacity fade. An additional advantage from the perspective of commercial viability is the abundance of chemical elements constituting the active compounds of the battery electrodes.

Electrode materials of LIBs are characterized by a possibility of reversible intercalation/deintercalation of lithium ions. Reversibility here is an arbitrary notion implying that the electrode materials in very large extent satisfy the theoretical model in which they undergo oxidation and reduction without destruction of their crystal or molecular structure. A representative type of the most-widespread modern lithium-ion batteries (Figure 1) contains cathode material based on complex oxide (e.g. $LiCoO_2$ with a layered structure); graphite anode; thin ($\leq$20 microns) macroporous film of polyethylene or polypropylene called separator, which is necessary for prevention of a short circuitry

16

between cathode and anode; organic aprotic electrolyte which fills the near-electrode space and pores of the separator and allows lithium ions to migrate between two electrodes. Besides, a polymeric binder (e.g. polyvinylidene difluoride, PVdF) is used for attachment of the powder of graphite or $LiCoO_2$ to the current collectors of copper or aluminum foil, respectively.
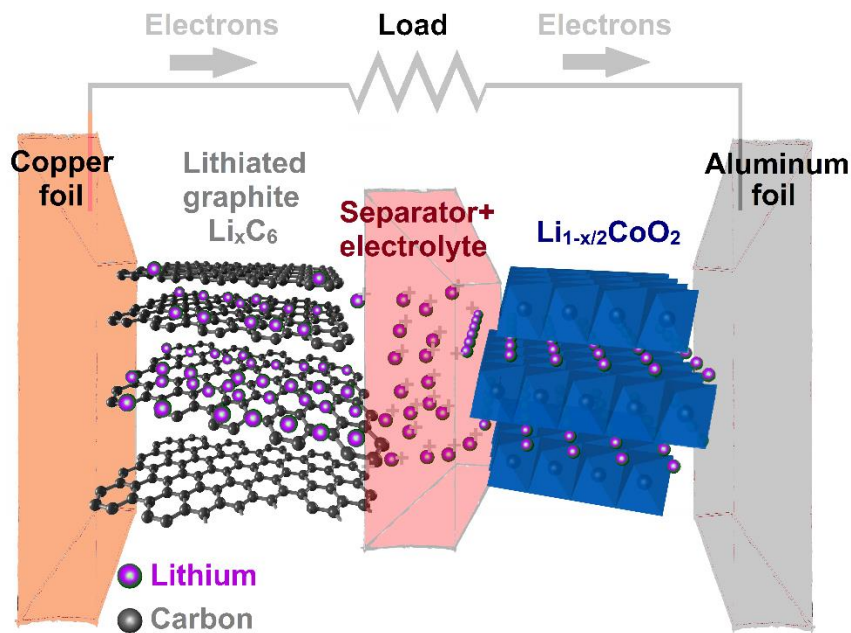
Figure 1. A schematic representation of a lithium-ion electrochemical cell during discharge.

On battery discharge electrons move from the graphite anode to the cathode as depicted by arrows in the Figure 1. Lithium ions inside the cell also move from the graphite anode to the $Li_{1-x/2}CoO_2$ cathode (x stands for the state of charge):

$$Li_xC_6 - xe^- = xLi^+ + 6C \text{ (anode)};$$

$$2 \cdot Li_{1-x/2}CoO_2 + xLi^+ + xe^- = 2 \cdot LiCoO_2 \text{ (cathode)}.$$
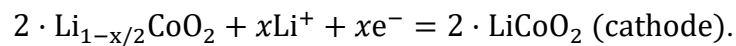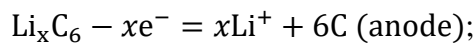
Upon charge the lithium ions and electrons move in the backward direction [3]. The electrochemical process in which the electrode of lithium cobaltite acts as the cathode begins when the difference between V_{oc} and the impedance of the electric circuit formed between battery current collectors (let it be denoted R) becomes positive; since this impedance is proportional to the impedance of the resulting circuit, and the dissipated power is roughly equal to $V_{oc}^2 \cdot R^{-1}$, the case of a short circuit (near-zero impedance) releases huge electrical energy in short time (ones or tens of seconds). This energy can be dissipated only as Joule heat, which often initiates so-called thermal runaway of a lithium-ion battery – a fire-hazardous condition and also sometimes a traumatic accident by itself. The electrochemical process in which the electrode with graphite acts as the cathode begins when the difference between the voltage applied between lithium cobaltite and graphite and V_{oc} becomes positive, i.e. electrode with $LiCoO_2$ has been connected to the positive terminal of the overwhelming voltage source and one with graphite has been connected to the negative terminal; this reverse electrochemical process is what is called charge or recharge of a battery.

If one describes deintercalation using a hypothetic phase diagram (Figure 2) where **A** is the lithium-depleted phase, **B** is the lithium-rich phase, **A** possessing a range of homogeneity α, **B** possessing the range of homogeneity γ, and at a specific Li content a compound is formed along with its homogeneity range β, then one can suppose co-existence of two different regimes of lithium (de)intercalation: two-phase one and single-phase one, depending on the position of the figurative point [4]. From the Gibbs' Phase Rule follows that the chemical potential of the system is constant when the figurative point

is located in the two-phase compositional ranges, or, in other words, until one of two coexisting compounds is exhausted. And when the figurative point appears to be located in a single-phase region (α or β or γ in the Figure 2, **left**), then from Gibbs' Phase Rule at constant temperature and pressure there is one degree of freedom, namely chemical potential depending on the composition (Figure 2, **right**). Then the electrode material can participate in a redox reaction without phase transitions which means absence of the phase boundary. The latter sometimes becomes a reason of kinetical difficulties for (de)intercalation, e.g. for $LiFePO_4$, which is described in the chapter on cathode materials for LIBs. In practice among metal-ion electrode materials one may encounter either one of two regimes or a combination of both depending on the chemical composition and the structure of the active compound.
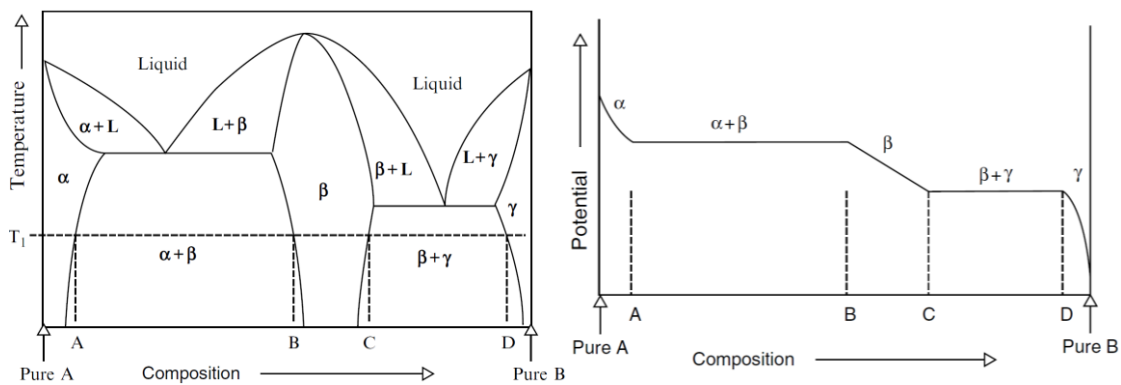
Figure 2. **Left** – hypothetical binary phase diagram AB at a constant pressure. **Right** – plot of dependence of the chemical potential of the system from the left figure on composition; reprinted by permission from Springer Nature: Springer Advanced Batteries Materials Science Aspects by Robert A. Huggins © 2009.

1.3. Electrolytes for lithium-ion batteries

Electrolyte is the component of an electrochemical cell responsible for migration of lithium ions from cathode to anode and vice versa. Besides abundance and environmental safety, electrolytes for all metal-ion batteries including lithium-ion ones should possess several functional features: ability to form an interface layer between electrolyte and electrodes with more or less constant composition and structure during cell cycling (this layer is called solid electrolyte interface, SEI); ionic conductivity $\sigma_{25°C}>10^{-4}$ S/cm (lg $\sigma_{25°C}>-4$) and the cation transference number closer to unity; high boiling and flash points (if flammable solvents are used); chemical stability towards charged electrodes at any temperature the battery is subjected to. SEI is a semi-solid film which is formed where electrolyte has contact with the surface of the charged electrodes. In the case of a LIB with graphite anode the film on the surface of graphite anode has thickness up to several tens nanometers and contains a whole series of compounds, which usually are amorphous Li_2O, LiF, Li_2CO_3, and polyolefins [5]. Alkaline metal cations from the electrolyte salt also are trapped in SEI film which imparts metal-ion diffusion to it.

Energy relations between the electrodes and the electrolyte are depicted in Figure 3. One can find in this figure the green area marking the absolute position and size of the "electrochemical stability window" of electrolyte; electrochemical potential of any electrode should fall into this window, otherwise electrolyte will be oxidized or reduced by the electrode. Usage of the term "electrochemical stability" instead of "chemical stability" is for underlying that the applied electric potential alone is capable of promoting chemical transformation of electrolyte or its reaction with any of two electrodes; such reactions

irreversibly change SEI and spend all compounds participating in these reactions. The window size is equal to the energy difference E_g between the lowest unoccupied molecular orbital (LUMO) and the highest occupied molecular orbital (HOMO) of the electrolyte; so those molecular orbitals are referred in the Figure 3. Besides, one can see in Figure 3 that the SEI is represented as a factor of apparent enlargement of the electrolyte stability window.
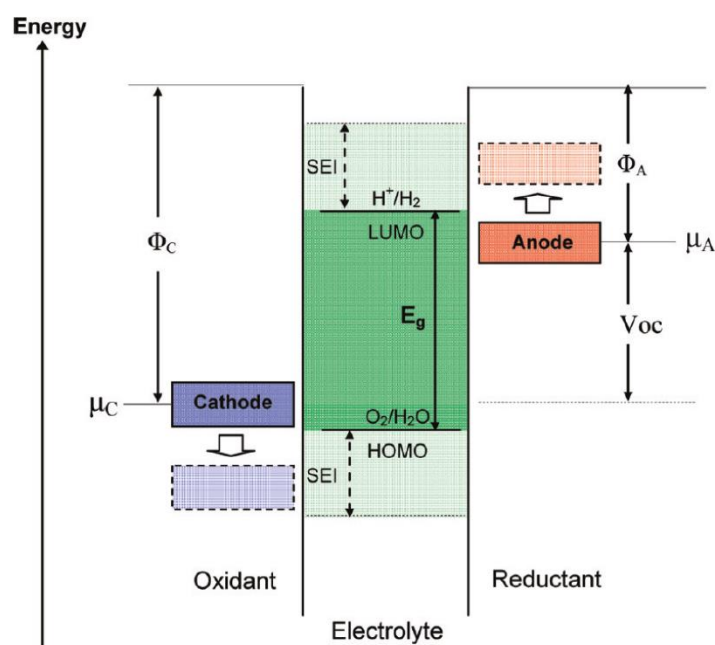
Figure 3. Diagram of the basic energy relations in an electrochemical cell [6]. Reprinted with permission from "Challenges for Rechargeable Li Batteries" // J. B. Goodenough, K. Youngsik, Chem. Mater., vol. 22, p. 587-603 (2010). Copyright 2010 American Chemical Society.

Actually, it was found long time ago that the SEI works as a mechanical barrier for solvent molecules [6], and this feature of the SEI is crucial for all modern metal-ion batteries with non-aqueous electrolytes. Ideally this enlargement is permanent for a specific

cell, but prolonged exposing to raised temperatures promotes degradation of the SEI eliminating its effect and spending electrolyte on the formation of renewed SEI [7]. The window enlargement because of the SEI can take place either from the upper side or from the lower side, and in the former case they say that an anodic reaction has occurred, a cathodic SEI has been formed and the anodic stability has been enhanced, and in the latter case they say that a cathodic reaction has occurred, an anodic SEI has been formed and the cathodic stability has been enhanced. Certainly, stability window may be enlarged from both upper and lower sides. Thus, for thermodynamic stability of electrolyte V_{oc} should not exceed energy difference E_g divided by elementary charge [6], and by means of SEI formation electrolyte can gain kinetic stability allowing such exceeding.

The actual composition of electrolyte in a modern lithium-ion battery depends on what type of battery is considered. Up to now there is no large-scale commercialization of batteries with inorganic or hybrid electrolytes. As scientific and technological problems of inorganic solid-state electrolytes are too far from the scope of the present work, there is no sense to focus on them and only constituents of the most widespread types of lithium-ion batteries will be shortly described. Electrolyte of any type of a commercialized battery consists of organic medium and lithium salt [6]. Organic medium is either a mixture of polymer with organic solvents introduced by wetting or swelling, or pure polymer (e.g. polyethylene oxide), or a mixture of polymers (both chemical and physical mixing methods are widespread [8]). If organic solvents contained in a battery wet the polymer, battery is called simply a "lithium-ion battery", and if the polymer is swollen instead of being wetted, or if there is no solvent at all, then such battery is called a "lithium polymer battery".

Lithium hexafluorophosphate LiPF$_6$ is the most widely used salt for LIBs, and some other salts (e.g. LiClO$_4$, LiBF$_4$ [9], lithium bis(oxalato)borate LiBOB [10], difluoro(oxalato)borate LiDFOB [11]) are considered as capable of forming slightly better SEI; selection of these compounds is explained mainly by their solubility in non-aqueous media having relatively low relative dielectric permittivity. Lithium N,N-bis(trifluoromethane)-sulphonamide LiN(SO$_2$CF$_3$)$_2$ (lithium TFSI or LiTFSI) is considered to be an expensive but promising option for the so-called high-voltage electrolytes [12] (the arbitrary demarcation between usual and high-voltage ones can be set at 4.5 V vs. Li/Li$^+$ [13]). Examples and main physical properties of some lithium salts are represented in Table 1, where a considerable dependence of ionic conductivity on the anion structure can be noticed. NaPF$_6$ and NaClO$_4$ are usually used for sodium-ion laboratory electrochemical cells and KPF$_6$ is most often used for potassium-ion cells.

Table 1. Properties of lithium salts in liquid organic electrolytes [9].

Anion	Melting point, °C	Decomposition temperature, °C	lg σ$_{25°C}$ of 1M solution in a mixture of EC and DMC (1:1 by vol.); [σ]=S/cm
BF$_4^-$	293	>100	−2.3
PF$_6^-$	200	~80	−2.0
AsF$_6^-$	340	>100	−2.0
ClO$_4^-$	236	>100	−2.1

Salts containing covalently bound halogens can undergo autocatalytic decomposition. For example, LiPF$_6$ can decompose into lithium fluoride LiF and phosphorous pentafluoride PF$_5$. The last one can easily react with carbonate esters and traces of protic compounds (water and alcohols) forming hydrogen fluoride. This leads to destruction of alumina passivation layer on the surface of aluminum current collectors,

further corrosive destruction of aluminum [14] () and even surface degradation of the oxide cathode. Different approaches for solution of the problem were suggested [15]: small amounts of hexamethyldisiloxane and tetraethyl orthosilicate [16], or of compounds with N–Si bond for binding HF; usage of separators made from quartz fibers; surface modification of $LiCoO_2$ with different ceramics (e.g. ZrO_2, Al_2O_3, SiO_2) for the sake of protection of its surface from acidic degradation. Decomposition of PF_5 can produce monofluorinated gaseous organic compounds, and that's why specific agents are introduced for complexation of PF_5 [15]: hexamethyl phosphorous triamide, dimethyl acetamide, etc.

Main solvents for metal-ion batteries are alkyl carbonates which have wide electrochemical stability window (1.6–4.8 V vs Li/Li^+) and moderate viscosity. If alkyl carbonate ester is cyclic, i.e. has a five-membered ring $-C(R_1R_2)-O-(C=O)-O-C(R_3R_4)-$, it acquires high relative permittivity, and, as a consequence, high viscosity (which is a disadvantage), high boiling point and the ability to dissolve electrolyte salts, the latter making cyclic carbonates a necessary component of a conventional lithium-ion electrolyte. The most-widespread carbonate solvent ethylene carbonate also facilitates SEI formation on the surface of graphite [17], which is important for prevention not only of reductive decomposition of electrolyte solvents but also of their occlusion into interlayer space of graphite [9]; non-cyclic carbonates are added to ethylene carbonate because of its high viscosity and melting point [18]. Some physical properties of carbonate esters and of γ-butyrolactone are represented in Table 2.

Table 2. Physical properties of main organic solvents used in commercial lithium-ion batteries and laboratory-scale metal-ion electrochemical cells [18],[19],[20]. Republished with permission of IOP Publishing from the Journal of The Electrochemical Society, vol. 147, №9, p. 3219 (2000); permission conveyed through Copyright Clearance Center, Inc.

Compound	Flash point, °C	Boiling point, °C	Melting point, °C	Relative permittivity ε	Viscosity, cP
Ethylene carbonate (EC)	160	248	36.4	89.8	1.90
Propylene carbonate (PC)	132	242	−48.8	64.9	2.53
Dimethyl carbonate (DMC)	18	90	4.6	3.1	0.59
Ethyl methyl carbonate (EMC)	27	107	−53	3.0	0.65
Diethyl carbonate (DEC)	31	126	−74.3	2.8	0.75
γ-butyrolactone (γ-BL)	98	204	−43.3	39.0	1.70

Among other types of solvents which have attracted much attention, sulfones [21] and dinitriles [22] should be distinguished. In turn, among aliphatic dinitriles the most attractive are glutaronitrile $NC(CH_2)_3CN$ with the melting point of −29°C, and widely available adiponitrile $NC(CH_2)_4CN$ with the flash point of 163°C [22], [23]. Sulfones and adiponitrile need to be mixed with other solvents of the same or another type in order to form an eutectic mixture and overcome the problem of high melting points [22], [24]. A remarkable drawback of sulfones and dinitriles is their high viscosity which is about 6 cP at 25°C for both ethyl methyl sulfone and adiponitrile. Their more serious drawback is low cathodic stability, which can hardly be overcome by SEI formation, especially for dinitriles [23]; but the outstanding anodic stability of sulfones has been attracting attention for almost

two decades in spite of their low cathodic stability, high melting points and viscosities [25]–[27].

Completely different liquids, which are capable of working simultaneously as solvents and salts also deserve some attention here. Actually, they are ionic salts with such low crystallization points that upon strong cooling they undergo a gradient transformation into a glassy ionic solid or into a liquid crystal instead of normal crystallization. They are called room temperature ionic liquids (RTILs) [28], and their ability to replace carbonate-based lithium electrolytes has been tested for more than a decade because of two remarkable advantages: wider stability window and dramatically lower flammability [28]. Up to now their main drawbacks are very high viscosities and cost. The typical examples of RTILs are imidazolium hexafluorophosphate or pyridinium hexafluorophosphate, but other anions (like tetrafluoroborate or TFSI) can be used instead of PF_6^- [28].

Polymer electrolytes represent a widely used type of solid and semi-solid electrolytes for LIBs. As it was mentioned above, polymer electrolyte can represent either a so-called "dry solid" system which is free of flammable liquid but has lower ionic conductivity (Table 3), or a gel-like polymer filled with conventional liquid electrolyte [29], which is still much less flammable than a wetted separator. One of the most widespread bases for "dry solid" systems is polyethylene oxide (PEO). "Dry solid" systems based on PEO conduct lithium better, if PEO acquires more amorphous domains, and three main approaches for strengthening its amorphization can be distinguished: addition of polyelectrolytes, e.g. lithium polyacrylate (PAA) or polymethacrylate ("PMAA") [30]; addition of $BF_3 \cdot OEt_2$ into a mixture of PEO and lithium PAA, the molar ratio B:Li being

26

unity [31]; addition of ceramic particles, e.g. Al_2O_3, SiO_2 [32], TiO_2 [33]. Alternatives for PEO are poly(ethylene oxide) methyl ether methacrylate (PEOMA), copolymers of polyester diacrylate (PEDA) and polyethylene glycol (PEG) and many other combinations [32]. Gel electrolytes are based mostly on polyvinylidene difluoride (PVdF) but they also can be enhanced by addition of ceramic particles (e.g. $BaTiO_3$, TiO_2 [29],[33]) or copolymerization of vinylidene difluoride with hexafluoropropylene (HFP) [34]. Gels based on copolymers of PVdF and HFP ($\approx$12 wt.% of HFP) normally have ionic conductivity between 10^{-3} and 10^{-2} S/cm [32]. Alternative bases for gel electrolytes are polyacrylonitrile (PAN) [29], polymethylmethacrylate (PMMA) [32], PMMA cross-linked with 70 wt.% of natural rubber [35], and others.

Table 3. Ionic conductivities of some "dry solid" polymer electrolytes at room temperature [32].

Electrolyte salt	Ratio $Li:O_{PEO}$	lg $\sigma_{25°C}$, $[\sigma]$=S/cm	Electrolyte salt	Ratio $Li:O_{PEO}$	lg $\sigma_{25°C}$, $[\sigma]$=S/cm
$LiCF_3SO_3$	1:9	−6.2	$Li(C_2F_5SO_2)_2N$ (LiBETI)	1:8	−6.7
LiTFSI	1:10	−4.7		1:16	−5.3
	1:20	−6.3	$LiClO_4$	1:8	−6.0
	1:24	−7.4		1:20	−8.0

1.4. Anode materials for lithium-, sodium- and potassium-ion batteries

As one may conclude from the Overview chapter, anode material should have low potential of its redox transformation upon insertion of lithium (or other metal ions).

Metallic lithium was historically the first anode material for lithium secondary cells because it offers the lowest possible redox potential and huge theoretical specific capacity of 3861 mAh/g. This is so high that in practice the final specific capacity of such battery will depend mostly on the capacity of the counter-electrode material. Two crucial drawbacks of the lithium anode are high reactivity towards some solvents (not alkyl carbonates, though) and ability of lithium to host on its surface lithium crystals of dendritic shape during cycling. Since dendrites can grow out of anode surface without limitation, they puncture separator and one of them occasionally reaches the cathode side, forms a short circuit and initiates thermal runaway of the battery [2]. This issue has drastically limited usage of the lithium anode, and plenty of works were devoted to overcoming this issue [36]. A battery with metallic lithium or its alloy is called lithium battery. Term "lithium-ion battery" emerged in connection with research and development of graphite powder as the intercalation host for lithium; if graphite is used as the anode instead of lithium, then lithium ions from cathode are reversibly intercalated into the space between graphite layers.

First electrochemical experiments with graphite were not successful because of co-intercalation of solvation shells of lithium cations which caused strong expansion of interlayer space in graphite and its exfoliation [9]. Ethylene carbonate was found to form a very stable SEI film which conducts lithium ions but is impenetrable for solvent molecules which allowed to reach ideal reversibility of lithium intercalation into graphite [9]. An example of its galvanostatic charge-discharge curve is depicted in Figure 4. Formula LiC_6 of the charged graphite corresponds to theoretical specific capacity of 372 mAh/g. Strong

additional advantage of graphite is its low redox potential of 0.1÷0.3 V vs. Li/Li⁺. The only fundamental disadvantage of the lithium-ion batteries with the graphite anode is their inability to be charged faster than ≈30÷60 minutes because graphite cannot tolerate very fast expansion of interlayer space upon lithium intercalation.
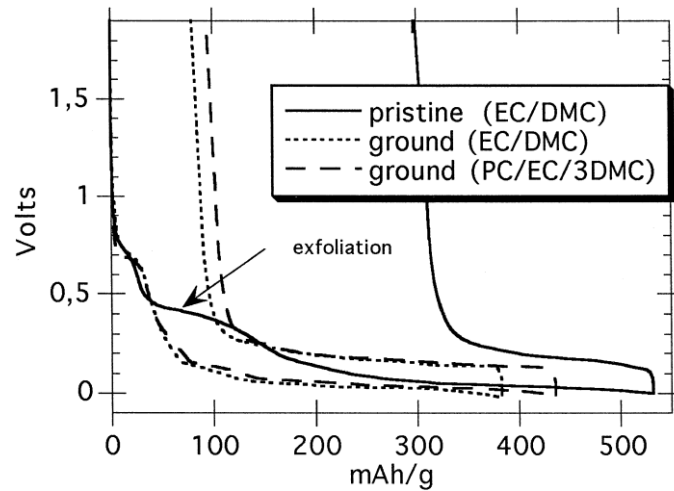
Figure 4. First galvanostatic cycle of graphite (Le Carbone Lorraine) in a lithium-ion half-cell at the current density 20 mA/g (ground samples underwent grinding with rotor blade grinder for 15 minutes) [37]. Reprinted from the Journal of Power Sources, vol. 81-82, B. Simon et al., On the choice of graphite for lithium ion batteries, p. 312-316, Copyright 1999, with permission from Elsevier.

In the search for an alternative intercalation anode for lithium-ion batteries which could sustain high rates of charge and discharge and possess better cyclability a complex oxide of lithium and titanium $Li_4Ti_5O_{12}$ with the spinel-type structure has been found (Figure 5) [38]. This compound is capable of intercalating 3 additional lithium atoms per formula unit with a formation of $Li_7Ti_5O_{12}$ [39]. In spite of its smaller theoretical specific capacity of 175 mAh/g and higher redox potential of 1.55 V vs. Li/Li⁺ the material has

been vastly commercialized because of the following advantages: small volume change upon lithiation ($<0.1\%$) which prevents discontinuities in SEI film and eliminates mechanical strain at high current density; the SEI layer formed between 1 and 1.5 V vs. Li/Li^+ has smaller resistance than the SEI formed around 0.1 V vs. Li/Li^+; finally, battery containing $Li_7Ti_5O_{12}$ instead of LiC_6 is dramatically safer in the case of a thermal runaway than its graphite counterpart [40]. Batteries based on $LiFePO_4$ cathode and $Li_4Ti_5O_{12}$ anode possess roughly twice as small specific energy as conventional lithium ion batteries, but demonstrate unmatched cyclability and power capability: they are able to withstand 20000 cycles at current density of 10C saving 95% of the initial specific energy [41].
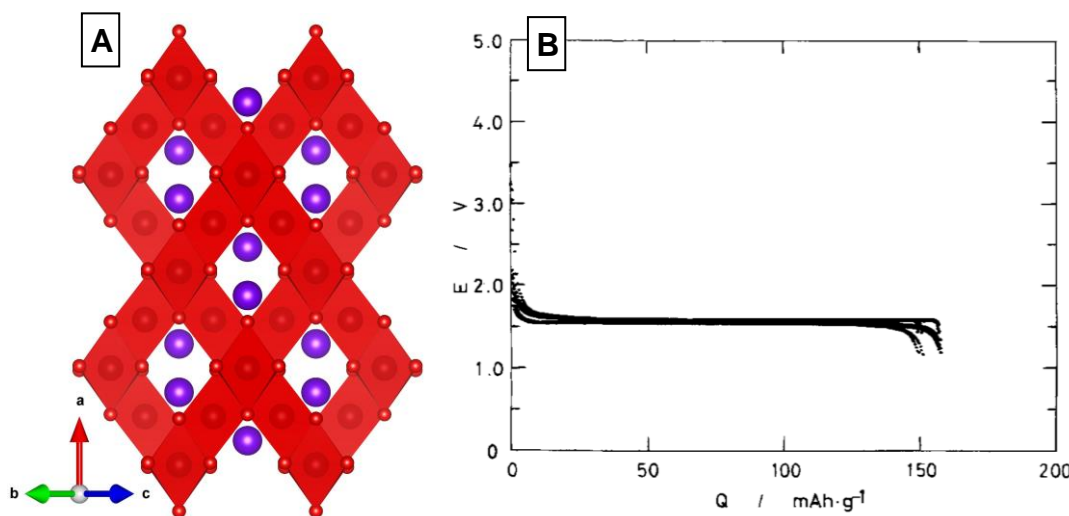
Figure 5. (**A**) Sketch of $Li_{4+x}Ti_5O_{12}$ with the spinel structure; TiO_6 octahedra are painted red and lithium atoms are marked with violet spheres. (**B**) galvanostatic charge-discharge curves of $Li_4Ti_5O_{12}$ in a lithium-ion half-cell at the current density of 5 mA/g and temperature of 30°C [38]; republished with permission of IOP Publishing from the Journal of The Electrochemical Society, vol. 142, №5, p. 1431-1435 (1995); permission conveyed through Copyright Clearance Center, Inc.

Specific group of anodes which possess intermediate properties between graphite and lithium and still are free of the dendritic problem are alloys of lithium with semimetals (silicon [42], arsenic [43], antimony [44]) and with metals with higher electronegativity (tin [45], indium [46]). The serious drawback for some of them (e.g. silicon and tin alloys) is actually too high specific capacity which means big volume changes (up to 300%) and dramatic capacity fade in several tens of cycles. But in spite of that silicon is regarded as a promising anode already for almost two decades [47] because of high natural abundance and appropriate value of its redox potential of 0.4 V vs. Li/Li$^+$ [42]. Nanostructured forms of silicon, e.g. nanotubes, suffer less from expansion because of the absence of three-dimensional long range order [48], and preparation of nanocomposites with carbon and titanium carbide can prevent loss of electric contact between nanoparticles and current collector upon cycling. Thus, practical specific capacity of silicon alloys varies between 500 and 2000 mAh/g depending on the electrode nanostructure and overall composition [48]. But low volumetric capacity and high final cost of silicon nanomaterials, be it thin films or nanotubes, still have not been overcome on the way to commercialized lithium silicon batteries.

It was until 2015 that main specific drawback of graphite for usage in sodium-ion batteries was actual instability of binary compounds of sodium and graphite [49]. But in 2015 it was published that glycol ethers are capable of supplying the sodium ions with an appropriate solvation shell for highly reversible inclusion of solvated sodium cations between graphite layers (Figure 6, **A**, **B**) [50], the solvation number of sodium being equal to 2. Density functional theory (DFT) calculations predicted that such solvated ions can be

31

intercalated and extracted easily, possessing high diffusivity in the interlayer space and even improvings electric conductivity of the graphite layers [51]. Still, multiple attempts to use graphite in sodium-ion cells (Figure 6, **A, B**) [50], [52], [53], as well as attempts to use complex oxides of sodium and titanium with "channel" structure – $Na_2Ti_3O_7$ [54], $Na_2Ti_4O_9$ [55], $Na_4Ti_5O_{12}$ [56], or even nanostructured TiO_2 [57], ended up with huge irreversible capacity on the first cathode branch necessarily followed by several or few cycles with coulombic efficiency <95% and irreversible sodium loss coupled with all of this. Besides, larger sodium ionic radius hinders fast diffusion in vast majority of these materials. That's why the materials with a higher redox potential and intrinsically outstanding sodium diffusivity, namely so-called natrium super-ionic conductors (Nasicons, space group *R*-3*c*) became attractive for researchers. Thus, $NaTi_2(PO_4)_3$ has been tested as an anode material, and with a proper synthetic procedure it was able to give out 80% of its capacity at the current density of 10C with overvoltage <0.3V and excellent cycle stability [58]. The only but crucial drawback preventing its usage in sodium-ion batteries is its high redox potential of ≈2.1 V vs. Na/Na^+. Finally, for the solution of the problem of potassium anodes generally meso- and macroporous materials based on carbon are tested, e.g. microspheres from so-called hard carbon (Figure 6, **C**) [59], and also the metal-organic framework from titanium (IV) terephthalate (referred to as Mil125(Ti) (Figure 6, **D**) deserves special mentioning [60]. But the problem of the irreversible capacity fade on the first cycles is actual here as well as in the case of sodium anodes.
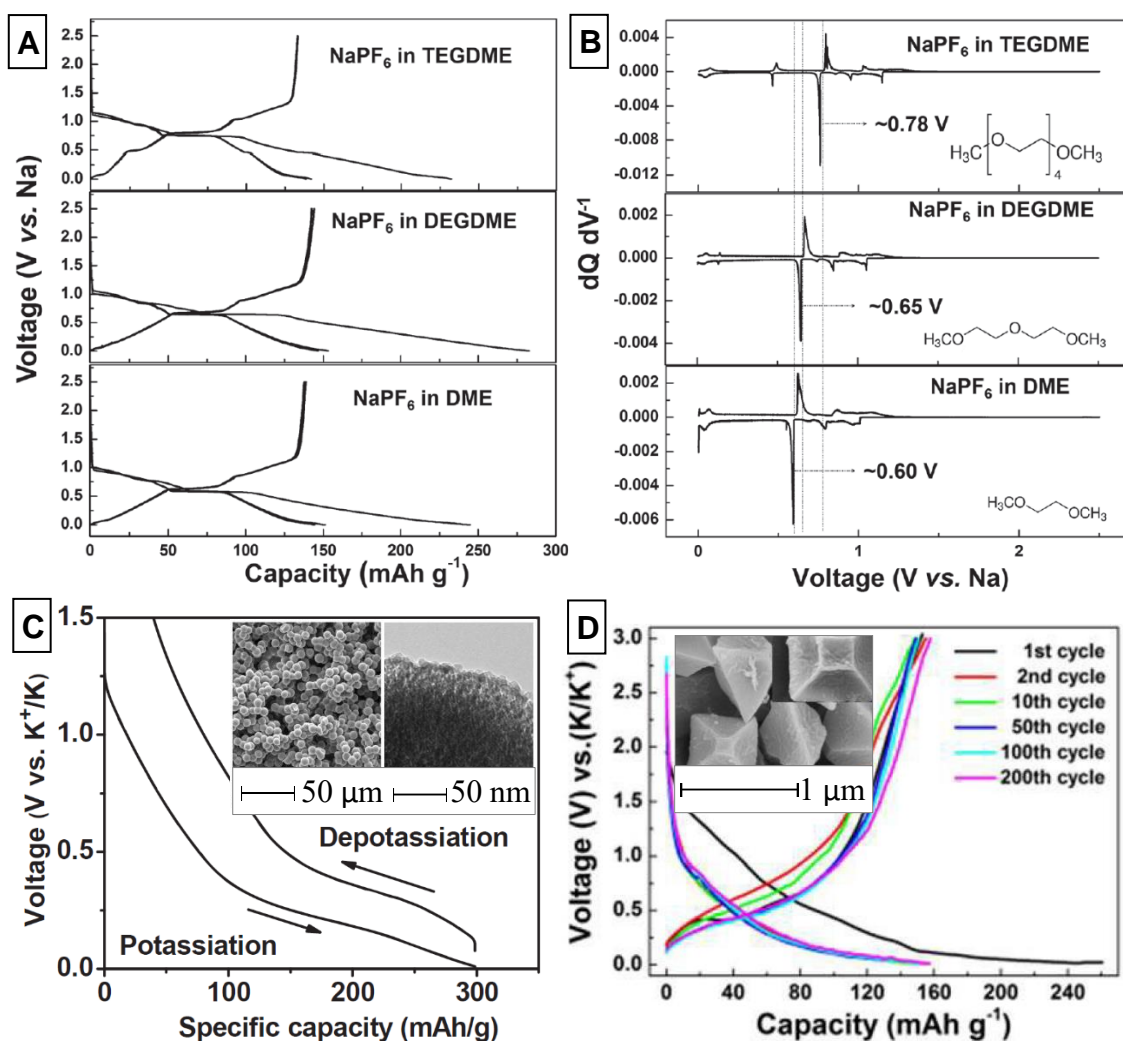
Figure 6. (**A**) Galvanostatic charge-discharge curves (current density 100 mA/g) and (**B**) the corresponding differential capacity curves of sodium-ion half-cells with graphite electrodes and 1M solutions of NaPF$_6$ in 1,2-dimethoxyethane (DME), diglyme (DEGDME) and tetraglyme (TEGDME) as electrolytes [50]; (**C**) the second galvanostatic cycle of hard carbon microspheres (current density 30 mA/g) [59] and (**D**) galvanostatic charge-discharge curves of the Mil125(Ti) (current density 50 mA/g) [60] in potassium-ion half-cells; micrographs are represented in insets. Figures (**A**) and (**B**) reproduced from the Advanced Functional Materials 25, №4, p. 534-541 (2015) with permission of John Wiley and Sons; figure (**C**) adapted from the Advanced Energy Materials 6, №3, p. 1501874 (2015) with permission of John Wiley and Sons. Figure (**D**) republished with permission of the Royal Society of Chemistry from "A titanium-based Metal-Organic Framework as an Ultralong Cycle-Life Anode for PIBs" by Yongling An et al. from Chem. Comm., vol. 53, 2017; permission conveyed through Copyright Clearance Center, Inc.

1.5. Cathode materials for lithium-ion batteries

The following requirements towards potential metal-ion cathode materials are conventionally applied [1]: presence of a redox active element capable of possessing different oxidation states (e.g. metals of 3d block: Co^{4+}/Co^{3+}, Fe^{3+}/Fe^{2+}, Mn^{3+}/Mn^{2+}, V^{5+}/V^{4+} etc.); high ionic conductivity; electronic conductivity, the higher the better; high specific capacity; an appropriately high redox potential of the compound; smaller structural and volumetric changes upon charge and discharge; abundance and environmental safety. Theoretical specific capacity of a redox active compound is calculated from the following formula:

$$C = \frac{nF}{M} = \frac{26.805n}{M},$$

where F is Faraday constant (96485 C/mol = 26.805 A·h/mol), n is the number of electrons or ions participating in the redox reaction, M is the molecular mass.

The most widespread graphite lithium-ion anode has much higher specific capacity than the vast majority of cathode materials known up to now, and this fact strengthens dependence of the final battery specific energy on the specific energy of the cathode material. In turn, for decades such importance of research and development in the field of lithium-ion cathodes promoted publications in their domain much stronger than in the domains of the other metal-ion cathodes. That's why in the present literature review special attention is paid to well-studied lithium compounds; it was easier for them to make a demonstration of how the structure type, chemical composition and synthetic technique together determine the final performance of the cathode. Thus, below are described the

cathodes which are implemented in the commercialized lithium-ion batteries. Then follow several types of inorganic lithium-ion cathodes which have been investigated in detail but not commercialized. Organic cathodes for metal-ion batteries represent a very promising but completely different type of materials because organic materials propose challenges strongly different from ones of inorganic materials; that's why organic cathodes lay out of the scope of the present review.

Layered chalcogenides

In 1970 it had been found that lithium diffusion in layered chalcogenides enables reversible electrochemical lithium intercalation [61]. Titanium disulfide became the first commercialized intercalation cathode because of high specific capacity, electronic and ionic conductivity and formation of a continuous solid solution series Li_xTiS_2 ($0 \leq x \leq 1$) (Figure 7); when x=0, the TiS_2 layers are kept together by Van der Waals weak force. Quality of TiS_2 strongly depends on the accuracy of synthesis technique: even slight excess of titanium between the TiS_2 layers attracts them to each other and shortens interlayer distance which spoils Li-ion transport properties. Excess sulfur, contrary to titanium, leads to "antibonding" of the layers and finally may cause formation of monoclinic TiS_3 [62]. These difficulties are the reasons of high cost of the TiS_2 cathode. Cathode material based on TiS_2 undergoes 1000 reversible charge/discharge cycles in apparently single-phase mode with 0.05% capacity loss per cycle. In 1988 Exxon has produced a lithium battery with LiAl alloy anode and TiS_2 cathode for watches and other portable devices. Its specific energy was roughly twice as small as the energy of the modern lithium-ion batteries [1].
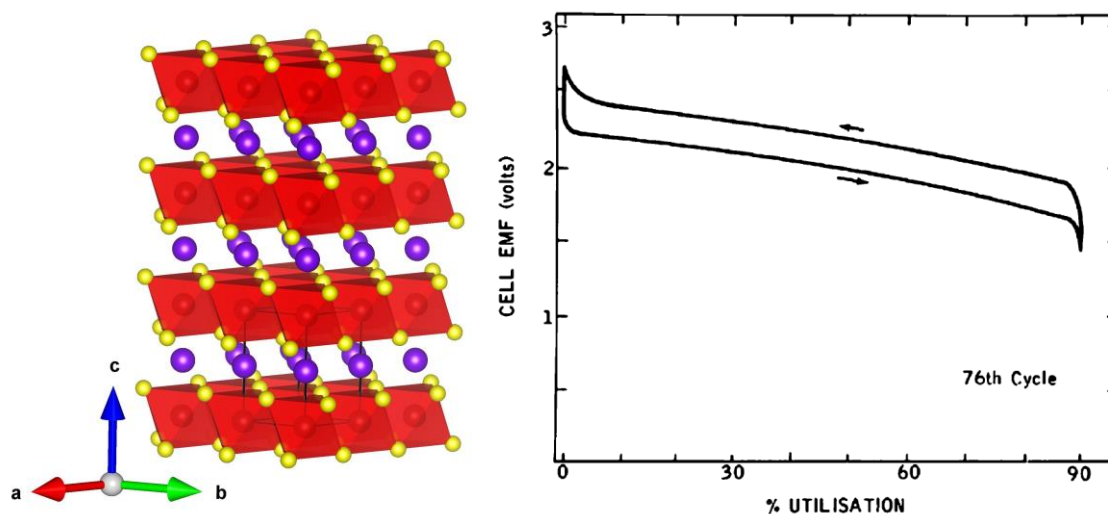
Figure 7. **Left** – crystal structure of $LiTiS_2$; red octahedra with yellow corners stand for TiS_6 units and violet spheres mark lithium atoms. **Right** – 76-th cycle of a Li/TiS_2 electrochemical cell at the current density 10 mA/cm^2 [1]; reprinted from the Progress in Solid State Chemistry, vol. 12, №1, M. Stanley Whittingham, Chemistry of intercalation compounds: Metal guests in chalcogenide hosts, p. 41–99, Copyright 1978, with permission from Elsevier.

Transition from sulfides to oxides possessing higher ionicity in comparison with sulfides leads to dramatic increase of the cell voltage, and consequently specific energy of the battery. $LiCoO_2$ has been proposed by John Goodenough as a promising candidate for the cathode material of advanced lithium batteries [63]. A lithium battery with $LiCoO_2$ as the cathode and graphite as the anode was successfully commercialized in 1991, and this moment is widely considered as the birth of the modern lithium-ion battery industry. In 2019 Goodenough's discovery along with those made by Stanley Whittingham and Akira Yoshino have been marked with a Nobel prize in Chemistry. Crystal structure of majority of oxide cathodes represents a "cubic" close packing of oxygen atoms where voids are

occupied by lithium and transition metal cations. LiCoO$_2$ has space group $R\bar{3}m$ and is isostructural to α-NaFeO$_2$: lithium atoms are positioned in octahedral voids formed between layers of edge-sharing CoO$_6$ octahedra (Figure 8, **left**); that's why sometimes this structure type is referred to as an ordered rock salt. Typical galvanostatic cycle of Li$_x$CoO$_2$ in the 0.5≤x≤1 range is depicted in the Figure 8 (**right**) [63], [64]. Deintercalation of lithium ions from Li$_x$CoO$_2$ in the 0.5≤x≤0.8 range occurs through single-phase mechanism [65].
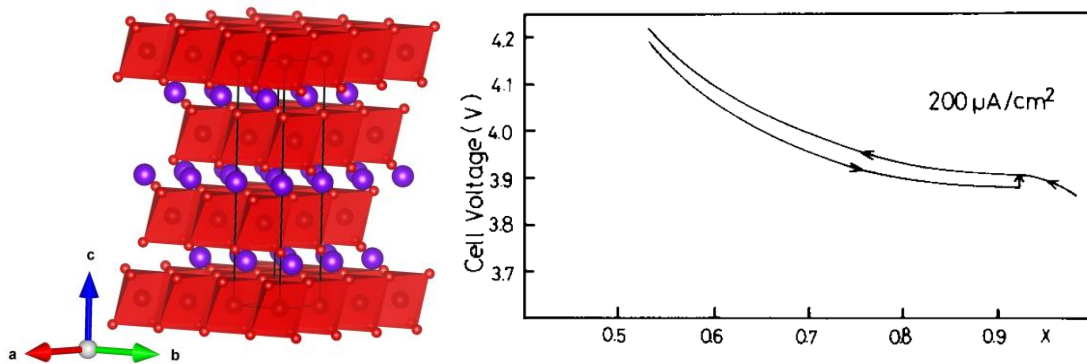
Figure 8. **Left** – crystal structure of LiMO$_2$ (M is 3d metal); red octahedra stand for MO$_6$ units and violet spheres mark lithium atoms. **Right** – typical galvanostatic cycle of Li$_x$CoO$_2$ [63], [64]; reprinted from the Materials Research Bulletin, vol. 15, №6, K. Mizushima et al., Li$_x$CoO$_2$ (0<x≤1): A new cathode material for batteries of high energy density, p. 783–789, Copyright 1980, with permission from Elsevier.

When x in Li$_{1-x}$CoO$_2$ noticeably exceeds 0.5, irreversible structure degradation occurs. Degradation of Li$_{0.5-\delta}$CoO$_2$ is caused by spontaneous reduction of metastable Co^{4+} to Co^{3+} and evolution of excess oxygen. It can take place either slowly through many cycles or in the "thermal runaway" mode, depending on the upper cutoff voltage on charge, and

that's why the cutoff voltage for $LiCoO_2$ is conventionally limited to 4.2÷4.3 V vs. Li/Li^+, limiting its specific capacity to 140 mAh/g (while its theoretical capacity is 274 mAh/g). However, the reversible capacity can be raised by replacement of some fraction of cobalt (III) with an equimolar mixture of manganese (IV) and nickel (II). Manganese (IV) stabilizes structure while $Ni^{2+} \rightarrow Ni^{3+} \rightarrow Ni^{4+}$ redox transitions compensate for capacity loss with the deleted cobalt; aluminum can be added for the same reason as Mn (Table 4). However, if too high percentage of Mn or Ni is introduced, then a local disorder of Li with 3d metals can lead to local structural transitions to spinel-like fragments [66]–[68].

Table 4. Properties of some formulations based on layered $LiMO_2$.

Composition	$LiCoO_2$	$LiCo_{0.8}Al_{0.2}O_2$	$LiMn_{0.4}Co_{0.2}Ni_{0.4}O_2$
Redox voltage vs. Li/Li^+, V	4.2–4.3	4.5	4.6
Specific capacity at the current density C/12, mAh/g	140	120–140	200 (C/12) 150 (5C)
Lithium disordering, %	–	–	1–6%
Reference	[63]	[66]	[67]

LiMn2O4 with spinel structure

In order to get somewhat cheaper and more environmentally friendly cathode, an oxide formulation without toxic cobalt was commercialized, this one has formula $LiMn_2O_4$ with a spinel structure (Figure 9, **left**). From the X-ray photoelectron spectroscopy data the manganese atoms possessing the formal oxidation state +3.5 actually have either +3 or +4 oxidation state [69]; the redox potential of Mn^{3+}/Mn^{4+} in $LiMn_2O_4$ is ≈4.1 V vs. Li/Li^+, the charge/discharge curve consists of two plateaus of the same capacity (Figure 9, **right**). While the composition of spinel by itself prevents irreversible structural changes upon overcharge, gradual amorphization is possible at slightly raised temperatures of operation

[70]. Another drawback of spinel is that its specific capacity is smaller by 30-50% than that of layered oxides, which noticeably decreases the specific energy of the battery. Both drawbacks are addressed by a derivative compound $LiNi_{0.5}Mn_{1.5}O_4$ which has the redox potential of ≈ 4.7 V vs. Li/Li^+ almost without voltage slope [47]. This value is slightly higher than conventional electrolytes can tolerate, but a huge work in the field of "high voltage" electrolytes has already been made (some options are mentioned in the Electrolytes chapter).
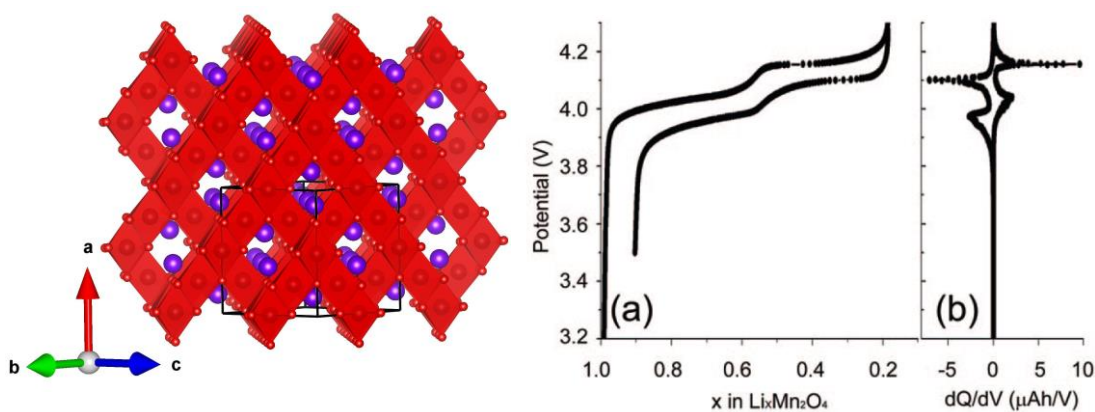
Figure 9. **Left** – structure of $LiMn_2O_4$; red octahedra stand for the MO_6 units and violet spheres mark lithium atoms. [64]. **Right** – galvanostatic cycle of $LiMn_2O_4$ nanorods and the corresponding differential capacity curve [69]; reprinted with permission from "Spinel LiMn2O4 Nanorods as Lithium Ion Battery Cathodes" // D. K. Kim et al., Nano Lett., vol. 8, №11, p. 3948–3952 (2008). Copyright 2008 American Chemical Society.

LiMPO4

Phosphates $LiMPO_4$ (M = Mn, Fe, Co, Ni) represent another type of cathodes suggested by Nobel laureate J. Goodenough and coworkers [71]. Materials based on $LiMPO_4$ are cheap and environmentally friendly (as long as the composition does not contain Co^{2+}). Interest to these compounds can be explained by their safety for flammable

electrolytes (at least in the case of $LiFePO_4$ [72]) and by negative inductive effect of phosphate groups leading to increase of the $M^{k+}/M^{(k-1)+}$ redox potential. They offer relatively high theoretical specific capacity of 170 mAh/g and an almost flat galvanostatic curve without voltage slope [71]. Among them $LiFePO_4$ possesses the lowest redox potential ($\approx$3.4 V vs. Li/Li^+), which defines its moderate specific energy (550 W·h/kg), and the Mn and Co analogues have the potentials of $\approx$4.1 and $\approx$4.8 V, respectively [73]–[74]. This finding became the impetus for investigation of huge number of compounds containing different polyanions, e.g. BO_3^{3-}, SiO_4^{4-}, CO_3^{2-}, PO_4^{3-}, $P_2O_7^{4-}$, SO_4^{2-}, also combined with fluoride anion.

The structure of $LiMPO_4$ (Figure 10) has space group *Pnma* and is closely related to that of olivine $(Mg, Fe^{+2})_2SiO_4$. It consists of lithium ions occupying channels between chains of the MO_6 octahedra, which in turn are linked by the PO_4 tetrahedra. $LiFePO_4$ has a mineral name triphylite but it is often referred to as phospho-olivine, or just olivine. While $LiFePO_4$ has visible "diffusion tunnels" along the *b* and *c* crystallographic directions, *ab initio* calculations show that Li^+ diffusion can occur only along the *b* direction [75]. Upon lithium extraction the unit cell parameters *a* and *b* slightly decrease while *c* increases, and the phase transition from triphylite to isostructural heterosite $FePO_4$ occurs [76], the latter compound being stable even at very high temperature in contrast to the charged oxide cathodes. Single-phase regions in the Li_xFePO_4 system are shown to be at x< 0.032 and x>0.962 [77].
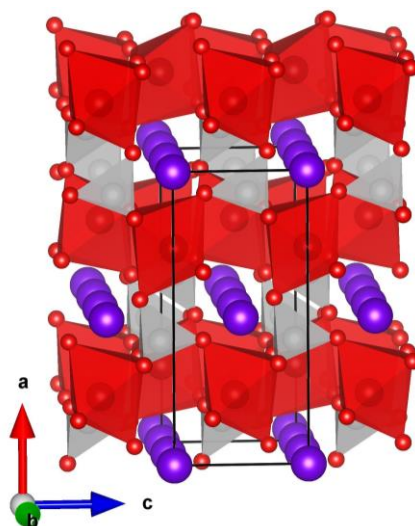
Figure 10. Crystal structure of LiMPO$_4$ (M=Fe, Mn, Co); grey tetrahedra depict PO$_4$ groups, red octahedra stand for MO$_6$ and violet spheres mark Li atoms.

Besides the fact that LiFePO$_4$ has moderate specific energy, it has another two drawbacks common for LiMPO$_4$: bulk LiFePO$_4$ has a low electric conductivity ($\lg(\sigma) \approx -9$, $[\sigma]$=S/cm) [78] and a moderate apparent Li diffusion coefficient ($\lg(D) \approx -15$, $[D]$=cm^2/s) [79], the lithium intercalation/extraction rate being controlled by the phase boundary between LiFePO$_4$ and FePO$_4$ [79]. Both these drawbacks can be mitigated, though. Usage of the "soft chemistry" methods allows to obtain LiMPO$_4$ with particles of submicron size [80]. When the particles thus obtained are thoroughly mixed with glucose or another organic compound and then calcined, a conductive composite of LiMPO$_4$ with carbon is obtained instead of a pure non-conductive powder [81]. Carbon coating not only serves as the conductive additive but also hinders aggregation and sintering of the particles during calcination. For example, nanoplates of LiMnPO$_4$ with thickness <30 nm along crystallographic direction *b* have been obtained using hydrothermal method. After carbon coating of particles they could demonstrate capacity 80 mAh/g at the current density 5C

[82]. More recently it was reported that carbon-coated $LiMnPO_4$ obtained through polyol-assisted hydrothermal method with pre-synthesized hollow-sphere Li_3PO_4 particles used as the precursor allowed to reach more than 140 mAh/g of discharge capacity at the current density C/20 [83]. Finally, an accelerated synthesis of $LiMnPO_4$ with microwave irradiation and *in situ* carbon coating was reported [84]; the material obtained in a fraction of an hour demonstrated reversible specific capacity 155 mAh/g at 0.5C after 100 cycles and 118 mAh/g at 10C. $LiMnPO_4$ historically is one of the first compounds which showed reversibility of the Mn^{3+}/Mn^{2+} redox transition. However, it seems that the manganese-containing compounds require considerably higher overvoltage ([85], [86]), than the purely ferrous ones with a similar morphology of particles ([87], [88]). Comparison of behavior of the Fe^{3+}/Fe^{2+} and Mn^{3+}/Mn^{2+} transitions when iron and manganese are mixed in one material ($LiMn_{0.6}Fe_{0.4}PO_4$ [89]) leads to a conjecture that the mechanism of the redox transitions of specific atoms can be the reason of that overvoltage (but other proofs are necessary for the exact conclusion).

Li_2MSiO_4

The success of cathode materials based on $LiMPO_4$ heats up interest for further investigations of the polyanion compounds, and silicates Li_2MSiO_4 (M = Mn, Fe, Co) represent a compound with polyanion based on a semimetallic element. They are interesting because of theoretical possibility to reversibly extract more than one lithium per formula unit getting much higher specific capacity than 165 mAh/g. The only condition for this is reversibility of multielectron activity of the selected 3d metal.

Li_2MSiO_4 has several polymorphs [90] which can be considered as deformed hexagonal close packings of oxygen atoms where cations occupy deformed tetrahedral voids. These polymorphs differ by mutual orientation and connectivity of the MO_4 and SiO_4 tetrahedra and by presence/absence of a slight monoclinic distortion. The layered β_{II}-Li_2MSiO_4 (M=Fe, Mn; sp. gr. *Pmn*2_1 [91]) is isostructural to β-modification of Li_3PO_4. Framework of γ_0-Li_2MnSiO_4 (sp. gr. *P*2_1/*n* [92]) is isostructural to γ-modification of Li_3PO_4. The layered γ_s-Li_2FeSiO_4 (sp. gr. *P*2_1 [93] or *P*2_1/*n* [94]) is a derivative of β_{II}-Li_2FeSiO_4 with a unit cell of doubled volume and the periodical modulation of orientation of FeO_4 and SiO_4 tetrahedra in the chessboard order [93]. The three referred polymorphs of Li_2MSiO_4 attract more attention as active cathodic compounds, and the former two are represented in Figure 11. All of them can be recognized by tetrahedra MO_4 and SiO_4 directed collinearly to *c* axis by one of their corners. The orthorhombic γ_{II}-modification of Li_2MnSiO_4 (sp. gr. *Pmnb* [95]), in short, unites properties of the first two polymorphs and requires high temperature (>>700°C) to be obtained in the pure form. And the fifth polymorph (sp. gr. *Pn* [96]) should be also mentioned: it was obtained by means of ion exchange of sodium for lithium in carbon-coated Na_2MnSiO_4 and is found to be stable at temperatures <370°C.
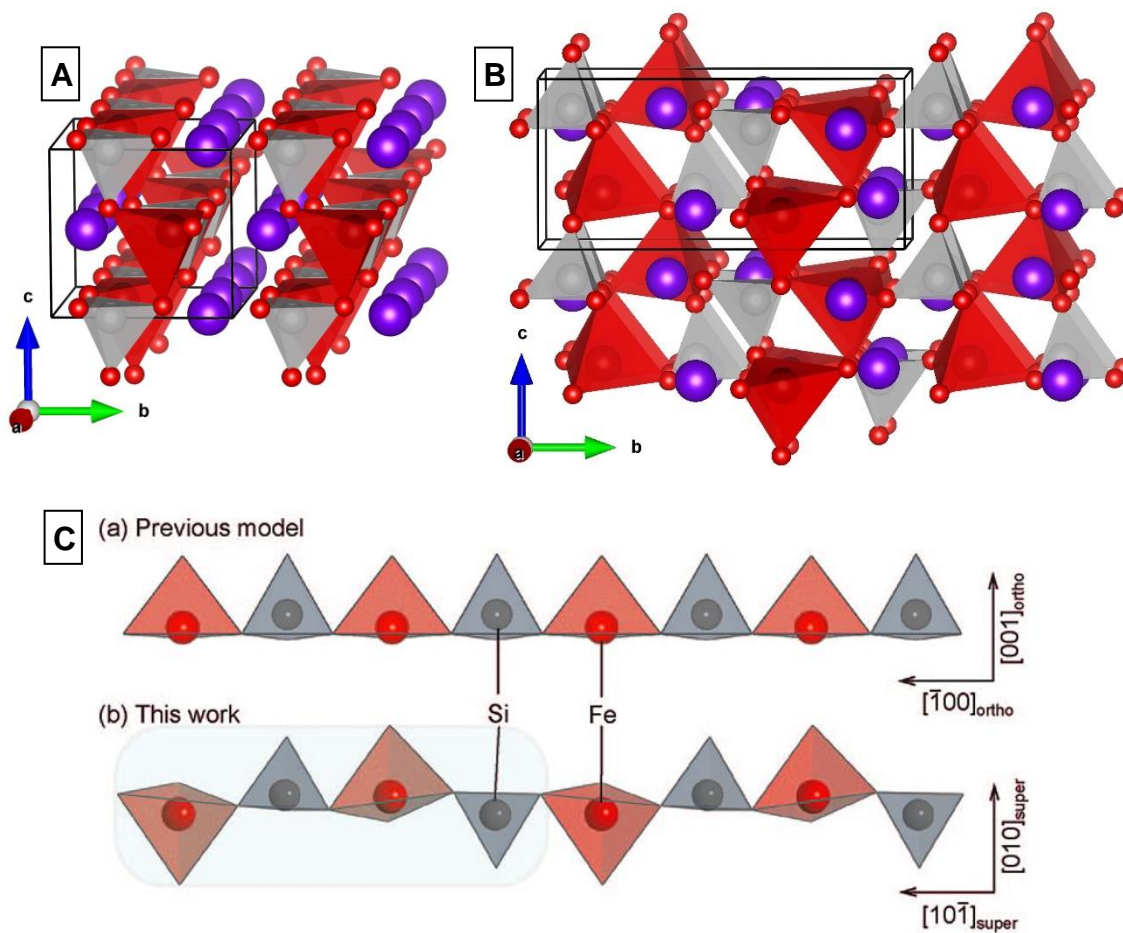
Figure 11. (**A**) β_{II}-Li$_2$MSiO$_4$ (M=Fe, Mn; sp.gr. *Pmn*2$_1$ [91]) and (**B**) γ_0-Li$_2$MnSiO$_4$ (sp.gr. *P*2$_1$/*n* [92]). Smaller grey tetrahedra mark SiO$_4$ anions, bigger red tetrahedra are for MO$_4$ units and violet spheres mark lithium atoms. (**C**) a sketch which might illustrate the key difference between β_{II}- modification (the upper tetrahedra row) and γ_s-modification (the lower tetrahedra row) of Li$_2$FeSiO$_4$ [93]; adapted with permission from "Structure of Li2FeSiO4" // S. Nishimura et al., J. Am. Chem. Soc. Commun., vol. 130, №40, p. 13212–13213 (2008). Copyright 2008 American Chemical Society.

Unfortunately, there was no success in preparation of cathode materials based on silicates Li_2MSiO_4 with strongly outstanding practical characteristics. Some samples with good electrochemical activity have been demonstrated, though. Carbon-uncoated particles of β_{II}-Li_2FeSiO_4 (sp.gr. *Pmn2$_1$*) with elongated form and dimensions of 0.4x1.5 microns have been obtained at low temperature (by hydrothermal technique), and they showed specific capacity of 70 mAh/g with average voltage of 2.7 V vs. Li/Li^+ at 2C current density [97]. It is to be noted that β_{II}-Li_2FeSiO_4 can be obtained electrochemically from γ_s-modification upon cycling [94]; as was shown later using slower cycling at the current density C/50 and heating to 55°C, it is possible due to electrochemical oxidation of oxygen [98]. Another example is carbon-coated β_{II}-Li_2MnSiO_4 with extremely small particle size of 25 nm which has demonstrated capacity of 44 mAh/g after 100 cycles at a low current (C/5) [99]; this compound demonstrated qualitatively worse behavior than the β_{II}-Li_2FeSiO_4, and this case resembles the one of $LiMPO_4$ (M=Fe, Mn). Remarkedly better performance was obtained in the above-mentioned metastable *Pn* polymorph of Li_2MnSiO_4: the sample consisting of even smaller particles (10 nm) has shown 110 mAh/g with the average voltage 2.8 V vs. Li/Li^+ (C/8) [96]; but capacity fade exceeded 30% per 50 cycles, and still there is no meaningful advantage from the multielectron activity of manganese.

LiMBO$_3$

Orthoborates $LiMBO_3$ represent another type of polyanion framework, which is built up by a non-metal of low electronegativity. Orthoborate is one of the lightest polyanion which makes $LiMBO_3$ a cathode with very high theoretical specific capacity of

≈220 mAh/g. Electrochemical experiments for $LiMBO_3$ (M = Mn, Fe, Co) have been set up for the first time in 2001 [100], but then negligible 4% of lithium were extracted at the very low current density C/250. Later solid solution mechanism of cycling with very small volume change (≈2%) has been established for $LiFeBO_3$ (Figure 12) [101]. These two features are premises for cyclability and relatively fast Li^+ diffusion in $LiFeBO_3$.
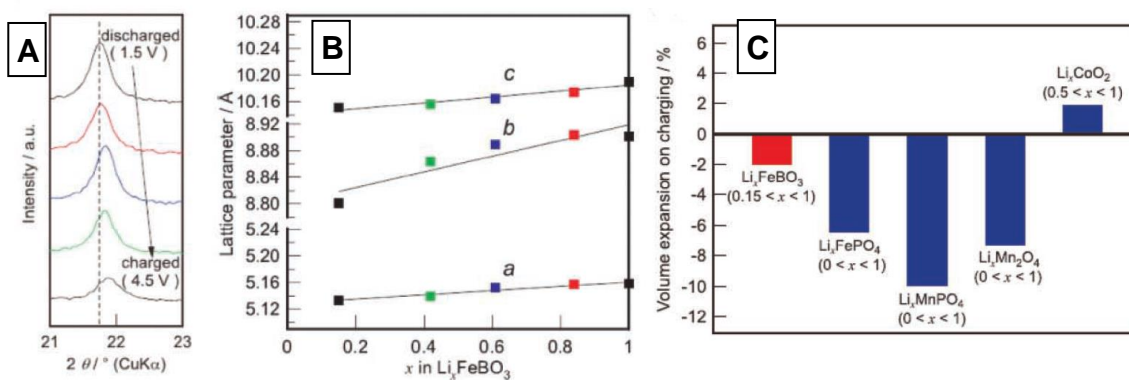
Figure 12. (**A**) Shifts of reflections upon lithium extraction; (**B**) parameters change depending on the change of lithium content; (**C**) volume change of unit cell of $LiFeBO_3$ and of some other unit cells ($x<0.85$ in $Li_{1-x}FeBO_3$) [101]. Reproduced from Advanced Materials 22, №32 p. 3583-3587 (2010) with permission of John Wiley and Sons.

$LiMBO_3$ (M = Fe, Co) are known to have only one polymorph with space group $C2/c$, but for $LiMnBO_3$ an additional hexagonal modification called h-$LiMnBO_3$ is known and it is described by the space group $P6$-; its monoclinic counterpart then is called m-$LiMnBO_3$. The three-dimensional MBO_3 framework of monoclinic $LiMBO_3$ consists of trigonal bipyramids MO_5 and triangular anions BO_3 (Figure 13, **A**). In this framework bipyramids MO_5 are connected by their edges and form isolated $(MO_3)_\infty$ chains running

along [-1 0 1] direction. Lithium occupies two tetrahedral positions forming diffusion channel along *c* direction, the two tetrahedra being connected by edges with each other. Every triangle BO_3 links three chains of the MO_5 bipyramids and three lithium channels. Three-dimensional $MnBO_3$ framework of *h*-LiMnBO$_3$ is composed of MnO_5 square pyramids and BO_3 triangles (Figure 13, **B**). Every MnO_5 pyramid is linked with another two MnO_5 pyramids with edges forming a $(MnO_3)_\infty$ chain along the *c* axis. As in the monoclinic LiMBO$_3$, triangles BO_3 are perpendicular to the *c* direction and connect three $(MnO_3)_\infty$ chains, but three inequivalent boron positions are present instead of one in *m*-LiMBO$_3$. Lithium atoms occupy tetrahedral positions connected by edges and forming channels along *c* and $(MnO_3)_\infty$ chains.
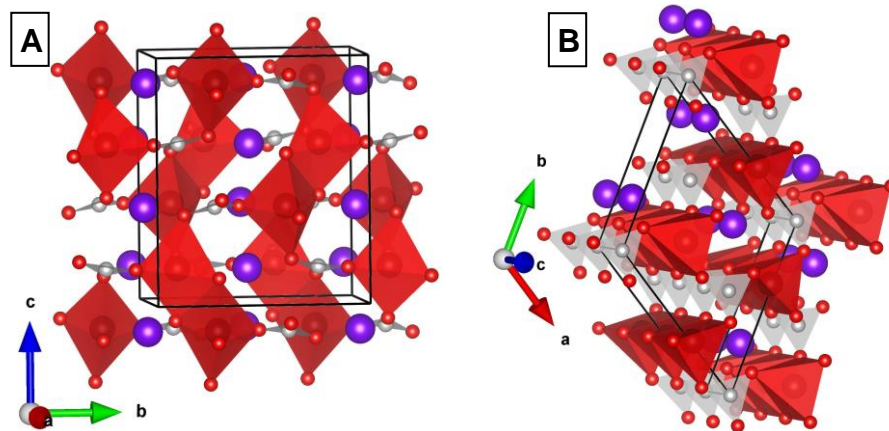
Figure 13. Crystal structure of (**A**) *m*-LiMBO$_3$ (space group *C2/c*; M = Mn, Fe, Co) [64] and (**B**) *h*-LiMnBO$_3$ [100]; red polyhedra mark the MO_5 units, flat grey triangles are for the BO_3 groups and violet spheres mark the lithium atoms.

The main drawback of LiMnBO$_3$ and LiCoBO$_3$ is low stability of their charged states which is most probably caused by atypical coordination of the transition metal (just

like in the above-mentioned Li_2MnSiO_4). The second problem is a "borderline" value of the activation energy for diffusion hop in lithium-conductive channels (Table 5) [102].

Table 5. Activation energies $E^{\neq}$ for lithium diffusion in m-$LiMBO_3$ in comparison with some other compounds [102].

Formula	$E^{\neq}$, eV	Reference	Formula	$E^{\neq}$, eV	Reference
$LiFeBO_3$	0.44		$LiFePO_4$	0.30	[103]
$LiMnBO_3$	0.49	[102]	$LiCoO_2$	0.25	[104]
$LiCoBO_3$	0.48		$LiNi_{0.5}Mn_{1.5}O_4$	0.35	[105]

LiFeBO₃

The common feature of all experiments involving $LiFeBO_3$ (see Table 6 below) is that $LiFeBO_3$ has relatively low capacity fade (a few percent per hundred of cycles) but there is a necessity of getting smaller particles and the best possible carbon coating, like for $LiMPO_4$ and Li_2MSiO_4. The main laboratory method of synthesis of carbon-coated $LiFeBO_3$ is a ceramic method, $FeC_2O_4 \cdot 2H_2O$ being the iron-containing precursor. Alkaline nature of the complex lithium borate coupled with easiness of iron oxidation in air means very high reactivity of $LiFeBO_3$ towards air moisture which means that correct techniques of avoiding contact of $LiFeBO_3$ with air should be meticulously followed (Figure 14, **up**) [101]. The harmful influence of exposition to air was confirmed by a comparison of [57]Fe Mössbauer spectra of a pristine $LiFeBO_3$ sample and the same sample after storage in air for 24 hours – in the former the doublet of Fe^{2+} was the only component of the spectrum while the latter contained huge doublet of Fe^{3+}. Total prevention of contact of $LiFeBO_3$ with air allowed to dramatically increase reversible capacity [101] in comparison with an air-oxidized sample ([106]) and to reach 86% of the theoretical specific capacity along with

comparable or better cyclability [101]. It is underlined that even very short exposition to air may cause capacity decrease by 30% and introduce plenty of side reactions into the process of cycling [101]. Unavoidable impurity Fe_3BO_5 apparently is not so harmful for the cathode characteristics. The above-mentioned non-degraded sample of $LiFeBO_3/C$ obtained in Ref. [101] demonstrated reversible specific discharge capacity of ~190 mAh/g at the C/20 current density, and acceptable cyclability (Figure 14, **down**). The insurmountable obstacle for practical usage of $LiFeBO_3$ is its relatively low redox potential.

Table 6. Some techniques used for synthesis of $LiFeBO_3$ and the final characteristics of the obtained samples.

| Suggested reagents and short description of synthesis conditions	% of reversible lithium extraction and capacity fade	Ref.
"Fe(II) oxalate" + $LiBO_2$: 250°C, 3 h, N_2; 750°C, 15 h, N_2	≤4% Li was extracted	[100]
Li_2CO_3 + H_3BO_3 + $FeC_2O_4 \cdot 2H_2O$: Planetary ball mill; 350°C, 10 h, N_2; 650°C, 10 h, 95%Ar + 5%H_2	57% Li, C/40, capacity fade 0.03% per cycle (no carbon); 72% Li, C/40, capacity fade 0.025% per cycle (5 wt% of C)	[106]
$LiBO_2$ + $FeC_2O_4 \cdot 2H_2O$: Planetary ball mill; Mixing with 4% solution of cellulose acetate, drying in air; 700°C, 24 h, CO/CO_2	70% Li, C/12, capacity fade 0.07% per cycle.	[107]
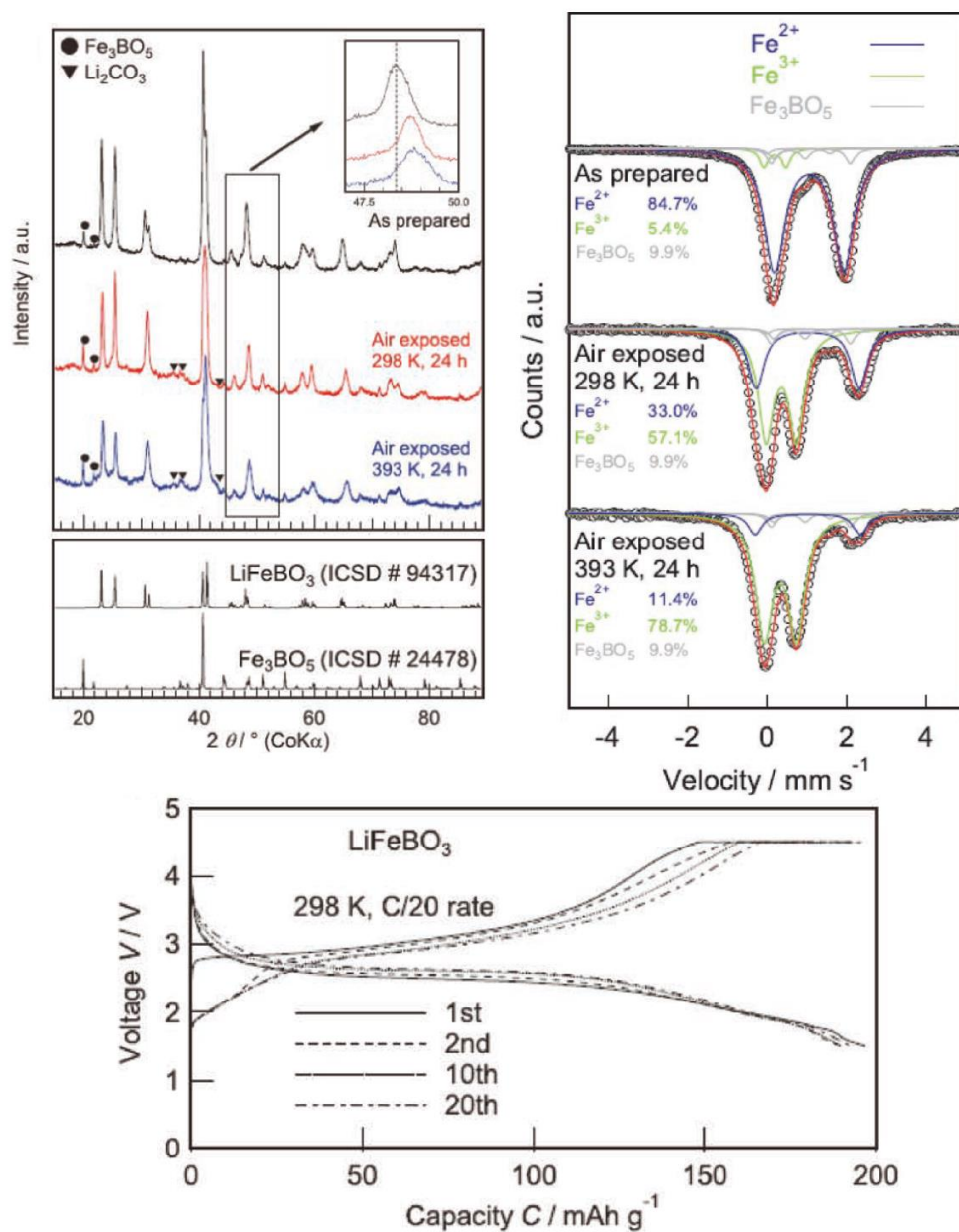
Figure 14. (**Up**) Powder X-ray diffraction patterns (**left**) and Mössbauer spectra (**right**) for pristine and air-exposed samples of $LiFeBO_3/C$ and (**Down**) its $1^{st}-20^{th}$ galvanostatic curves at the velocity C/20 [101]. Reproduced from the Advanced Materials 22, №32 p. 3583-3587 (2010) with permission of John Wiley and Sons.

LiMnBO₃

LiMnBO$_3$ possesses a higher redox potential than LiFeBO$_3$: *h*-LiMnBO$_3$ has E$_{theor}$=4.11 V vs. Li/Li$^+$ (calculated), *m*-LiMnBO$_3$ has E$_{theor}$=3.7 V (calculated) and E$_{experim}$≈3.4 V (experimental) [108]. DFT calculations predicted for *h*-LiMnBO$_3$ inappropriately high activation energy of diffusion hop E$^{\neq}$=0.723 eV, while for *m*-LiMnBO$_3$ E$^{\neq}$=0.509 eV [108] or 0.491 eV [102] (depends on the conditions of calculation).

Ceramic synthesis of electrochemically active *m*-LiMnBO$_3$ was successfully realized in a whole series of works (Table 7), but in every of them the cyclability is qualitatively worse than that for LiFeBO$_3$ (Table 6). For example, a comparable cyclabilities are shown in two different works ([108], [109]), and in the former capacity fade is ≈3% per one cycle at the current C/20 (Figure 15) [108]. In the same work *h*-LiMnBO$_3$ has also been obtained, but since a very high temperature of calcination was used [108], strong sintering took place and the obtained morphology became inappropriate. But application of a sol-gel technique instead of the ceramic synthesis allowed to get nanorods of *h*-LiMnBO$_3$ with the thickness of ~20 nm and length of ~200 nm, which showed 75% of the theoretical capacity with the average voltage of 2.7 V vs. Li/Li$^+$ (C/20) and capacity fade of ≈3% per cycle (like in *m*-LiMnBO$_3$) [110].
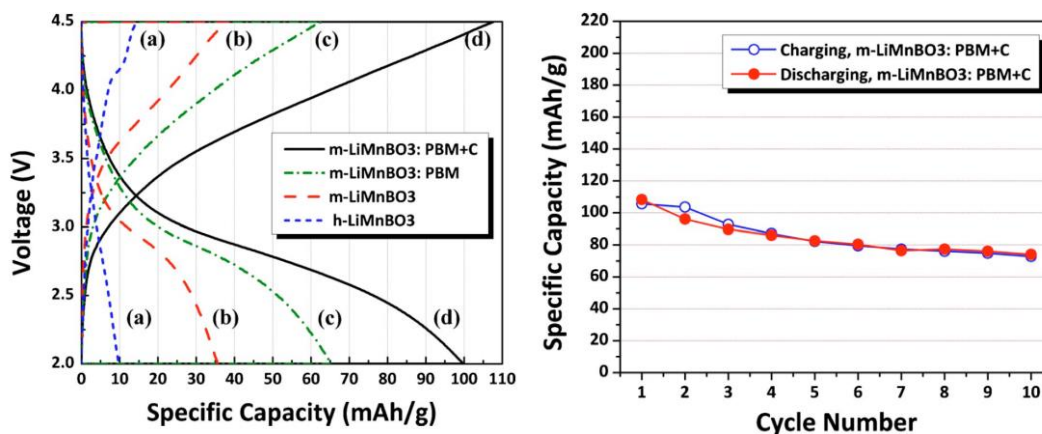
Figure 15. **Left** – galvanostatic charge-discharge curves for different samples at the current density C/20; PBM tag marks planetary ball milling after calcination and +C tag marks addition of 10 wt.% of sucrose and additional shorter calcination for making uniform carbon coating [108]; **right** – cyclability of the sample *m*-LiMnBO$_3$:PBM+C, C/20 [108]. Republished with permission of IOP Publishing from the Journal of The Electrochemical Society, vol. 158, №3, p. A309-A315 (2011); permission conveyed through Copyright Clearance Center, Inc.

Table 7. Some techniques used for synthesis of $LiMnBO_3$ and the final characteristics of

the samples obtained by them.

Suggested reagents and short description of synthesis conditions	Polymorph, % of reversible lithium extraction and capacity fade	Ref.
$MnO + LiBO_3$: 750°C, 18 h	h-$LiMnBO_3$; <3% Li.	[100]
$Li_3CO_3 + MnC_2O_4 \cdot 0.5H_2O + B_2O_3$ + Ketchen Black (8 wt%), + vapor grown carbon fiber (2 wt%); 600°C, Ar	m-$LiMnBO_3$/C 41% Li, C/20, capacity fade 2% per cycle	[101]
$Li_2CO_3 + MnC_2O_4 \cdot 2H_2O + H_3BO_3$ Ball milling; 350°C, 10 h, Ar; Ball milling; 500°C (m-polymorph) or 800°C (h-polymorph), 10 h, Ar; Optional: ball milling with 10 wt% sucrose; 500°C, 5 h, Ar; Optional: ball milling with electrode carbon black	m-$LiMnBO_3$/C 45% Li, C/20, capacity fade 3.4% per cycle	[108]
$LiOH \cdot H_2O + H_3BO_3 + MnCO_3$; adipic acid ($C_6H_{10}O_4$) as the source of carbon-coating: 250°C, 3 h, air; 750°C, 15 h, Ar	m-$LiMnBO_3$/C 50% Li, C/20, capacity fade 0.7% per cycle	[109]
$LiNO_3$, $Mn(NO_3)_2 \cdot (H_2O)_4$, $B(OEt)_3$ in propionic acid. Addition of small volume of water, evaporation at 80-100°C to gel-like state; 350°C, 10 h, carbon monoxide; ball milling with 33 wt% of graphene oxide (GO); 200-250°C, 8h, N_2; Final carbon content ≈20 wt% (Combustion infrared spectroscopy analysis)	nano-h-$LiMnBO_3$/C (reduced GO) 66% Li, C/20, initial capacity fade 5% per cycle, after 50% loss of capacity its fading slows down; 36% Li, C/2.	[110]
$Li_2CO_3 + H_3BO_3 + MnO_2$ Ball milling; 850°C, 12 h, 70%Ar+30%H_2	h-$LiMnBO_3$ (strongly sintered powder, size of particles reaches few microns) 33% Li, C/44, capacity fade 0.09% per cycle	[111]
$Li_2CO_3 + H_3BO_3 + MnCO_3$ Ball milling; + Ketjchen black; 70°C, 12 h, air; Dispersion in deionized water; spray pyrolysis	m-$LiMnBO_3$/C 75% Li, C/20, strong capacity fade in the initial cycles (≈10% per cycle).	[112]

LiMn$_x$Fe$_{1-x}$BO$_3$

There was a successful attempt to combine relatively good cyclability of LiFeBO$_3$ and higher redox potential of LiMnBO$_3$ in a solid-solution series LiMn$_x$Fe$_{1-x}$BO$_3$ [113], applying the synthetic procedure taking into account reactivity towards air. From powder X-ray diffraction patterns of Li$_{1-y}$Mn$_x$Fe$_{1-x}$BO$_3$ acquired *ex situ* for several values of y (0≤

y≤1) one can make a conclusion that mechanism of cycling in LiMn$_x$Fe$_{1-x}$BO$_3$ is single-

phase for all x (0, 0.25, 0.5, 0.75, 1) [113]. The relative volume change upon deintercalation (≈3%) [113] was consistent with the one reported for the fully ferrous analogue (≈2%)

[101]. As was expected, LiMn$_x$Fe$_{1-x}$BO$_3$ demonstrated much better cyclability than LiMnBO$_3$ (Figure 16).

LiCoBO$_3$

LiCoBO$_3$ is the most attractive potential cathode material from the whole LiMBO$_3$ series because it has an ideal value of redox potential of ≈4V vs. Li/Li$^+$ [114]. It is very

difficult to synthesize LiCoBO$_3$ in a phase-pure form because of easiness of cobalt (II) oxidation or reduction upon heating in furnace, and by the same reason it is impossible to obtain a composite with carbon using conventional methods of carbon coating. Still the main synthetic method is the ceramic method, but it has an intermediate stage of formation of Co$_2$B$_2$O$_5$ [100], [114]. A detailed electrochemical investigation of LiCoBO$_3$ showed that during lithium extraction from the near-surface layer of LiCoBO$_3$ this layer becomes amorphous and loses lithium-ion conductivity, while cobalt partially dissolves in

54

electrolyte (proved by atomic absorption spectroscopy) [114]; attempts to chemically oxidize $LiCoBO_3$ by NO_2BF_4 led to its total destruction.
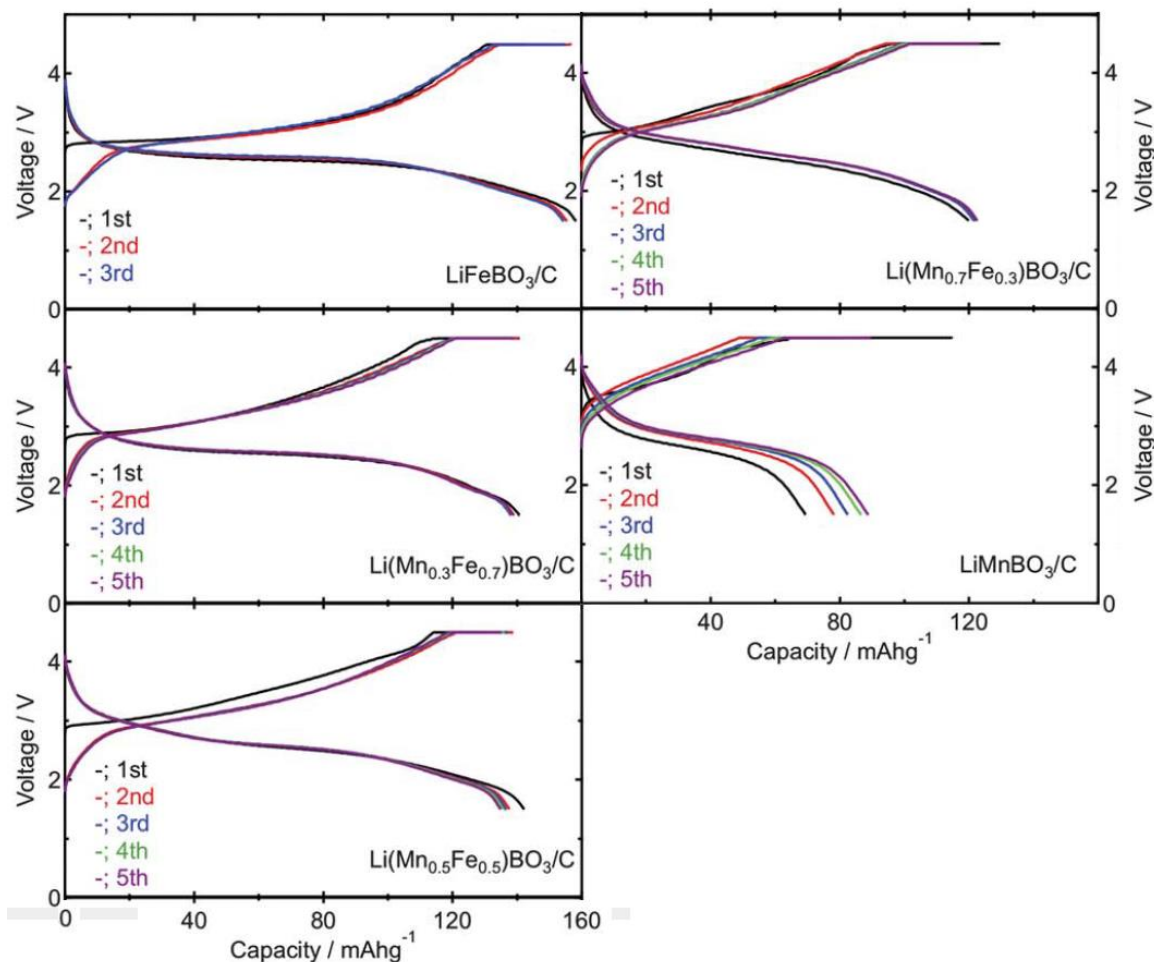
Figure 16. Galvanostatic charge-discharge curves of $LiMn_xFe_{1-x}BO_3$ (C/20) [113]. Republished with permission of the Royal Society of Chemistry from "Synthesis and electrochemistry of monoclinic Li(MnxFe1−x)BO3: a combined experimental and computational study" by A. Yamada et al. from J. Mater. Chem., vol. 21 (29), 2011; permission conveyed through Copyright Clearance Center, Inc.

1.6. Cathode materials for sodium- and potassium-ion batteries

Investigated inorganic cathodes for sodium- and potassium-ion batteries mostly are represented by crystalline compounds of sodium or potassium and of the redox active metals of 3d block (V, Cr, Mn, Fe, Co, Ni, Cu), these compounds being divided into two main subgroups: complex transition metal oxides (may also contain fluorine), polyanion materials and compounds derivative from Prussian blue (Table 8). In the field of sodium-ion batteries it has resulted in particular interest towards making different compositions of the general formula $Na_{2-x}M(PO_4)_{1.5}$ which are referred to as Nasicons. A separate kind of research activity is electrochemical replacement of one alkaline metal with another one, e.g. sodium intercalation into charged Li_0FePO_4 ([115], [116]).

Table 8. Selected inorganic compounds as potential sodium- and potassium-ion cathodes.

Formula	Space group and structure analogue (if any)	Current density (mA/g, ±1%), and specific discharge capacity (mAh/g, ±1 mAh/g; number of cycle is 50 if not stated otherwise)	E_c in the half-discharged state (V, ±0.1 V, 1st cycle)	Ref.
NaFePO$_4$	$Pnma$, LiFePO$_4$	15, 111	3	[115]
		15, 105		[116]
Na$_3$V$_2$(PO$_4$)$_3$	$R\bar{3}c$, Na$_{1+x}$Zr$_2$Si$_x$P$_{3-x}$O$_{12}$	≥60, ≥80	3.3	[117]–[124]
Na$_3$TiMn(PO$_4$)$_3$		13, 80	3.5	[125]
Na$_3$V$_2$(PO$_4$)$_2$F$_3$	$P4_2/mnm$	64, 123 (1st cycle)	3.4	[126]
Na$_{0.44}$MnO$_2$	$Pbam$, Na$_4$Mn$_9$O$_{18}$	120, 60	2.9	[127]
Na$_{1.73}$Fe[Fe(CN)$_6$]$_{0.98}$	$Fm\bar{3}m$	100, 105	3	[128]
Na$_2$FePO$_4$F	$Pbcn$, Na$_2$CoPO$_4$F	50, 105	3	[129]
Na$_2$CoPO$_4$F		6.2, 100 (1st cycle)	4.3	[130]
P2-type K$_{0.6}$CoO$_2$	$P6_3/mmm$	100, 60 (nth cycle)	2.8	[131]
KVPO$_4$O	$Pna2_1$, KTiOPO$_4$	6.5, 67	4.1	[132]
KVPO$_4$F		6.5, 70	4.2	
KFeSO$_4$F		6.5, 100 (1st cycle)	3.5	[133]
K$_{0.220}$Fe[Fe(CN)$_6$]$_{0.805}$·4.01H$_2$O	$P2_1/n$	100, 70	3.2	[134]
K-rich Prussian blue		60, 79	3.4	[135]
K$_{1.6}$Mn[Fe(CN)$_6$]$_{0.96}$·0.27H$_2$O		50, 85 (30th cycle)	3.8	[136]

Complex transition metal oxides

Investigated complex oxides of sodium/potassium and transition metals are represented mainly by A$_x$MO$_2$, where A=Na or K, M is for transition metal and 0.3≤x≤1 depending on the initial composition and the state of charge. Na$_{0.44}$MnO$_2$ has an orthorhombic unit cell with *Pbam* space group (V=678 Å^3) [137] and is isostructural to

$Na_4Mn_4Ti_5O_{18}$ [138]. The manganese atoms are distributed between two different oxygen coordination environments: all Mn (IV) and half of the Mn (III) are in octahedral sites and the remaining Mn (III) sit in square-pyramids, the latter forming edge-sharing chains linked into two double and one triple octahedral chains by the vertices, leading to the formation of two types of tunnels (Figure 17, **A**). Two sodium sites (referenced as Na1 and Na2 in Figure 17, **A**) are contained in large S-shaped tunnels, while the third site (Na3) is found in smaller tunnels [137]; sodium diffusion occurs in the direction perpendicular to the Figure 17, **A**. When $Na_{0.44}MnO_2$ is discharged to $Na_{0.65}MnO_2$, sodium is intercalated into S-shaped tunnels as they are only half-filled in $Na_{0.44}MnO_2$. $Na_{0.44}MnO_2$ was obtained by a series of different synthetic techniques: solid-state reaction between Na_2O_2 and MnO_2 [127], urea-based solution combustion [139], hydrothermal treatment of Na-birnessite [140] or Mn_3O_4 [141]. The reversibility of redox activity for Na_xMnO_2 formed electrochemically from $Na_{0.44}MnO_2$ was established for $0.25<x<0.65$ [137]. There six separate phases and five two-phase transitions can be distinguished upon analysis of cyclic voltammograms, differential capacity curves obtained from galvanostatic curves and *operando* powder X-ray diffraction at an extremely low current density of C/250 [137]. The typical galvanostatic discharge curves of a material with apparently the best performance reported up to the moment are shown in Figure 17 (**B**).
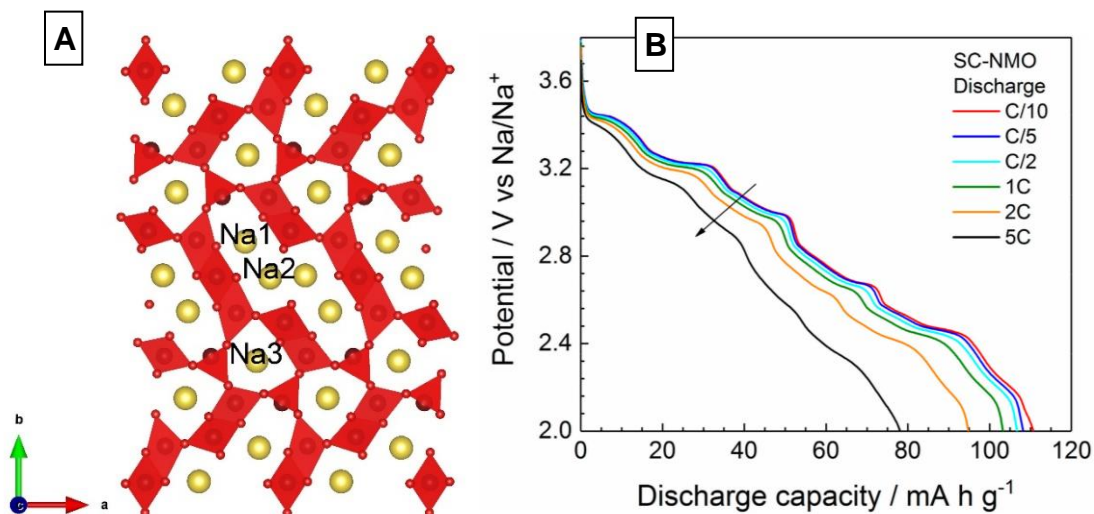
Figure 17. (**A**) Schematic projection of the crystal structure of $Na_{0.44}MnO_2$ onto the *ab* plane; red polyhedra mark the MnO_5 and MnO_6 units and yellow spheres mark sodium atoms; the depicted pattern repeats along *c* forming spacious sodium channels. (**B**) the galvanostatic discharge curves of SC-NMO at different C rates [139]; reprinted under the CC-BY 4.0 license from Batteries, vol. 4, №1, p. 8 (2018).

There has been established a system of notation for A_xMO_2, in which a special symbol is placed right before the chemical formula of the oxide; it represents the shape of the coordination environment of alkaline metal (P is for AO_6 prism and O is for AO_6 octahedron) and the number of unique oxygen atomic planes parallel to the alkaline atomic layers [142], for example P2-$K_{0.6}CoO_2$ (or "P2-type $K_{0.6}CoO_2$") [131] or O3-$NaMn_{0.25}Fe_{0.25}Co_{0.25}Ni_{0.25}O_2$ [143]. Also, as well as in the case of complex lithium transition metal oxides, changing of the composition of transition metals (V, Cr, Mn, Fe, Co, Ni) and doping with electrochemically inactive metals (Mg [144], Ca [145], Al [146], Zn [147]) alter practical characteristics: cyclic stability, redox potential and, importantly, air stability. A peculiar kind of modification is copper doping which has a notable positive

influence on the material stability towards decomposition with wet air; it was demonstrated in a series of works [148].

Sodium-ion cathode materials generally demonstrate lower specific capacity than the lithium-ion counterparts, which is related to with generally strong Na−Na repulsion and necessity of a bigger voltage cutoff for cycling even in a narrow compositional range [142]; this tendency seems to be even stronger for the potassium-ion cathodes [131],[149]. More serious problem of potassium-ion oxide cathodes is the low melting point of potassium oxide 740°C [19] (for sodium oxide it is 1134°C [19]). This makes chemical synthesis of potassium layered oxide cathodes with complex compositions difficult (this is not an obstacle for the electrochemical synthesis of them, though) and that's why only oxides with a relatively simple composition, like P2-$K_{0.44}Ni_{0.22}Mn_{0.78}O_2$ [149] or P2-$K_{0.6}CoO_2$ [131], have been chemically synthesized up to now. In P2-$K_{0.6}CoO_2$ with $P6_3/mmm$ space group potassium occupies large prismatic voids making neighboring CoO_2 layers mirroring each other (Figure 18, **A**). At least seven distinct compounds can be supposed from its galvanostatic curves (Figure 18, **B**) which indicate that the effective K content can be reversibly varied between 0.33 and 0.68 throughout 2V-large voltage window. Total volume change during deintercalation of 0.35 K atoms per formula unit is about +3.5% [131] because of the interlayer repulsion characteristic for all similar layered oxides. Strong interatomic repulsion between potassium atoms is considered to be the main reason of low redox potential in the potassium-rich subrange. In turn, this interatomic repulsion is attributed to big cation radius of potassium and overly weak screening of potassium atoms from each other by the valence electrons of oxygen atoms [131].
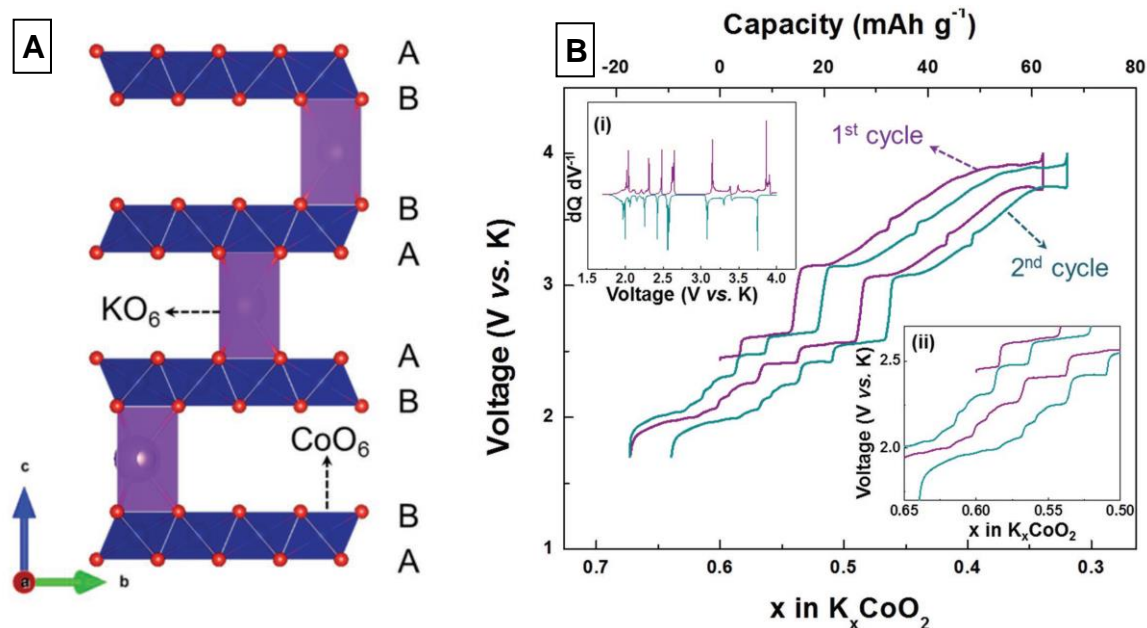
Figure 18. (**A**) Schematic crystal structure of P2-type $K_{0.6}CoO_2$; (**B**) typical charge/discharge profiles of P2-type $K_{0.6}CoO_2$ at a current rate of 2 mA/g in the voltage window between 4.0 and 1.7 V vs. K/K^+. (Inset (i): derivative curve of the second cycle and inset (ii): enlarged charge/discharge curves with K content between 0.5 and 0.65.). Reproduced from the Advanced Energy Materials 7, №17, p. 1700098 (2017) with permission conveyed through Copyright Clearance Center, Inc. Copyright 2017 Lawrence Berkeley National Lab.

An important peculiarity of electrochemical half-cells containing these compounds is high reductive activity of sodium and potassium metals, which may exert a perceptible negative influence on the apparent cyclability of the oxide cathode because of "chemical dialogue" [7] between alkali metal anode and the charged oxide cathode. By the way, lithium-ion oxide cathodes in the charged state are generally less kinetically stable towards reactions with organic electrolyte components than the polyanion compounds of lithium

and transition metals in the charged state, e.g. LiFePO$_4$ [72]. This may be true for the potassium analogues.

Polyanion compounds

The number of polyanion compounds for sodium- and potassium-ion cathodes is overly large for giving the necessary minimal attention to every structure type. In spite of that a clear initial tendency was to prefer ferrous compounds as the objects of research because of their multiple successes in the field of lithium-ion polyanion cathodes. Among them the highest reversible specific capacity (>100 mAh/g) can be attributed to hydrothermally prepared Na$_2$FePO$_4$F [150] (other techniques also have been reported, e.g. a mechanochemical synthesis [151]), olivine-type NaFePO$_4$/C prepared from LiFePO$_4$/C by aqueous ion exchange [116], Na$_2$FeP$_2$O$_7$/C [152] and Na$_4$Fe$_3$(PO$_4$)$_2$P$_2$O$_7$/C [153] prepared by solid-state synthesis. An important advantage for all of them (with an exception for NaFePO$_4$/C) is that their synthesis can be accompanied with *in situ* carbonization of the organic carbon additive. The disadvantage is that their energy density is strongly limited by their redox potential of ≈3 V vs. Na/Na$^+$.

In order to increase the energy density of ferrous metal-ion cathodes Recham et al. [133] have obtained samples of KFeSO$_4$F with KTiOPO$_4$ structure (space group *Pna2$_1$*) and tested this material as a universal metal-ion host; results of the tests with sodium and potassium are represented in Figure 19, **A**. In spite of a somewhat big volume change upon potassium extraction (≈10%, see the Figure 19, **B**) the shapes of charge and discharge curves in the Figure 19, **A** have common features which points on the reversibility of cycling. AFeSO$_4$F (A=Li, Na, K) with KTP structure was the highest energy density

sodium- and potassium-ion cathode based on Fe^{2+}/Fe^{3+} couple until the moment when another sulphate $Na_2Fe_2(SO_4)_3$ with the alluaudite structure has been reported [154]. In spite of relatively low thermal stability and extreme hygroscopicity and synthetic challenges, the cathode materials based on complex sulphates of iron (II) and manganese (II) keep attracting much of researchers' attention up to now [155]–[158].

In spite of all advantages of the ferrous cathode materials at least four promising structure types emerged due to specific advantages of vanadium-based redox couples V^{3+} → V^{4+} and/or V^{4+} → V^{5+}: $Na_3V_2(PO_4)_3$ with well-known Nasicon structure ([117]–[124]), tetragonal layered fluoride-phosphates $Na_3V_2(PO_4)_2F_3$ [159] and $Na_3V_2(PO_4)_2O_2F$ [160], KVP_2O_7 [161] and β-$NaVP_2O_7$ [162] isostructural to $KAlP_2O_7$ and $K_2[(VO)_2(HPO_4)_2(C_2O_4)]$ with a layered structure [163]. These structures (except for the latter one) still find their development in partial or total replacement of vanadium with other transition metals, for example Ti [125], Mn ([125], [164]) and Fe [165] in $Na_3V_2(PO_4)_3$; Ti, Cr, Fe and Mo in KVP_2O_7 [161]; chromium in $Na_3V_2(PO_4)_2F_3$ [166]. KMP_2O_7 with $KAlP_2O_7$ structure are known for having a "borderline" potassium-ion conductivity allowing potassium insertion/extraction only at temperatures ≥50°C [161]. Thus, the four structure types together with complex phosphates of vanadium and lithium ($Li_3V_2(PO_4)_3$ [167] and $LiVPO_4F$ [168]) explain well the emergence of interest to $KVPO_4F$ ([169], [132]) and $KVOPO_4$ [132] (Figure 20, **A**) isostructural to $KFeSO_4F$.
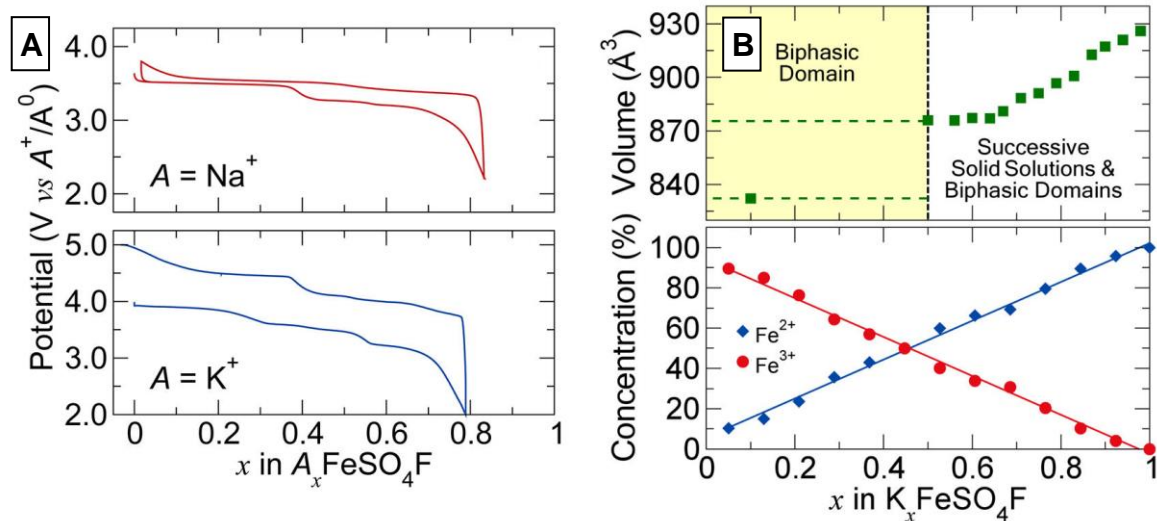
Figure 19. (**A**) Electrochemical behavior of "K_0FeSO_4F", which was obtained via the electrochemical oxidation of $KFeSO_4F$ [133]; the recovered $FeSO_4F$ powder already containing 20% carbon additive was cycled vs. Na and K anodes using 1M $AClO_4$ (A= Na or K) in propylene carbonate electrolytes at the current rate of C/20. (**B**) Evolution of the unit cell volume, along with Fe^{2+} and Fe^{3+} concentrations obtained from *in situ* Mössbauer during the first oxidation of a $Li/KFeSO_4F$ cell [133]. Reprinted with permission from "Preparation and Characterization of a Stable FeSO4F-Based Framework for Alkali Ion Insertion Electrodes" // N. Recham et al., Chem. Mater., vol. 24, №22, p. 4363–4370 (2012). Copyright 2012 American Chemical Society.
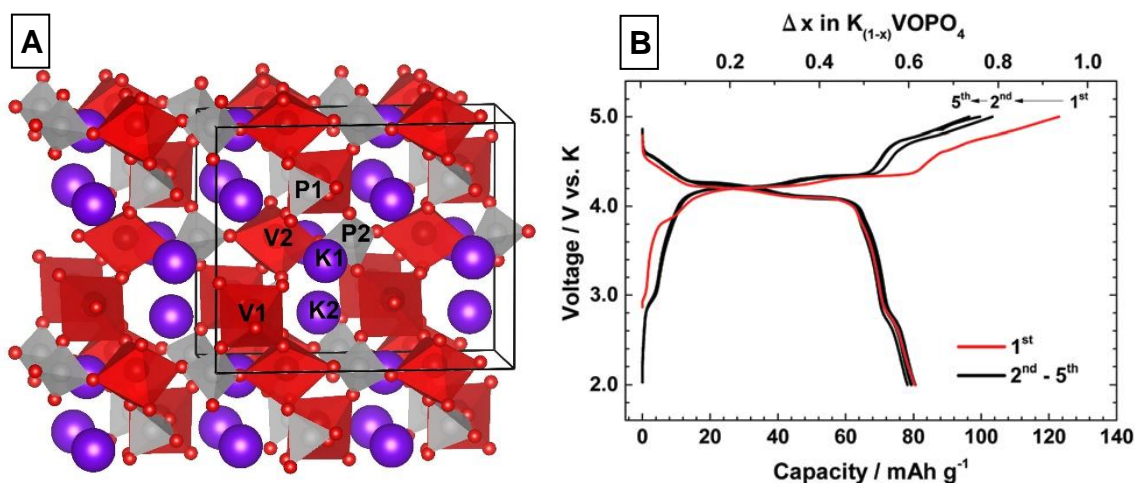
Figure 20. (**A**) Crystal structure of KVOPO$_4$ isostructural to KTP; red octahedra mark VO$_6$ units, grey tetrahedra depict PO$_4$ groups and violet spheres mark potassium atoms. (**B**) Charge and discharge profiles of KVOPO$_4$ at 5.0–2.0 V with 1 M KPF$_6$/EC:PC (1 : 1 v/v) electrolyte [132]; republished with permission of the Royal Society of Chemistry from "KVPO$_4$F and KVOPO$_4$ toward 4 volt-class potassium-ion batteries" by K. Chihara et al. from Chem. Commun., vol. 53 (37), 2017; permission conveyed through Copyright Clearance Center, Inc.

Though the theoretical specific capacity of KVOPO$_4$ is 50% higher than that of K$_{0.6}$CoO$_2$, it represents one of the best examples for showing how strongly the redox potential of oxyanion potassium cathodes differs from the same of the layered oxides of Na and K (Figure 20, **B**). The reason for that is the optimized positioning of potassium preventing the strong mutual repulsion of potassium atoms. Inductive effect of phosphorus is pronounced in KVOPO$_4$ as well as it is pronounced in the lithium-ion oxyanion cathodes; phosphorus imparts V^{4+}/V^{5+} transition a favorable redox potential 4÷4.5V vs. K/K$^+$ which theoretically allows the energy density to exceed 500 W·h/kg. The galvanostatic curves point to a highly reversible redox transformation (Figure 20, **B**); volume change for

KVPO$_4$ is reported to be −3.3% after charging to 5.0 V vs. K/K$^+$ [132], the same for KVPO$_4$F being −5.8% [132]. Thus, combination of vanadium, oxide and phosphate ions represents one of the most promising options for building a potassium-ion cathode with high energy density.

Prussian Blue derivatives

Apart stands a peculiar class of cathode materials for sodium- and potassium-ion batteries with general formula A$_x$M$^{(1)}$[M$^{(2)}$(CN)$_6$]$_{1-y}$·zH$_2$O·(OH)$_m$ where A=Na or K while M$^{(1)}$ and M$^{(2)}$ are 3d metals initially coordinated by nitrogen and carbon atoms respectively. Compounds containing 50:50 mol. mixtures of M^{2+} and M^{3+} are referred to as Prussian blues and the ones containing only M^{2+} being referred to as Prussian whites [170]; also they are called hexacyanoferrate (HCF) analogues (especially if there is M ≠ Fe). Their structure is based on a perovskite-like framework M[M(CN)$_6$]$_{1-y}$ where every 3d metal atom sits in an octahedron of CN$^-$ ligands, and CN$^-$ ligands can be partially replaced with water molecules [170] or hydroxyl anions [171]; each voluminous void between octahedra readily accommodates an alkaline metal atom but can be occupied by water as well [170]. HCF analogues with Fe^{2+} in M$^{(1)}$ position have been shown to isomerize upon aging or slight heating due to the reversible transition of an electron from Fe^{2+} to [Mn(CN)$_6$]$^{3-}$ or [Cr(CN)$_6$]$^{3-}$ [172].

Though for the Na$_x$TM[Fe(CN)$_6$]·zH$_2$O (TM=Mn, Fe, Co, Ni) compounds highly reversible cycling performance has been obtained [173], the highest interest is still attracted by HCF analogues based on manganese [136], [174]–[176] and iron [128], [134], [177]–

[179]. The main reason for that may be higher abundance and lower toxicity of these elements. HCF analogues have the theoretical specific capacity around 150 mAh/g and redox potential 3÷4 V vs. A/A^+ (A=Na, K) depending on the residual water content (Figure 21, **A**, **B**), which in turn strongly depends on the drying technique [180]. Isomerization caused by the heating drying might affect the performance as well. Another practical peculiarity of hexacyanoferrate analogues is that they are not able to survive high- or even medium-temperature treatment in a furnace in strong contrast to any other material described in the present literature review. Nevertheless, since the structure of these materials is based on strongly ionic bonds, the intrinsic electronic conductivity is not very high, and this requires looking for a proper way of mixing material with carbon, which up to now was rarely addressed. As an example, the addition of ≈10 mass.% of reduced graphene oxide has been reported to increase the discharge capacity at the current density 2C by 25% up to 115 mAh/g [176].
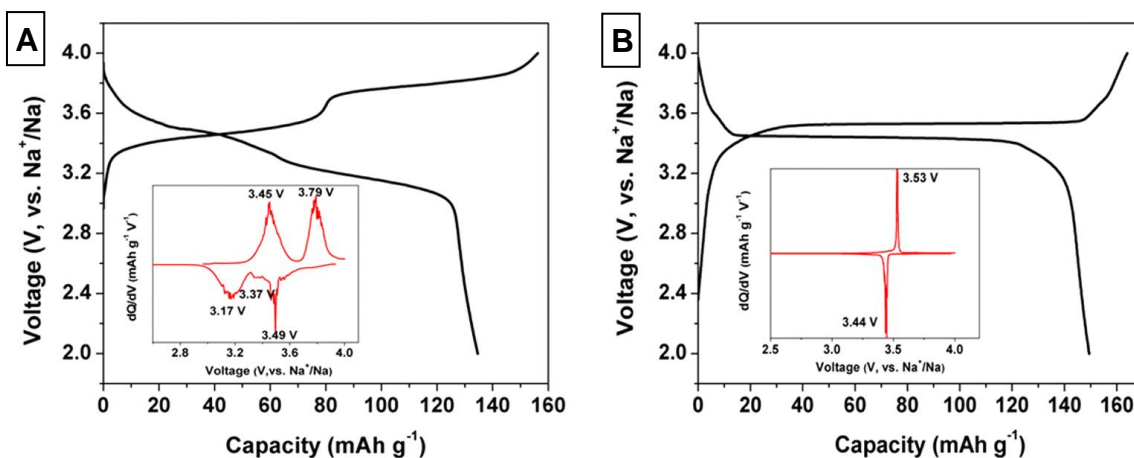
Figure 21. Galvanostatic initial charge and discharge profiles of (**A**) air-dried and (**B**) vacuum dried $Na_{2-\delta}MnHCF$ at a current of 0.1 C (15 mA/g) in the voltage range of 2.0−4.0 V [180]. The derivative curves (dQ/dV) plotted as a function of V are shown as inserts. Reprinted with permission from "Removal of Interstitial H2O in Hexacyanometallates for a Superior Cathode of a Sodium-Ion Battery" // J. Song et al., Chem. Mater., vol. 137, №7, p. 2658–2664 (2015). Copyright 2015 American Chemical Society.

1.7. Methods of synthesis of cathode materials

Hydrothermal method

Hydrothermal synthesis is used for preparation of cathode materials for lithium-ion batteries for two decades because in some special cases it allows to obtain nanosized particles and overcome problems of low electronic and ionic conductivity of the final material [85], [181]–[183]; its additional advantages are scalability and environmental safety. The main necessary equipment for hydrothermal synthesis is a high-pressure reactor which usually represents a tightly closed vessel of cylindrical shape. It may comprise furniture for connection of manometer, thermocouple, stirring impeller, safety valve and inlet/outlet valves for gas flow, solvent distillation or attachment of a coolant tube. In the

68

most primitive configuration (Figure 22) hydrothermal reactor comprises an enclosed polytetrafluoroethylene (PTFE) inner vessel with good contact between the jar and the cap and the outer steel jar with screw cap for tightening of the inner vessel and imparting to it mechanical resistance to autogenous pressure; upon heating to a temperature T>150°C gas-tightness of PTFE vessel increases due to thermal expansion of PTFE. A magnetic stir bar with PTFE coating stirs the reaction medium after setting the proper rotation speed of the magnetic stirrer, the latter depending on the viscosity of reaction mixture at the temperature of synthesis. Some examples of hydrothermal synthesis of $LiMPO_4$ (M=Fe, Mn, Co) are represented here (Table 9) because up to now the method is one of the most appropriate approach for the laboratory synthesis of miscellaneous polyanion cathode materials.
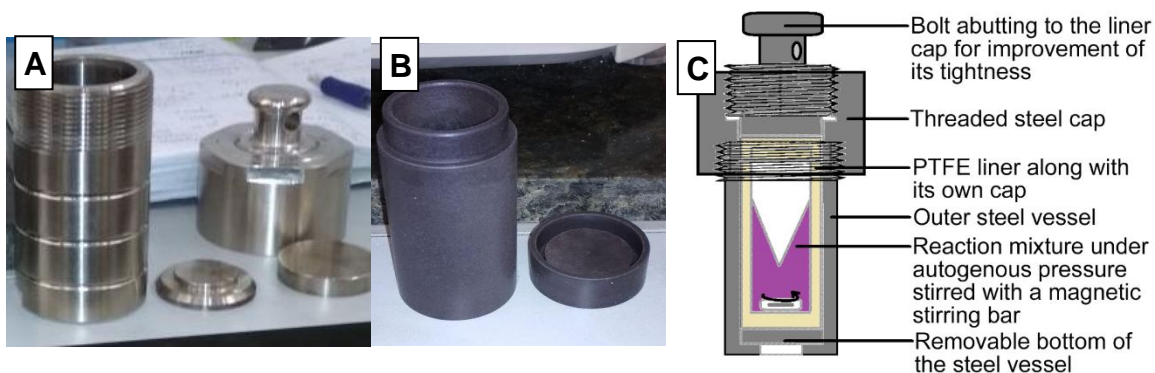

Figure 22. A photograph of a simple hydrothermal vessel (**A**) and the inner vessel (**B**); **C** – sketch of a reactor similar to one depicted in the photograph **A-B** and designed for hydrothermal synthesis on a magnetic stirring hotplate.

Table 9. Main parameters of hydrothermal synthesis of cathode materials based on LiMPO$_4$ (M = Fe, Mn, Co).

Reagents, concentrations, reducing agent and the source of carbon coating (if there is one)	Conditions of hydrothermal reaction	Apparent result	Ref.
LiOH, Co(NO$_3$)$_2$, H$_3$PO$_4$ Li:Co:P = 2:1:1, C(Co)=0.05M	pH=5.7 and pH=8.5; 220°C, 5 h	Micron particles	[184]
LiOH, FeSO$_4$, MnSO$_4$, CoCl$_2$, CoSO$_4$, H$_3$PO$_4$; Li:M:P = 3:1:1, C(M) = 0.15M; sucrose or ascorbic acid (C=1.3 g/l); for M=Fe carbon nanotubes are added (C=0.8 g/l)	150-220°C, 5 h (M=Fe); 200°C, 48 h for M=Mn, 24 h for M=Co		[185], [186]
LiOH, CoSO$_4$, (NH$_4$)$_3$PO$_4$, glucoze; Li:Co:P:glucoze = 3:1:1:0.5, C(Co) = 0.1M	Water:Benzyl alcohol (1:1 by vol.); 200°C, 8 h	Aggregates of few microns	[187]
LiOH, FeSO$_4$, Co(NO$_3$)$_2$, H$_3$PO$_4$, (NH$_4$)$_2$HPO$_4$; Li:M:P = 2:1:1	pH=7; 170°C, 10 h	100-500 nm particles	[188]

Synthesis with gel-like precursors

The Pechini method of synthesis of multicomponent ceramics has been patented in 1967, and its initial application was synthesis of lead and earth-alkaline metals titanates and niobates for the production of capacitors. Later the process was adapted for laboratory synthesis of multicomponent oxide materials. Its essence is in reaching highly homogeneous distribution of metal cations in a solution of protic organic, consequent transformation of the solution into a translucent polymer gel and thermal decomposition of the gel into a highly homogeneous oxide precursor.

Practical realization of Pechini method looks as follows [189]. Alkoxides or salts of the required metals are introduced into a solution of citric acid in ethylene glycol. It is considered that formation of citrate complexes blurs difference in behavior of different metals in solution which promotes homogeneous mixing and allows to avoid separation of

the components on the stage of polycondensation or thermal decomposition of the organic matrix. Upon heating to a temperature above 100 ºC ethylene glycol and citric acid undergo polycondensation leading to gelation of the viscous solution, mobility of molecules of metal citrate complexes being strongly hindered. Upon raising temperature to 400 ºC the polymeric matrix is burned and a highly dispersive and homogeneous amorphous powder of oxide and/or carbonate is formed. The consequent high-temperature treatment allows to obtain the required material.

Method of polyacrylamide gel is a derivative of Pechini method, wherein a polyacrylamide gel is used instead of the one formed by ethylene glycol and citric acid [189]. Polyacrylamide gel comprises an aqueous medium with complexed metal cations contained in a copolymer of polyacrylamide and N,N'-methylene-bis-acrylamide, the latter molecule functioning as the crosslinker. The general advantages of polyacrylamide method are availability of reagents and simplicity while its main drawback is high carcinogenicity of acrylamide and its combustion products. For different variations of this method common are the following stages [189]–[191]: preparation of the multicomponent solution of metal citrates and monomers; heating to ≈100°C and carrying out of the polymerization by a droplet of initiating agent (polymerization is instant); thermal treatment of the gel. N,N'-methylene-bis-acrylamide is not the only appropriate crosslinker; piperazine diacrylamide (used in gel electrophoresis) and glyoxal (used in paper production) also are applicable. Azobisisobutyronitrile (AIBN) dissolved in acetone is the most widely used initiating agent [189], [190]; in some cases polymerization occurs spontaneously just from heating [189].

Sometimes comparable results can be obtained by usage of natural gelation agents (e.g. pectin or agarose) or by preparation of a concentrated glucose syrup instead of a gel. When the desired compound cannot be obtained hydrothermally, preparation and decomposition of a gel or a syrup precursor may be a working alternative to the traditional ceramic method. For example, compounds with high potassium content cannot be obtained from aqueous solutions because of relatively high solvation energy of potassium, and in this case application of glucose-based precursor proposes a comfortable tool for finding a trade-off between phase purity and morphology of the final material.

1.8. Formulation of the problem

As one can conclude from the literature review, both approaches for increasing specific energy of the cathode are viable: increasing of the n/M ratio, where n is the number of reversibly extracted elementary charges and M is the molecular mass in g/mol; and increasing of the cathode redox potential (maybe at the cost of capacity loss). In the former case it practically means usage of the compounds with low normalized molecular mass (oxides, borates) and/or engagement of multielectron activity. In the latter case it means either usage of a redox couple with higher redox potential (e.g. Mn^{2+}/Mn^{3+} or Co^{2+}/Co^{3+} instead of Fe^{2+}/Fe^{3+}) and/or introduction of stronger electron acceptor groups, e.g. PO_4^{3-}, F^-, $P_2O_7^{4-}$ [192].

Lithium cobalt borate $LiCoBO_3$ represents a compound which seems to be the worst from the trinity $LiMBO_3$ (M=Fe, Mn, Co) from the point of reversibility of lithium intercalation. The most heavy argument for that was the amorphization of $LiCoBO_3$ upon

oxidation with equimolar portion of NO_2BF_4 [114]; but NO_2BF_4 is a very strong reagent capable of oxidizing even $LiCoO_2$ [193], and this makes the results of application of NO_2BF_4 ambiguous: it is not clear what half-reaction was the main reason of amorphization: $Co^{2+} \rightarrow Co^{3+}$ or $Co^{3+} \rightarrow Co^{4+}$. In order to provide more insight into the ability of $LiCoBO_3$ to undergo reversible electrochemical transformation, a material with a different and/or better morphology than the ones described in Refs. [114], [194] and [195] should be prepared. It can be made if a soft chemistry method is used, for example hydrothermal technique. As this technique provides possibility to get particles with some specific shape, the selection of possible solvents for synthesis media should not be limited by just water. If a material with qualitatively better morphology is obtained, its electrochemical properties may be more valuable for research and practical applications.

Na_2FePO_4F [150] and Na_2CoPO_4F [196] represent two isostructural compounds with the layered *Pbcn* structure (Figure 23, **A**). Interesting feature of Na_2FePO_4F ([150], [197]) is strong dependence of its cycling mechanism on the intercalated ion (sodium or lithium) resembling the same in the layered $ACoO_2$ (A=Li [63] or Na [198]). As for Na_xCoO_2, its explanation requires application of the advanced experimental facilities and practices including *operando* powder diffraction [198] and corroboration by the methods of density functional theory [199]. In turn, Na_2CoPO_4F is interesting mainly because of high specific energy ($<V_{oc}>\approx4.3$ V vs. Na/Na$^+$ [130]); besides, hypothetic Na_2CoPO_4F should be less prone to thermal runaways than miscellaneous oxide cathodes (e.g. $Na_{0.44}MnO_2$ [127], [137], [140], [141], [200]) which would make Na_2CoPO_4F a good competitor to them. But the structural transformations of $Na_{2-x}CoPO_4F$ were not clarified

up to the present work, and their detailed investigation would be very useful for its application in sodium-ion batteries. Finally, cobalt in Na_2CoPO_4F can be partially replaced with Mn (and Mg) with preservation of its structure. This may allow engagement of $Mn^{2+}/Mn^{3+}/Mn^{4+}$ redox transitions and reversible extraction of additional sodium, as it was already done in $Na_3MnTi(PO_4)_3$ [125]. It still wasn't realized in Na_2MnPO_4F because it has completely different structure [201] leading to poor electrochemical performance in comparison with Na_2MPO_4F (M=Fe, Co). Thus, there is a need to establish how much cobalt can be replaced with manganese with preservation of the layered structure.

The search for new structure types suitable for reversible potassium intercalation is also of great interest. As well as in the case of sodium compounds, fortunate crystal structures with a metal from 3d block and capable of potassium diffusion seem to be not so numerous as in lithium-ion cathodes. Since the electrochemical capacity of the K-based cathode materials is generally lower than the capacity of their Li- or Na-based counterparts, it is vitally important for K-ion batteries to maintain practically viable energy density through implementation of the cathode materials with higher redox potential. The second structure type the present work is devoted to has the $K_6(VO)_6O_2(PO_4)_4P_2O_7$ formula which can be re-written as $KVPO_{5\frac{1}{6}}$, or $KVPO_{5,167}$ (Figure 23, **B**) [202]. It has lower specific capacity (88 mAh/g) but still is interesting as an alternative to $KVPO_4F$ and $KVPO_4O$ [132] because it may have slightly higher cyclic stability due to presence of the residual potassium in the fully charged state. Potassium diffusion is also of great concern: it was earlier shown by DFT calculations that the straight potassium channels in $KVPO_4O$ perpendicular to the plane of the Figure 20 (**A**) do not conduct potassium and that its

diffusion occurs only along c direction (in the setting with sp.gr. *Pna*2_1) [203]. Thus, the final part of the present work is evaluation of $K_6(VO)_6O_2(PO_4)_4P_2O_7$ as a potassium-ion cathode by means of electrochemical testing and powder XRD diffraction corroborated with DFT calculations of potassium diffusion barriers.
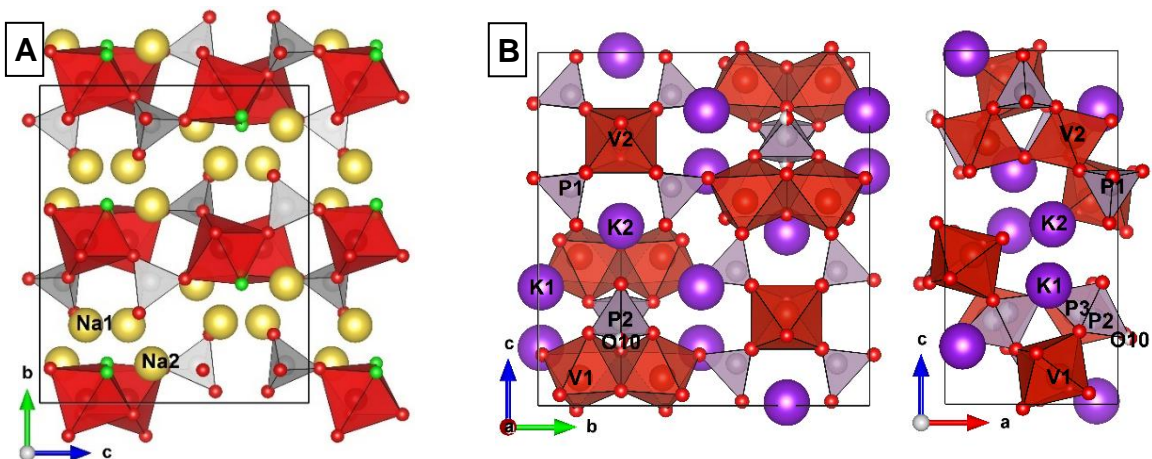

Figure 23. Crystal structures of Na_2MPO_4F (M= Fe, Co) (**A**) and of $K_6(VO)_6O_2(PO_4)_4P_2O_7$ (**B**); red octahedra stand for the coordination polyhedra of transition metals, grey tetrahedra mark PO_4 groups, big yellow and violet spheres mark sodium and potassium atoms respectively, and small red and green spheres are for oxygen and fluorine atoms respectively. V1 position contains 50% V(IV) and 50% V(V) which are ordered on the superstructural level, and V2 contains only V(IV); P1 belongs to orthophosphate and P2 and P3 atoms belong to pyrophosphates; 50% occupancies of P2, P3 and O10 atoms originate not from statistical disposition of pyrophosphate fragments but from their systematical relative shifts on the superstructural level. The Figure (**B**) is reprinted from "Reversible electrochemical potassium deintercalation from >4 V positive electrode material $K_6(VO)_2(V_2O_3)_2(PO_4)_4(P_2O_7)$" // I. V. Tereshchenko, D. A. Aksyonov, A. Zhugayevych, E. V. Antipov and A. M. Abakumov, Solid State Ionics 357, p. 115468. Copyright 2020, with permission from Elsevier. Available from https://www.sciencedirect.com/science/article/abs/pii/S0167273820305221.

2. Experimental section

2.1. Equipment for synthesis

The following equipment was used for the synthesis of the investigated compounds: high-precision balances YDP02-OD (Sartorius®) and GR-202 (A&D®), precision of weighting being ±1 mg; water purification systems Water Pro PS (Labronco®) and Direct-Q 3 UV Smart (Millipore®); magnetic stirrer C-Mag HS-7 (IKA®); 125 ml high-pressure reactor 4748 (Parr®) and a 150 ml high pressure reactor (China), both having body from a non-magnetic steel and a gas-tight PTFE liner and supporting magnetic stirring during synthesis; a 25 ml non-stirred high pressure hydrothermal reactor 4790 (Parr®); laboratory centrifuges 5804R (Eppendorf®), CM-6M (Elmi®) and ЦЛн-16 (Polikom, Russia); high energy ball mill 8000M (Spex®) with steel milling jars (V=4 ml) and balls (d=6 mm); automatic gas flow controller (Bronkhorst®); furnaces R50/250/13/B410 and L5/12/P330 (Nabertherm®); dual-zone tube furnace (SUOL, Russia).

2.2. Analysis of composition, structure and morphology

Water content in hydrates of transition metal precursors was determined by thermogravimetric analysis using TG-DS calorimeter STA-449 (Netzsch®); decomposition was conducted in a flowing mixture of $Ar:O_2$ (80:20), heating rate was set to 5–10 K/min, and after ramp the sample was kept at the final temperature for 15–30 minutes.

Metal content in the samples of $Na_2Fe_{1-x}Mg_xPO_4F$ was analyzed by means of Inductively coupled plasma mass spectrometry (ICP-MS) which was performed at ICP-OES 5100 (Agilent® Technologies).

The phase composition of $LiCoBO_3$ was characterized by powder X-ray diffraction (PXRD) using a STADI-P diffractometer (STOE®; transmission geometry, $CoK_{\alpha 1}$ radiation). The phase composition of Na_2MPO_4F (M=Mg, Mn, Fe, Co) was characterized by PXRD using an imaging plate Guinier camera G670 (Huber®; $CoK_{\alpha 1}$ radiation for M=Fe, Co and $CuK_{\alpha 1}$ radiation for all samples containing Mg or Mn). The *ex situ* synchrotron X-ray powder diffraction (SXPD) experiments were performed for different states of charge of $(Na,Li)_2FePO_4F$ at the BM01 beamline of the European Synchrotron Radiation Facility (ESRF, Grenoble). *Operando* PXRD data for Na_2FePO_4F were acquired with a D8 Advance diffractometer (Bruker®; Bragg-Brentano geometry, $CuK_{\alpha 1,2}$ radiation, LYNXEYE XE linear PSD detector), in an electrochemical cell with Be X-ray window [204]. *Operando* SXPD data for Na_2MPO_4F (M=Fe, Co) were acquired at the BM01 beamline, ESRF (λ=0.7225 Å for M=Fe and λ=0.68987 Å for M=Co) using an electrochemical cell with sapphire windows [205] briefly described in the Chapter 2.4. $K_6(VO)_2(V_2O_3)_2(PO_4)_4(P_2O_7)$ in its pristine, charged, discharged and cycled forms was characterized by means of PXRD using the same above-mentioned D8 Advance diffractometer; *operando* PXRD patterns during the first galvanostatic charge-discharge of $K_6(VO)_2(V_2O_3)_2(PO_4)_4(P_2O_7)$ were acquired at the C/40 current density with the same diffractometer using the mentioned electrochemical cell with Be X-ray window [204]. For the qualitative analysis of X-ray diffraction patterns databases PDF-2 of different dates

were used, including PDF-2 2016; the corresponding results are referred using the same numbers under which the corresponding files are stored in the database PDF-2 2016 written in the same format (#00-000-0000). When describing the results of quantitative PXRD or SXPD analysis, mass percentage is used. For the refinement of cell parameters of $Na_2Mn_{1-x}M_xPO_4F$ (M=Fe, Co) with space group $P2_1/n$ silicon internal standard was introduced. VESTA software [206] was used for the visualization of most of the depicted crystal structures.

FullProf [207] and Jana2006 [208] software were used for the Le Bail or Rietveld refinements of structures, the PO_4 fragments in all compounds being treated as rigid bodies. The anisotropic size broadening was included into the refinement of $Na_{2-x}CoPO_4F$, and the occupancy of one of the two non-equivalent sodium atoms A2 in $Na_{1.44}CoPO_4F$ was fixed to zero in order to prevent it from becoming negative.

Microstructure characterization of $LiCoBO_3$ was performed with a scanning electron microscope (SEM) NVision 40 (Carl Zeiss®); the same of the Na_2MPO_4F (M=Fe, Co) samples was performed with a focused ion beam-scanning electron microscope Helios G4 PFIB UXe (FEI®); the same of the $K_6(VO)_2(V_2O_3)_2(PO_4)_4(P_2O_7)$ samples was performed by a field emission scanning electron microscope (FE-SEM) Quattro S (FEI®). Compositional characterization of $(Na, Li)_{2-y}FePO_4F$ was performed using the energy-dispersive X-ray (EDX) attachment Energy 350X-Max 80 (INCA®) of an NVision 40 scanning electron microscope and the same of Na_2CoPO_4F and $K_{6x}(VO)_2(V_2O_3)_2(PO_4)_4(P_2O_7)$ was performed using the energy dispersive X-ray

spectroscopy (EDS) system Octane Elite Super (EDAX®) of the Helios G4 PFIB UXe scanning electron microscope.

Average oxidation state of iron in the samples of $Na_{1.55}FePO_4F/C$ and $(Na,Li)_{1.5\pm\delta}FePO_4F/C$ obtained by electrochemical oxidation (so-called half-charged samples) was confirmed by means of Mössbauer spectroscopy at ^{57}Fe nuclei at room temperature. ^{57}Co in a rhodium matrix ($^{57}Co/Rh$) was used as the source of γ-quants. Isomeric shifts are represented relatively to a highly pure α-Fe standard. Experimental data were treated using "UnivemMS" software. The data acquisition was conducted at the department of Radiochemistry of the Department of Chemistry in Lomonosov Moscow State University.

2.3. Electrochemical measurements

Electrode materials were prepared by grinding with a mortar and a pestle of mixtures containing the active component, carbon black (Super P®) and polymer binder polyvinylidene difluoride (PVdF, Solef), in the following mass ratio – 75:15:10 for $LiCoBO_3/C$ and Na_2FePO_4F/C, 75:12.5:12.5 for Na_2CoPO_4F/C and 70:20:10 for $K_6(VO)_2(V_2O_3)_2(PO_4)_4(P_2O_7)$. The ground mixtures were turned into slurries by addition of anhydrous N-methyl-2-pyrrolidinone (Sigma Aldrich, anhydrous, 99.5%), the mass fraction of the solid component of the electrode slurry being 20%, followed by a thorough mixing with N-methyl-2-pyrrolidinone using mortar and pestle. The obtained slurries were put onto aluminum foil by a tape casting coater. The electrode coating was dried in an oven, coated aluminum sheets were mechanically treated by steel rollers and electrodes of diameter 16 mm were cut from them. Then the round electrodes were weighed on a high-

precision balance and additionally dried at 110°C for 2 hours under vacuum (p<10 torr); electrodes with $LiCoBO_3$ were being dried for 3 hours. The mass of the active material on every electrode was calculated by subtraction of masses of non-active components (Al foil, PVdF and carbon black Super P®) from the gross-mass of the electrode. For conducting the electrochemical experiment two-electrode coin-type electrochemical cells were assembled in a glove-box with argon atmosphere (MBraun®), the H_2O and O_2 content being <1 ppm. Disks from borosilicate glass membranes (Whatman® of Grade GF/A or equivalent) were used as the separators with diameter 20 mm were dried at 130°C for 15 hours under vacuum (p<10 torr) and then were used as separators. Metallic lithium (Sigma Aldrich, 99.9%), sodium (Sigma Aldrich, 99.8%) or potassium (Sigma Aldrich, 98%) was rolled into foil and used without further purification as the counter-electrode in a corresponding electrochemical half-cell.

In lithium-ion half-cells with cathodes based on $LiCoBO_3$ or Na_2FePO_4F 1M solution of $LiPF_6$ in the mixture of ethylene carbonate (EC) and dimethyl carbonate (DMC) (volume ratio 1:1; vendor – Sigma Aldrich, <15 ppm H_2O, <50 ppm HF) was used for all experiments at room temperature, and 1M solution of $LiPF_6$ (Sigma Aldrich, battery grade) in sulfolane (Sigma Aldrich, 99%) was used for the experiment at 75°C; sulfolane had been dried with 4Å molecular sieves (Sigma Aldrich). In sodium-ion half-cells with cathodes based on Na_2FePO_4F 1M solution of $NaClO_4$ (Sigma Aldrich, 98%) in a mixture of 95 vol.% of propylene carbonate (PC; Sigma Aldrich, anhydrous, 99.7%) and 5 vol.% of fluoroethylene carbonate (FEC; Sigma Aldrich, anhydrous, 99%) was used. $NaClO_4$ salt was dried at 130°C for 15 hours under vacuum (p<10 torr).

In sodium-ion half-cells with cathodes based on Na_2CoPO_4F 1M solution of sodium di(fluoro)oxalatoborate in sulfolane was used for the initial electrochemical characterization of Na_2CoPO_4F/C and 1M solution of $NaPF_6$ (Sigma Aldrich, 98%) in a mixture of 50 vol.% of EC (Sigma Aldrich, anhydrous, 99%) and 50 vol.% of PC (Sigma Aldrich, anhydrous, 99.7%) was used for *operando* SXPD investigation. Sodium di(fluoro)oxalatoborate solution was prepared by the exchange reaction of lithium difluoro(oxalato)borate (LiDFOB, Sigma Aldrich) with stochiometric amount of NaF (98%) in sulfolane (Sigma Aldrich, 99%) which had been dried with 4Å molecular sieves (Sigma Aldrich). $NaPF_6$ salt was dried at 90°C for 15 hours under vacuum (p<10 torr).

In potassium-ion half-cells with cathodes based on $K_6(VO)_2(V_2O_3)_2(PO_4)_4(P_2O_7)$ 0.6M solution of KPF_6 (Sigma Aldrich, 99%) in a mixture of 50 vol.% of EC (Sigma Aldrich, anhydrous, 99%) and 50 vol.% of diethyl carbonate (Sigma Aldrich, anhydrous, 99%) was used for all electrochemical experiments. KPF_6 salt was dried at 90°C for 15 hours under vacuum (p<10 torr).

If not stated otherwise, electrochemical measurements were conducted at room temperature (which was set at 25°C). Acquisition of galvanostatic charge-discharge curves was performed on a multichannel potentiostat-galvanostat P-20X8 (Elins) or potentiostat-galvanostat VMP-3 (Biologic®; EC-Lab® software). Potentiostatic intermittent titration technique (PITT) of Na_2FePO_4F was performed using the same potentiostat-galvanostat VMP-3 and EC-Lab software. Anhydrous propylene carbonate (Sigma Aldrich, 99.7%) was used for washing non-aqueous electrolytes from all electrodes which were planned to be analyzed by PXRD and/or EDX spectroscopy.

2.4. Electrochemical cell for operando synchrotron diffraction

The overall scheme of the electrochemical cell for operando SXPD is represented in Figure 24. The cell consisted of the "inner" and "outer" current collectors; the "inner" collector was made of brass, and the "outer" one was made from aluminum. One or two O-rings provided gas sealing and electrical isolation between the outer and inner collectors. The conical opening from the cathode side was made with the opening angle ≈120°. The window for incoming and outcoming X-rays was made from thin (≈0.2 mm) sapphire single-crystal wafer. Bragg reflections from the sapphire single-crystal windows contributing to the X-ray diffraction pattern have been eliminated ("masked") using the data processing software.

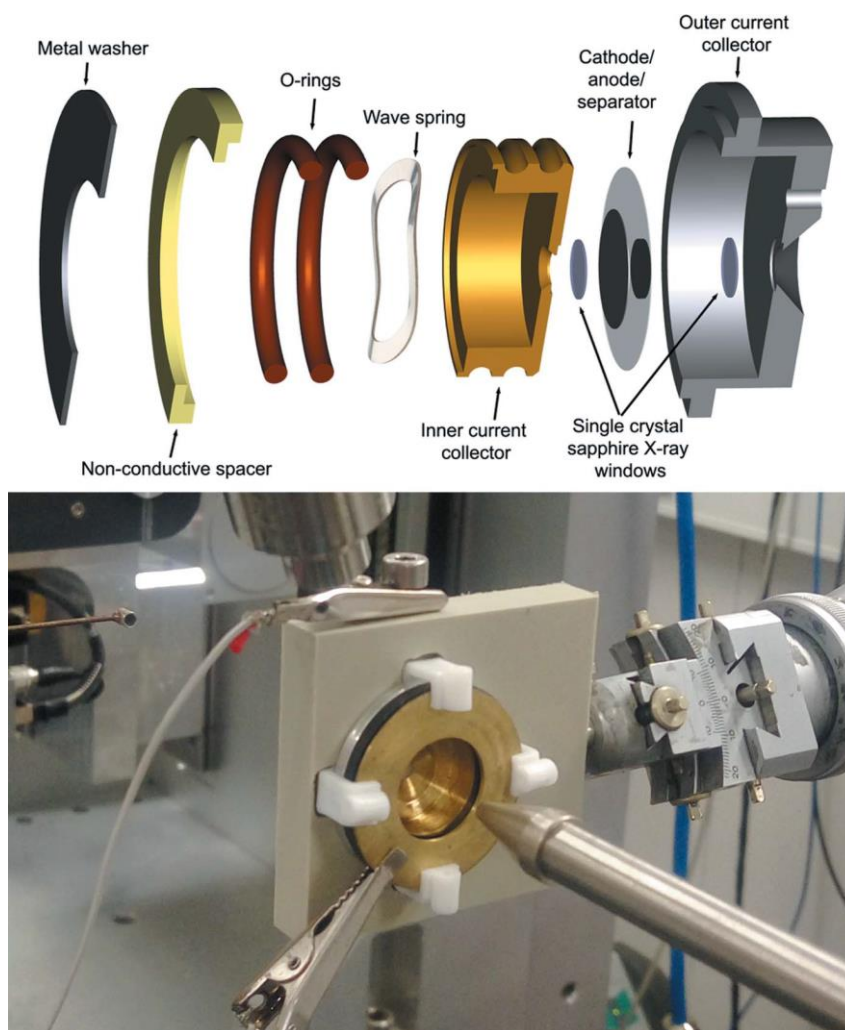Figure 24. (**Up**) Exploded view and (**Down**) photograph of the novel operando electrochemical cell [205]; reprinted under the CC-BY 4.0 license from the Journal of Synchrotron Radiation 25 (2), p. 468-472 (2018).

2.5. Synthesis of LiCoBO₃

Reproduced in part from "Novel synthetic approaches to LiCoBO₃ cathode material and its electrochemical properties" // O. A. Drozhzhin, I. V. Tereshchenko and E. V.

10.707 g (37.5 mmol) of $Co(NO_3)_2 \cdot 5.70H_2O$ (Labteh, 99%) were dissolved in 15 ml of distilled water; 3.617 g (86.25 mmol) of $LiOH \cdot H_2O$ (>98%) and 0.050 g of ascorbic acid were dissolved in 30 ml of distilled water. The solution of lithium hydroxide was added dropwise to the solution of cobalt nitrate, the latter being stirred vigorously with a magnetic stirrer; a bluish-green precipitate was formed at the addition of lithium hydroxide solution, the precipitate gradually getting a skin color. The obtained product was thoroughly purified by three washings with deionized water and centrifugations. Few ml of water, 1.573 g of $LiOH \cdot H_2O$ (>98%), 2.318 g of H_3BO_3 (Reakhim, 99.8%), the whole yield of the freshly precipitated cobalt hydroxide (wet with decanted water) and 5 ml of pyridine were placed in series into a PTFE vessel of the volume 29.5 ml; the thick suspension was mixed and diluted with distilled water to 19 ml and a magnetic stir bar was placed inside. The PTFE vessel was placed into a non-stirred high-pressure hydrothermal reactor 4790 (Parr®) which was then tightly sealed, purged with nitrogen and placed into the heater supplied with a custom magnetic stirrer. The reaction mixture was heated to 250 °C and kept at this temperature for 6 h with constant and thorough stirring. After hydrothermal treatment, the sample was purified by several washings and centrifugations, dried, and a fraction of the sample was ball-milled with acetylene black (5 mass %). The milled mixture was calcined for one hour at 500°C in a dual zone tubular furnace under argon flow with presence of nickel metal powder as the absorber of residual oxygen and quenched after the calcination.

2.6. Synthesis of Na₂FePO₄F

5.686 g of $(NH_4)_2Fe(SO_4)_2\cdot6H_2O$ (Sigma Aldrich, 99%), 1.8 g of ascorbic acid, and 1.8 g of glucose were dissolved in distilled water adjusting the volume to 30 mL. Then, 20 mL of 4.6 M sodium hydroxide solution (Sigma Aldrich, 98%) was added to the mixture dropwise under vigorous stirring; ascorbic acid prevented partial oxidation of iron (II) during the alkalization. 4.493 g of sodium fluoride (98%) and 25 mL of 95% ethanol were added quickly, and the mixture was rapidly sealed into a 150 ml PTFE lined high-pressure vessel along with a magnetic bar of appropriate size; the fill factor was 50%. The reaction mixture in the autoclave was heated to 200 °C and kept at this temperature for 8 h under magnetic stirring and autogenous pressure. Carefully washed and dried Na_2FePO_4F was carbon-coated using annealing with D-glucose for 2 h at 600 °C under an inert atmosphere.

For the ion exchange of sodium for lithium in Na_2FePO_4F the same lithium-ion electrolyte as in the electrochemical measurements was used.

2.7. Synthesis of Na₂CoPO₄F

First, 4.05 g $CoSO_4\cdot6.36H_2O$ (Reakhim, 99.5%) were dissolved in 25 ml of deionized water, and separately of this 15.3 g of $CH_3COONa\cdot3H_2O$ (99%), 3.2 g of sodium fluoride (98%) and 31.685 g of $Na_2HPO_4\cdot12H_2O$ (Sigma Aldrich, 99%) were introduced

together into 25 ml of deionized water and a suspension in their saturated solution was formed. Two solutions were heated up to 75°C and the $CoSO_4$ solution was added dropwise to hot suspension upon stirring to form a violet precipitate. Then 25 ml of 95% aqueous ethanol solution was added to the resulting suspension and the mixture was transferred into a 125 ml Parr® PTFE lined high-pressure vessel along with a magnetic bar of appropriate size. The final fill factor was approximately 60%. The vessel was sealed and placed on a hotplate with magnetic stirring inside of a thermal-insulating case. The reaction mixture in autoclave was kept at 200°C for 8 hours under magnetic stirring and autogenous pressure. After cooling the reaction vessel, the product was washed with deionized water several times with centrifugation, the resulting powder of Na_2CoPO_4F was dried in a Petri dish under air flow and used for further carbon coating. For the carbon-coating uncoated Na_2CoPO_4F sample was thoroughly mixed with 25 mass % of glucose using mortar and then was calcined for two hours at 600°C in a tubular furnace under argon flow with presence of nickel metal powder as the absorber of residual oxygen and quenched after the calcination.

2.8. Synthesis of $Na_2M^I_{1-y}M^{II}_yPO_4F$ (M^I=Fe/Co; M^{II}=Mn/Mg)

Solid solutions of $Na_2Mn_{1-x}Fe_xPO_4F$ and $Na_2Co_{1-x}Mn_xPO_4F$ (x=0, 0.2, 0.4, 0.6, 0.8) were obtained by the same technique as Na_2CoPO_4F, but stirring at the time of these syntheses was not available, and that was why the total content of the transition metals was set three times higher (0.6 mol per liter of the final precursor suspension), and the concentration of sodium was 20% lower; a non-stirred high-pressure hydrothermal reactor Parr 4790 (volume 25 ml) was used. Compounds with formula $Na_2Fe_{1-x}Mg_xPO_4F$ were

synthesized by the same technique as the one used for Na_2FePO_4F, but the temperature of the ferrous solution was lowered below 3°C. Purity grade of both $MnSO_4 \cdot H_2O$ (vendor Sigma Aldrich) and $MgSO_4 \cdot 7H_2O$ (vendor Reakhim) was 99%.

2.9. Synthesis of $K_6(VO)_2(V_2O_3)_2(PO_4)_4(P_2O_7)$

Reproduced from "Reversible electrochemical potassium deintercalation from >4 V positive electrode material $K_6(VO)_2(V_2O_3)_2(PO_4)_4(P_2O_7)$" // I. V. Tereshchenko, D. A. Aksyonov, A. Zhugayevych, E. V. Antipov and A. M. Abakumov, Solid State Ionics 357, p. 115468. Copyright 2020, with permission from Elsevier. Available from https://www.sciencedirect.com/science/article/abs/pii/S0167273820305221.

$K_6(VO)_2(V_2O_3)_2(PO_4)_4(P_2O_7)$ was synthesized via a two-stage ceramic route. On the first stage 0.573 g of V_2O_5 (Sigma Aldrich, 98%) were introduced into aqueous solution containing 2.8125 g of $H_2C_2O_4$ (Sigma Aldrich, 98%), 0.850 g of KH_2PO_4 (Reakhim, 99%) and 10 ml of deionized water. After stirring for 30 minutes in air the greenish-blue color characteristic of vanadium (IV) was established. Then additionally 5.63 g of D-glucose (Sigma Aldrich, 99.5%) were dissolved, the obtained solution was dried and the residue was calcined in air in a muffle furnace at 350°C for 5 hours. Yellowish-green foam obtained after the calcination was thoroughly ground in a mortar and pressed into a pellet; the pellet was calcined at 425°C for 4 hours under argon flow which deliberately was not purified from remaining traces of oxygen; the used argon was of high purity grade claiming oxygen content limited by $2 \cdot 10^{-4}$ vol. %.

2.10. Density functional theory calculations

General points

Total energies and optimized geometries were calculated with the Vienna Ab Initio Simulation Package (VASP) [209]. The Perdew−Burke−Ernzerhof (PBE) flavor of the generalized gradient approximation (GGA) and projected augmented wave (PAW) method with minimum number of valence electrons were employed [210]. The standard library potentials "V", "Fe", "Co" (3d and 4s valence states), "P", "F", "O", "Na", and "Li" were used. To take into account the strongly correlated character of the d-electrons of Fe and Co, a Hubbard-like correction was added within the Dudarev scheme [211] and U value of 4 eV for Fe and 3.4 eV for Co. To ensure the convergence of wave functions to ground state, the U-ramping approach was employed [212]. Gaussian smearing with smearing width of 0.1 eV was used for Brillouin-zone integrations. All calculations for Na_2MPO_4F (M=Fe, Co) were performed with spin polarization with the ferromagnetic ground state and tetrahedron method with Blöchl corrections for partial occupancies; for calculations of density of states of $Na_{2-x}CoPO_4F$ the increased k-point mesh of 8×4×4 was used. The convergence study showed that the energy cutoff of 400 eV and k-point grid of 5×2×2 (for $(Na,Li)_{2-x}FePO_4F$) and of 4×2×2 (for $Na_{2-x}CoPO_4F$ and $K_6(VO)_2(V_2O_3)_2(PO_4)_4(P_2O_7)$) are

sufficient for reliable description of lattice constants and formation energies. To eliminate the influence of Pulay error, the lattice optimization (ISIF = 4) was performed at constant volume for several contracted and expanded cells (7 points), followed by a third-order polynomial fit of the obtained energies. The relaxation was performed until the forces acting on atoms were smaller than 50 meV/Å, which is enough for obtaining total energies within 1 meV/atom precision. The cluster expansion method, such as implemented in the ATAT code, was used to study phase stabilities for $Na_{1-x}LiFePO_4F$ and $Na_{2-x}MPO_4F$ (M=Fe, Co) [213]; after every Na removal, full optimization of the unit cell and atomic positions was performed.

Na_2FePO_4F

The initial crystal structure of Na_2FePO_4F with the *Pbcn* space group was taken from the experiment. The fully charged compounds relevant for charging in a Na-ion cell ($NaFePO_4F$) were obtained by removing Na atoms from either A1 or A2 sites. The atomic structure of the half-charged $Na_{1.5}FePO_4F$ compound was found by screening all possible configurations after removal of 0.5 Na (15 configurations in total). To understand the structural transformations during charging in the Li-ion cell, the discharged ($NaLiFePO_4F$) and half-charged ($Na_{0.5}LiFePO_4F$) atomic structures were constructed by substituting Na

by Li and considering all possible atomic arrangements. The effects of positional disorder have not been taken into account; in particular, the $Na_{0.5}LiFePO_4F$ structure has been found to have $P2_1/b$ space group, while in the experiment due to disordered locations of Na it still has *Pbcn* space group. To account for the contribution of lattice vibrations to the free energies, the harmonic approximation was employed, as implemented in the PHONOPY code [214]. The force constants were calculated using density functional perturbation theory with increased FFT meshes in VASP. By comparing phonon density of states (PHDOS) and thermodynamic properties of 72-atom and 144- atom supercells, it was found that the 72-atom supercell provides reliable results.

Potassium diffusion in $K_6(VO)_2(V_2O_3)_2(PO_4)_4(P_2O_7)$

The activation energies for potassium migration were determined using the nudge elastic band (NEB) method as implemented in VASP code. The error in activation energy due to limited relaxation precision and small polaron−vacancy/cation binding intervention was on the order of 0.1 eV.

3. Results and discussion

3.1. LiCoBO₃

The results of this chapter are described in "Novel synthetic approaches to LiCoBO$_3$ cathode material and its electrochemical properties" // O. A. Drozhzhin, I. V. Tereshchenko and E. V. Antipov, Ceram. Int. 43 (5), p. 4670-4673. Copyright 2017, with permission from Elsevier. Available from https://www.sciencedirect.com/science/article/pii/S0272884216324178.

During the investigation of the hydrothermal synthesis of LiCoBO$_3$ following peculiarities of the synthetic process have been found which must be taken into account. First, presence of an antioxidant (e.g. ascorbic acid) was found to be necessary to prevent the oxidation of freshly prepared Co(OH)$_2$ in alkaline media of solutions of LiOH or LiBO$_2$; second, stirring of the suspension during the synthesis was necessary to prevent crystallization of cobalt hydroxide and formation of crystalline Li$_3$B$_5$O$_8$(OH)$_2$ or LiBO$_2$. Third, a high concentration of the precursor suspension (above 1.5 mol/l) was desirable to prevent the occurrence of an admixture of crystalline Co(OH)$_2$ in the final product. In the second step (calcination with carbon) the most important is to sustain the proper amount of oxygen in argon, shortening of the calcination time and avoidance of usage of carbon additives carbonizing *in situ* (because of cobalt reduction).

Unit cell parameters and atomic coordinates of LiCoBO$_3$ obtained hydrothermally were refined by the Rietveld method using the structure model of LiCoBO$_3$ from Ref. [215] with space group *C*2/*c* (Figure S1). The refined unit cell parameters *a*=5.1292(2) Å,

b=8.8623(3) Å, c=10.1082(3) Å, β=91.311(3)°, V=459.4(2) Å^3 are in accordance with those from Ref. [215] and [114]. The only detected impurity was 4.5 mass % of $Co(OH)_2$. Pyridine molecule was chosen as a potential adsorbate which hypothetically could attach itself to the surface of $LiCoBO_3$ by means of occupation of the boron free orbital by the nitrogen electron pair. This might make *ab* crystallographic plane of growing crystals of $LiCoBO_3$ less accessible for adsorption of lithium and cobalt ions and shorten the size of the final particles selectively in the [001] crystallographic direction.

In the SEM micrograph of the sample obtained in water-pyridine mixture and subjected to a short calcination at 500°C (inset in the Figure S1) one may distinguish micron-sized agglomerates of sintered plates. But in spite of sufficient phase purity and moderate particle size the sample has demonstrated negligible specific capacity and cyclability (Figure 25) which are also not better than the electrochemical characteristics of $LiCoBO_3$ obtained through ceramic [114] or sol-gel route [195].
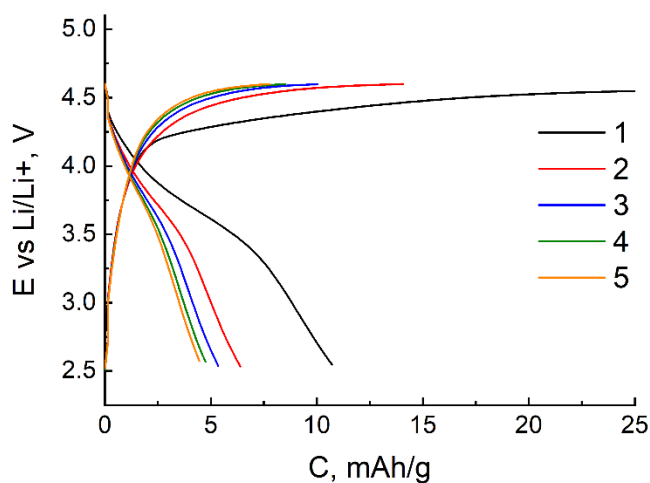
Figure 25. The first five galvanostatic cycles of $LiCoBO_3$/C at the current density C/20.

The poor behavior of $LiCoBO_3$ may be explained as follows. Since the divalent cobalt is known to occupy tetrahedral sites in complex polyanionic compounds of lithium and cobalt (Li_2CoSiO_4 [216], $Pna2_1$ $LiCoPO_4$ [217], Na_2CoSiO_4 [218]), then an irreversible "disproportionation" of CoO_5 bipyramids into tetrahedra and distorted octahedra may occur upon partial lithium extraction and consequent rotations of individual BO_3 triangles around the axis perpendicular to the plane of triangle. One should expect the same disproportionation in $LiFeBO_3$ and m-$LiMnBO_3$ but there it can be reversible due to zero ligand field stabilization energy for Mn^{2+} and Fe^{3+} ions; by the way, these rotations might be responsible for their poor rate capability known from the literature.

3.2. Phase formation in the Na_2MPO_4F (M=Mg, Mn, Fe, Co) system

In order to complete the first step of synthesis of Na_2MPO_4F (hydrothermal stage) long duration ($\geq$8 hours), high temperature ($\geq200°C$) and high sodium concentration ($\approx4.5M$) are necessary; otherwise a fluoride-phosphate (II) M_2PO_4F (M=Fe, Co) or a cobalt phosphate-hydroxide with unknown composition forms; the latter phosphate-hydroxide lacks sodium as EDX data evidence. Other problem was presence of inseparable admixtures detected by PXRD: Na_2PO_3F (#01-070-1013), NaF (#00-036-1455), maricite $Na(Fe,Mn)PO_4$, Fe_3O_4 or $Co(OH)_2$. Na_2PO_3F was visible in PXRD patterns if the synthesis temperature was $\geq230°C$, sodium fluoride – if fluoride ion concentration in the bittern was higher by more than 30% relatively to ones specified in experimental section or in the case the product precipitate was not washed from the bittern for a time interval longer than 40 min from the moment of the reactor quenching. Maricite $NaMPO_4$ (M=Fe, Mn) was found

if the bittern pH was less than 10, Fe_3O_4 – in the case the NaOH solution was injected awry or its molar quantity was slightly higher than one specified in the experimental section, $Co(OH)_2$ – if bittern pH was higher than 11. Addition of ≈30 vol.% of a solvent with low relative permittivity (ethanol) was motivated by its noticeable capability to slow down the growing of product particles while not spoiling the final phase composition by admixtures. It is worth mentioning that it was impossible to synthesize Na_2NiPO_4F (#01-080-9880) by the procedure proposed for Na_2CoPO_4F. At the stage of calcination with glucose reduction of iron (II) or cobalt (II) with absorber of residual oxygen by means of a gas phase transport reaction was a problem, that was why powders of two different metals were used as absorbers of residual O_2: iron powder was used for materials containing Fe^{2+} and nickel powder was used for materials containing Co^{2+}, the latter were kept at 600°C for no longer than 1 hour and were quenched right after calcination for minimization of metallic cobalt admixture in the final material.

Unit cell parameters of Na_2MnPO_4F (Table S2), Na_2FePO_4F (Table S3) and Na_2CoPO_4F (Table S4) were refined by the Rietveld method using structure models of Na_2FePO_4F (#01-078-5219 [150]) and Na_2CoPO_4F (#01-070-9643 [196]) with space group *Pbcn* and Na_2MnPO_4F (#01-087-0467 [201]) with space group $P2_1/n$; the results of Rietveld refinement are consistent with the literature data. Unit cell parameters of solid solutions $Na_2Mn_{1-x}Fe_xPO_4F$ (x=0.2, 0.4, 0.6, 0.8; Table S2), $Na_2Fe_{1-x}Mg_xPO_4F$ (x=0.1, 0.25 and 0.5; Table S3) and $Na_2Co_{1-x}Mn_xPO_4F$ (x=0.2, 0.4, 0.6, 0.8; Table S4) were refined by Le Bail method. Molar ratio between metals in the samples of $Na_2Fe_{1-x}Mg_xPO_4F$ was confirmed by ICP-MS for exclusion of presence of some amorphous magnesium-rich

admixtures with unexpected composition (Table S5); then the relative deviation of the ratio between sodium and divalent metals does not exceed 10%. Elemental composition of Na_2CoPO_4F was found to be consistent with the formula after the EDX analysis revealed the ratio of Na:Co:P=2.00:0.89:0.96 (standard deviation 5 %; see a representative spectrum in Figure S4). Le Bail refinement of the $Na_2Mn_{1-x}Fe_xPO_4F$ cell parameters confirmed that its structure switches to the layered type only at a very high iron content. At the same time replacement of 40 at.% of cobalt in Na_2CoPO_4F with manganese with preservation of the layered structure (Table S4 and Figure S5) shows a potential possibility to get a high voltage cathode material with formal theoretical capacity >170 mAh/g, if Mn^{2+} and Co^{2+} are fully oxidized to oxidation states +4 and +3 respectively. 0.6 sodium atoms per formula unit might remain in the interlayer space for stabilization of the charged structure.

3.3. Na₂FePO₄F

Reproduced in part with permission from "The Role of Semilabile Oxygen Atoms for Intercalation Chemistry of the Metal-Ion Battery Polyanion Cathodes" // I. V. Tereshchenko et al., J. Am. Chem. Soc. 140 (11), p. 3994–4003 (2018). Copyright 2018 American Chemical Society. Available from https://pubs.acs.org/articlesonrequest/AOR-YJh64uPKIstIQxXrxm5f.

The proposed technique of combined solvo-hydrothermal synthesis allows to obtain reproducibly the single-phase samples of Na_2FePO_4F/C. But in the present work its SXPD pattern is represented instead of PXRD for the sake of better resolution and correspondingly better Rietveld refinement (Figure S2). The represented pattern has been acquired right before the *operando* SXPD acquisition in a specially designed lithium half-

cell, the result is described further below. Micrograph of the Na_2FePO_4F/C sample (inset from Figure S2) demonstrates slightly anisotropic particles with the short dimension less than 500 nm. This sample was taken for further investigation as an example of polyanion phase able to work in both sodium- and lithium-ion half-cells and demonstrating strong dependence of the deintercalation potential on the state of charge (which is referred to as SOC below), see the Figure 26 (**A**, **B**). Data from PITT (Figure 26, **C**, **D**) also demonstrate clear difference between mechanisms of cycling in lithium- and sodium-ion half-cells already in the second half of the first anode branch. For comparison of galvanostatic curves with phase transitions occurring under application of voltage and for estimation of the contribution to these transformations of solid-solution behavior caused by ion exchange of sodium for lithium, *operando* SXPD experiment was performed in a lithium-ion half-cell, and an *operando* PXRD experiment was performed in a sodium-ion half-cell, for the latter a laboratory diffractometer with Bragg-Brentano geometry was used (Figure 26, **E**, **F**; reflections from the cell components in the figure **F** are marked with an asterisk). Three-dimensional SXPD pattern reveals both solid-solution-like behavior of Na_2FePO_4F caused by ion exchange visible from reversible shifts of reflections at the second cycle (Figure 26, **E**, **blue color**), and the presence of reflections characteristic for purely sodium-ion half-cell – these of $Na_{1.5\pm\delta}FePO_4F$ and $NaFePO_4F$ (peaks stained with green and red colors in Figure 26, **E**, **F**). As the quantitative *operando* SXPD analysis requires structure models of $Na_{1.5\pm\delta}FePO_4F$ and $NaFePO_4F$, these compounds were obtained in a relatively pure form by means of a one-time half-charge of Na_2FePO_4F/C and separately by its one-time full charge and consequent washing of both samples with anhydrous propylene carbonate. For

96

confirmation of the Fe^{2+}:Fe^{3+} molar ratio in the half-charged sample a ^{57}Fe Mössbauer spectrum was acquired, wherein the deviation from the Fe^{2+}:Fe^{3+} ratio expected from the passed charge does not exceed 1%. (Figure S6, Table S7).

Electrodes with the $Na_{1.5\pm\delta}FePO_4F$ and $NaFePO_4F$ compositions were subjected to *ex situ* SXPD and EDX analyses. SXPD data allowed to establish the proper space group of $Na_{1.5\pm\delta}FePO_4F$ ($P2_1/b11$) and to perform Rietveld refinement of its structure (Figure S7) and of the structure of $NaFePO_4F$ (Figure S8). Their unit cell parameters and R-factors are represented in Table S6, atomic coordinates – in Table S9 and Table S10. The monoclinic distortion of the *Pbcn* unit cell of $Na_{1.5\pm\delta}FePO_4F$ was selected thanks to a very weak reflection at d≈11.5 Å being absent in initial and fully charged states and assigned to have Miller indexes (010). The reliability of these refinements is confirmed by correct bond valence sums for all atoms (Table S9, Table S10) and correct bond lengths of first coordination spheres (Table S11, Table S12). The refined Na/(Fe+P) ratio is equal to 0.775 and is fully consistent with the ratio obtained from EDX spectra (Table S13). As a result, splitting of the active alkaline position A2 (the one undergoing depletion) into the $A2_1$ and $A2_2$ positions with almost complete depletion of the former coupled with charge ordering of Fe^{2+} and Fe^{3+} (BVS(Fe1)=1.86(3), BVS(Fe2)=2.78(5)), has finally been proven.
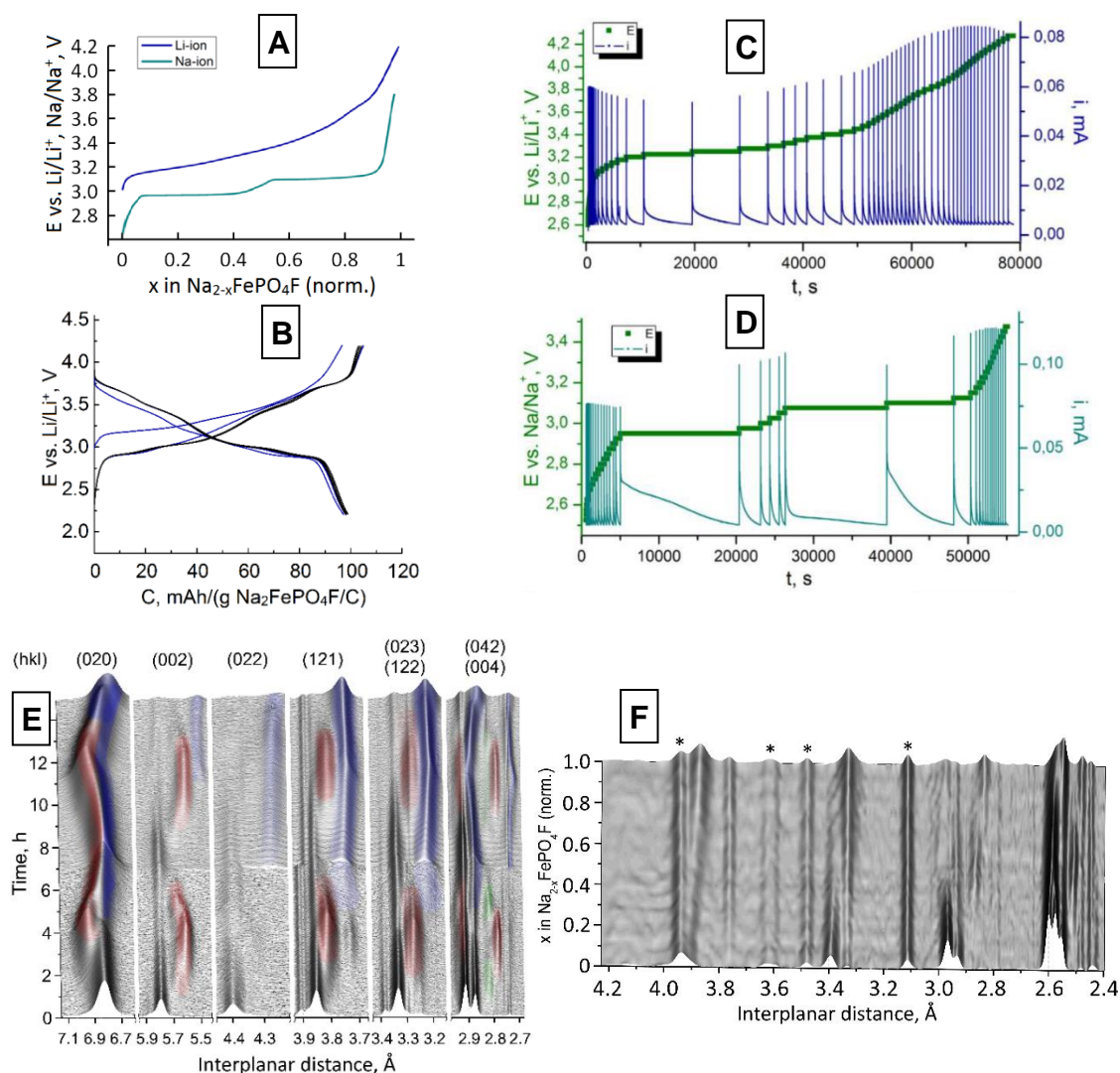
Figure 26. (**A**) The first galvanostatic charge curve of half-cells with Na_2FePO_4F/C with current density C/10: lithium-ion (**blue**) and sodium-ion (**cyan**); (**B**) galvanostatic charge-discharge curves of a lithium-ion half-cell with Na_2FePO_4F/C with current density C/10: 1st and 2nd cycles (**blue**) and 3rd-5th cycles (**black**); (**C, D**) PITT curves of Na_2FePO_4F/C acquired in a lithium-ion (**C**) and a sodium-ion (**D**) half-cell and the corresponding voltage steps (**green**), the residual current being C/50 and the voltage step being 25 mV; (**E**) main SXPD reflections with their Miller indexes acquired *operando* in a lithium-ion half-cell, the colors correspond to compounds as follows: **green** is for $Na_{1.55}FePO_4F$, **blue** – for $(Na,Li)_{2-x}FePO_4F$, **red** – for $NaLi_yFePO_4F$ and **grey** is for Na_2FePO_4F and for reflections of other phases without miller indices; intensity axis has logarithmic scale; (**F**) – PXRD pattern of the 1st galvanostatic charge of Na_2FePO_4F/C in a sodium-ion half-cell acquired *operando* using laboratory diffractometer. Reprinted with permission from "The Role of Semilabile Oxygen Atoms for Intercalation Chemistry of the Metal-Ion Battery Polyanion Cathodes" // I. V. Tereshchenko et al., J. Am. Chem. Soc. 140 (11), p. 3994–4003 (2018). Copyright 2018 American Chemical Society. Available from https://pubs.acs.org/articlesonrequest/AOR-YJh64uPKIstIQxXrxm5f.

98

The monoclinic distortion caused by the charge ordering of Fe^{2+} and Fe^{3+} was suggested earlier [150] from other structures known at that time but was not confirmed directly. This feature of $Na_{1.5\pm\delta}FePO_4F$, from now referred to as $Na_{1.55}FePO_4F$, allows to suppose the connection between raising of the deintercalation potential of $Na_{2-x}FePO_4F$ above x>0.5 with additional inductive effect "felt" by every Fe^{2+} ion because of newly appeared Fe^{3+} neighbor and with the shift of $O6\equiv O2_2$ atom closer to the remaining sodium atom in $A2_2$ position.

For the description of mass composition using *operando* SXPD data acquired in the lithium-ion half-cell the model of Na_2FePO_4F and the newly obtained structure model of $Na_{1.55}FePO_4F$ were taken into refinement along with two additional models of phases which had undergone lithium-ion exchange. These additional models with space group *Pbcn* and "floating" unit cell parameters were introduced to mark sodium-rich and sodium-depleted states of $(Na,Li)_{2-x}FePO_4F$ over the whole range of x; occupancies of both sodium positions in the latter model also were refined in order to take into account the strong decrease of the scattering density in the sodium sites (Figure 27, **A**, **B**). It was found that the occupancies of A1 and A2 positions equal to 0.27(2) and 0.01(2) at the end point of the second anodic branch and grow throughout the following cathodic branch to 0.55(2) and 0.50(2) in almost linear fashion (R^2=0.94). From *operando* PXRD data obtained using the laboratory diffractometer in spite of their worse quality two-phase behavior of Na_2FePO_4F in the sodium-ion half-cell with formation of the intermediate phase $Na_{1.5\pm\delta}FePO_4F$ was confirmed by an automatic sequential Rietveld refinement, $Na_{1.5\pm\delta}FePO_4F$ being approximated by the model of $Na_{1.55}FePO_4F$ (Figure 27, **C**, **D**).
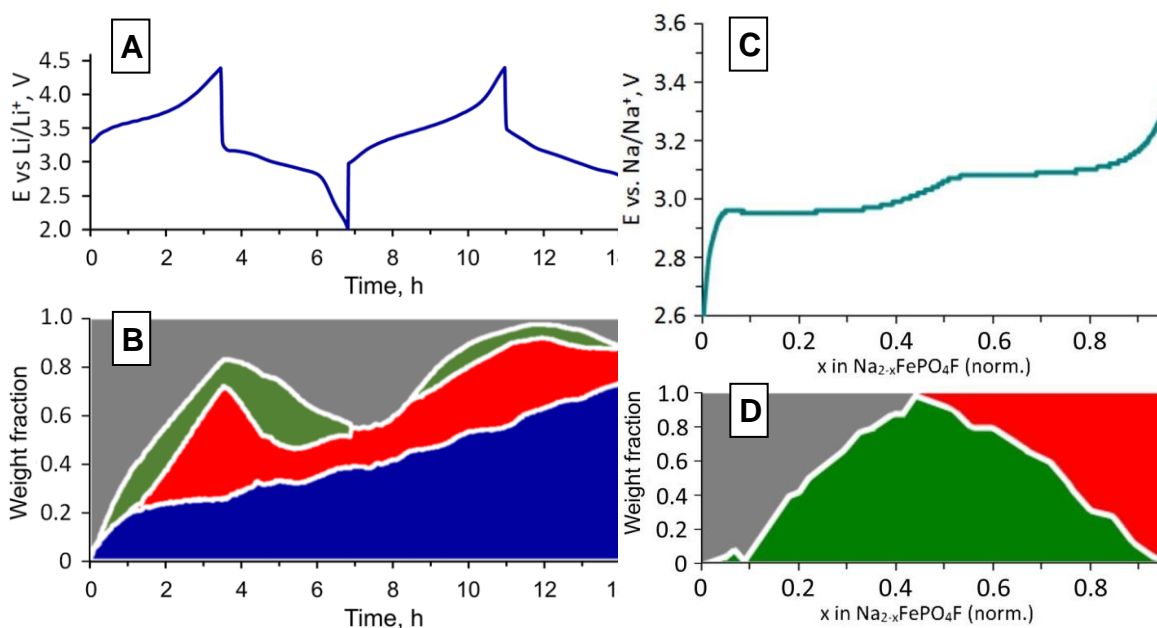
Figure 27. (**A**, **C**) Galvanostatic charge-discharge curves in lithium-ion half-cell (**A**, current density 24 mA/g) and sodium-ion half-cell (**C**, current density 12 mA/g); (**B**, **D**) corresponding percent stacked area charts demonstrating evolution of the phase composition from *operando* powder X-ray diffraction data acquired in lithium-ion (**B**, SXPD data) and sodium-ion (**D**, PXRD data) half-cells; **grey** color is for Na_2FePO_4F, **green** – for $Na_{1.55}FePO_4F$, **red** – for $NaFePO_4F$ and **blue** is for the series of solid solutions $(Na,Li)_{2-x}FePO_4F$. Reprinted with permission from "The Role of Semilabile Oxygen Atoms for Intercalation Chemistry of the Metal-Ion Battery Polyanion Cathodes" // I. V. Tereshchenko et al., J. Am. Chem. Soc. 140 (11), p. 3994–4003 (2018). Copyright 2018 American Chemical Society. Available from https://pubs.acs.org/articlesonrequest/AOR-YJh64uPKIstIQxXrxm5f.

For the explanation of behavior of $(Na,Li)_{2-x}FePO_4F$ demonstrated in Figure 26 (**B**) a description of structural and compositional transformations is necessary. But the *operando* data do not allow for a good enough description of a structure with lithium

partially substituting sodium. However, *ex situ* SXPD data can provide necessary information if the actual state of charge of the material is known. Thus, a necessity to obtain the $(Na,Li)_{2-x}FePO_4F$ samples with lithium instead of significant amount of sodium and precisely defined state of charge emerged.

Since the difference between 2nd and 3rd charge curves in the lithium-ion cell is very slight (Figure 26, **B**), it seems that ionic exchange of sodium for lithium is practically complete already at the beginning of the second cathodic branch. Besides, from EDX data it follows that the active phase of an electrode contains mere 0.2 ± 0.1 sodium atoms per formula unit after the first charge at current density of C/10 (which takes about 8 hours), which is seven times lower than the analogous phase contains if the electrode has been kept for 10 hours in a lithium-ion electrolyte without electrochemical oxidation (Table S13). Application of anodic current strongly accelerates the ion exchange making it almost complete in 1.5 cycles at current density C/10. That's why the $(Na,Li)_{1.5\pm\delta}FePO_4F$ and $(Na,Li)FePO_4F$ samples have been obtained in a lithium-ion half-cell by the same procedure as $Na_{1.55}FePO_4F$ and $NaFePO_4F$ had been obtained in a sodium-ion one, with the upper voltage limit of the "fully charged state" in lithium-ion half-cell of 4.2 V vs. Li/Li^+ instead of 3.8 V vs. Na/Na^+ in the sodium-ion half-cell. The deviation from the $Fe^{2+}:Fe^{3+}$ molar ratio in $(Na,Li)_{1.5\pm\delta}FePO_4F$ expected from the passed charge does not exceed 2%, as the M Mössbauer spectrum evidences (Figure S6). Refinement of both $(Na,Li)_{1.5\pm\delta}FePO_4F$ and $(Na,Li)FePO_4F$ structures from *ex situ* SXPD using space group *Pbcn* and taking into account the actual SOCs yielded the refined compositions $Li_{0.88}Na_{0.73}FePO_4F$ (Figure S9, Table S14 and Table S16) and $Li_{0.72}Na_{0.28}FePO_4F$ (Figure

S10, Table S15 and Table S17). In the former structure the Rietveld refinement revealed scattering densities in the A1 and A2 positions to be equal to ≈6.7 electrons and ≈3.3 electrons, respectively, which in total accounts for slightly more than a half of the scattering density expected for the same SOC in absence of ion exchange. Average bond lengths in the coordination spheres of the A1 and A2 positions were found to be 2.6 Å and 2.2 Å, respectively, which forced lithium to enter only into the A2 position. Thus, the residual scattering density in the A2 position was attributed to sodium. The total A2 occupancy appears to be very close to unity, which additionally speaks in favor of cation extraction from the A1 position only. In the $Li_{0.72}Na_{0.28}FePO_4F$ structure the A2 site appears to be empty as in $NaFePO_4F$ and the A1 site having scattering density of ≈5.2 electrons is occupied by lithium and sodium in the 72:28 ratio. The average bond length in the anion coordination sphere of A1 is 2.4 Å (CN=9) which is intermediate between the distances typical for the lithium and sodium coordination environment.

Partial depletion of A1 in $Li_{0.88}Na_{0.73}FePO_4F$ simultaneously with its full occupancy in $Li_{0.72}Na_{0.28}FePO_4F$ requires additional verification with DFT calculation. In absence of lithium, there is one specific oxygen atom out of four non-equivalent oxygen atoms, which is responsible for keeping the remaining sodium atom in the position A1 – namely the one lacking a redox-active metal in its environment and usually labeled in this structure as O2 (Figure 28, **A**). The key difference between the A1 and A2 positions is that the former is surrounded by three O2 atoms compared to only one O2 in the A2 environment (Figure 28, **B**, **C**). From the conjecture tested below by DFT calculations, occupation of the vacant A2 site by lithium shortens the A2-O2 distance from 2.2Å ($Na_{1.55}FePO_4F$, Table S11) to 1.9Å

($Li_{0.88}Na_{0.73}FePO_4F$, Table S16) and lithium becomes bound to A2 stronger than sodium is bound to any of both sodium sites.
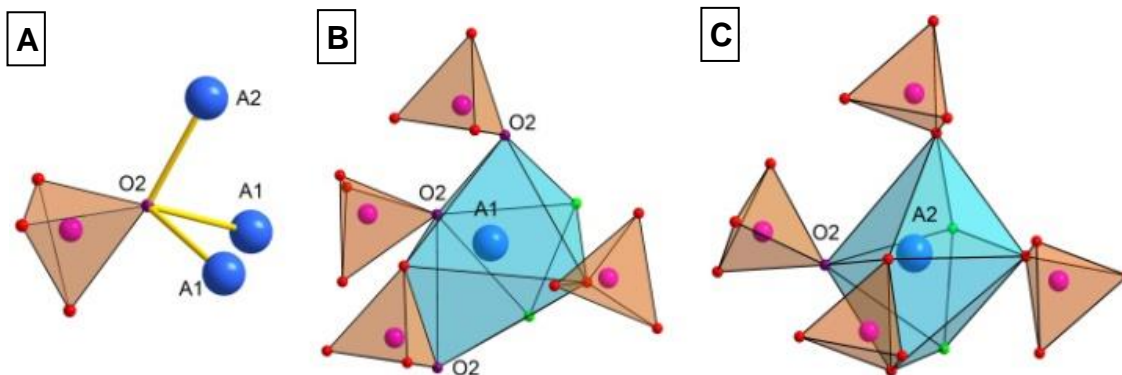
Figure 28. Coordination environment of O2 (**A**), A1 (**B**) and A2 (**C**) positions in Na_2FePO_4F. Reprinted with permission from "The Role of Semilabile Oxygen Atoms for Intercalation Chemistry of the Metal-Ion Battery Polyanion Cathodes" // I. V. Tereshchenko et al., J. Am. Chem. Soc. 140 (11), p. 3994–4003 (2018). Copyright 2018 American Chemical Society. Available from https://pubs.acs.org/articlesonrequest/AOR-YJh64uPKIstIQxXrxm5f.

Deintercalation potential of the sodium atom was selected as the criterion for estimation of ability of this atom to be extracted and was calculated as follows:

$$E = -\frac{H(A_xFePO_4F) - H(A_yFePO_4F) - (x-y)H(A)}{(x-y)\cdot e},$$

where $H(A_xFePO_4F)$ and $H(A_yFePO_4F)$ – total energies of the phase before and after deintercalation, $H(A)$ – analogous energy per one alkaline atom when it is in its own metallic crystal lattice, and e – charge of one electron. Among calculation results represented in Table 10 it is worth noticing at first, that the redox potential and unit cell volume change have been estimated correctly for $Na_{2-x}FePO_4F$ in a pure sodium system

(1st-4th rows of the table). Second, whatever position lithium occupies in the structure, it is harder to re-extract it than to extract sodium occupying another position (5th-10th strings). Total replacement of sodium for lithium separately in A1 and A2 sites has been found to have noticeable negative enthalpies of -0.08 and -0.15 eV, respectively [219]. These facts together partially explain the growing deintercalation potential of (Na, Li)$_{2-x}$FePO$_4$F observed in Figure 26 (**A**, **B**).

Table 10. Average deintercalation potential and relative volume change (%) for some reactions [A1][A2]FePO$_4$F→[A3][A4]FePO$_4$F. Adapted with permission from "The Role of Semilabile Oxygen Atoms for Intercalation Chemistry of the Metal-Ion Battery Polyanion Cathodes" // I. V. Tereshchenko et al., J. Am. Chem. Soc. 140 (11), p. 3994–4003 (2018). Copyright 2018 American Chemical Society. Available from https://pubs.acs.org/articlesonrequest/AOR-YJh64uPKIstIQxXrxm5f.

Transformation of [A1][A2] in [A1][A2]FePO$_4$F	Calculated		Experimental	
	E, V	ΔV,%	E, V	ΔV,%
[Na][Na]→[Na$_{0.5}$][Na]	3.08	0.7	2.95	−1.6
[Na][Na]→[Na][Na$_{0.5}$]	2.99	−1.6		
[Na][Na]→[□][Na]	3.24	5.4	3.05	−2.9
[Na][Na]→[Na][□]	3.03	−3.7		
[Na][Li]→[Na$_{0.5}$][Li]	2.98	0.8	3.10÷ 4.20	−
[Na][Li]→[Na][Li$_{0.5}$]	3.12	1.2		
[Li][Na]→[□][Na]	3.33	12.7		
[Li][Na]→[Li][□]	3.17	−6.2		
[Na][Li]→[□][Li]	3.15	8.3		
[Na][Li]→[Na][□]	3.18	2.5		

Finally, the refined $Li_{0.88}Na_{0.73}FePO_4F$ structure (Figure 29, **A,** right sketch) became a basis for the theoretical model entitled for calculation of formation energies by the cluster expansion method [220]; this model has been constructed as a compositional series $Na_{1-x}LiFePO_4F$ with lithium fully occupying the A2 site. In order to check the method at first on a simpler related system it was applied to a well understood and evidently similar series $Na_{2-x}FePO_4F$ with the A1 position fully occupied with sodium. This series was found to have several configurations at $x=0.5\pm\delta$ with noticeably lower formation energy than ones at $x=0$ and $x=1$, and a stable phase at $x=0.5$ (Figure 29, **B**, left). This was related to an ordered distribution of iron (II) and (III) and empty A2 sites being in full accordance with results of the structure investigation. Then, the same treatment of $Na_{1-x}LiFePO_4F$ series revealed almost four times lower formation energies for intermediate SOCs than ones found for $Na_{2-x}FePO_4F$ in the same SOCs (Figure 29, **B,** right). In the case of A1 site becoming available for a lithium atom, or A2 site – for a vacancy, the number of possible configurations will grow enormously, and most probably the formation energies of the most favorable configurations also will become much lower than –0.10 eV. These noticeably low formation energies of certain configurations of $(Na,Li)_{2-x}FePO_4F$ explain both spreading the compositional range of solid-solution-like behavior practically on the whole x range and the strong dependence of the deintercalation potential on x observed in Figure 26 (**A**, **B**).
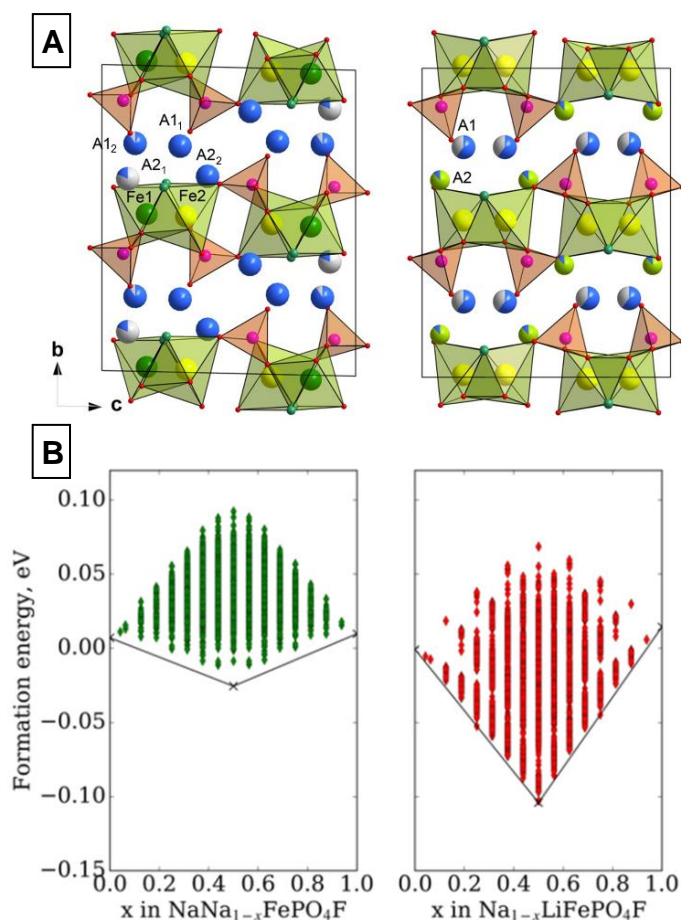
Figure 29. (**A**) Sketches of the unit cell of $Na_{1.55}FePO_4F$ (left) and $Li_{0.88}Na_{0.73}FePO_4F$ (right): iron is marked by **yellow** (Fe^{+2}) and **dark-green** (Fe^{+3}) spheres, sodium and lithium – **blue** and **small light-green** spheres; (**B**) formation energies (eV) calculated using the cluster expansion method for $NaNa_{1-x}FePO_4$ (left) and $Na_{1-x}LiFePO_4F$ (right) for all configurations of the 144-atom supercell; crosses mark stable phases at x = 0, 0.5, and 1. Reprinted with permission from "The Role of Semilabile Oxygen Atoms for Intercalation Chemistry of the Metal-Ion Battery Polyanion Cathodes" // I. V. Tereshchenko et al., J. Am. Chem. Soc. 140 (11), p. 3994–4003 (2018). Copyright 2018 American Chemical Society. Available from https://pubs.acs.org/articlesonrequest/AOR-YJh64uPKIstIQxXrxm5f.

3.4. Na$_2$CoPO$_4$F

PXRD analysis confirmed the purity of Na$_2$CoPO$_4$F/C with the unit cell parameters a=5.2416(7) Å, b=13.779(2) Å, c=11.688(2) Å and V= 844.2(2) Å^3 (Figure S3, Table S8) which are consistent with the literature [196]. Micrograph of the sample (inset from Figure S3) demonstrates uniform plates with ≈300 nm in size and ≈100 nm thickness. EDX analysis of the sample revealed the ratio of Na:Co:P=2.00:0.89:0.96 (standard deviation 5 %; see a representative spectrum in Figure S4). Galvanostatic measurements performed at 12.5 mA/g current density revealed almost 90 mAh/g of the reversible capacity with appr. 75% Coulombic efficiency at the first cycle (Figure 30, **A**, **B**). Materials obtained in previous works ([130],[221]) demonstrated significantly lower values of the Coulombic efficiency (typically 50%). We believe that the type of electrolyte used in our work and smaller size of the particles obtained in solvothermal synthesis lead to better kinetic parameters of the electrodes and, correspondingly, better relation between charge and discharge capacity. However, cycling stability of the electrodes is still a challenge necessitating further development of the stable high-voltage electrolyte. Since differential capacity curve of the Na$_2$CoPO$_4$F electrode strongly resembles this of Na$_2$FePO$_4$F (Figure 30, **C**), we supposed a similar two-phase mechanism of cycling with an intermediate charge-ordered phase. To confirm the mechanism the first galvanostatic cycle has been done at the approximate constant current density C/5 with *operando* SXPD measurements.
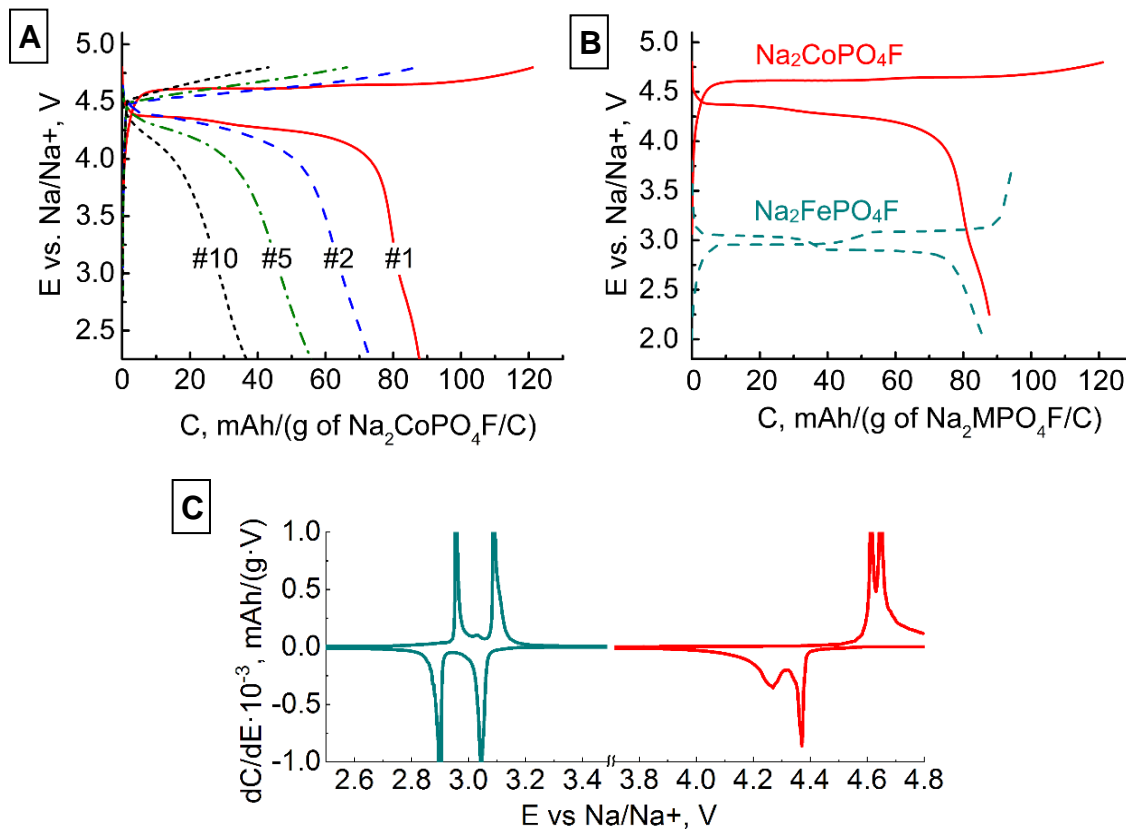
Figure 30. (**A**) first ten galvanostatic cycles of Na₂CoPO₄F/C and (**B**, **C**) comparison of its first cycle with the same of Na₂FePO₄F/C in a sodium-ion half-cell at the rate C/10.

It has been proven above that the charge ordering in the iron-bearing analogue of Na₂CoPO₄F at the state of charge (SOC) close to 0.5 results in monoclinic distortion changing the space group *Pbcn* to monoclinic subgroup *P*2₁/*b*11. *Operando* SXPD patterns acquired for Na₂CoPO₄F at the SOC close to 0.5 feature a weak peak seen at d-spacing of 11.4 Å which is absent at SOCs 0 and 1 indicating this distortion (Figure 31, **A**). Further, these patterns feature well pronounced peaks at d = 5.7 Å and 2.5 Å which become weaker but still are visible at SOC=0.25 and SOC=0.75 (Figure 31, **B**, **C**). At SOC=0.25 they coexist with the nearest strong reflections 002 and 104 of Na₂CoPO₄F, and at SOC=0.75 they coexist with some strong peaks of the charged phase corresponding to d-spacings of

5.6 Å and 2.46 Å. Since the positions of the above-mentioned peaks vary just very slightly throughout the charge and discharge, an intermediate ordered phase $Na_{1.5+\delta}CoPO_4F$ at SOC=0.5 is expected. Thus, if the phase transformations in Na_2CoPO_4F are similar to those in Na_2FePO_4F, then the mentioned peaks of $Na_{1.5+\delta}CoPO_4F$ and $NaCoPO_4F$ have the same Miller indices 002 and 104 as the mentioned peaks of Na_2CoPO_4F.
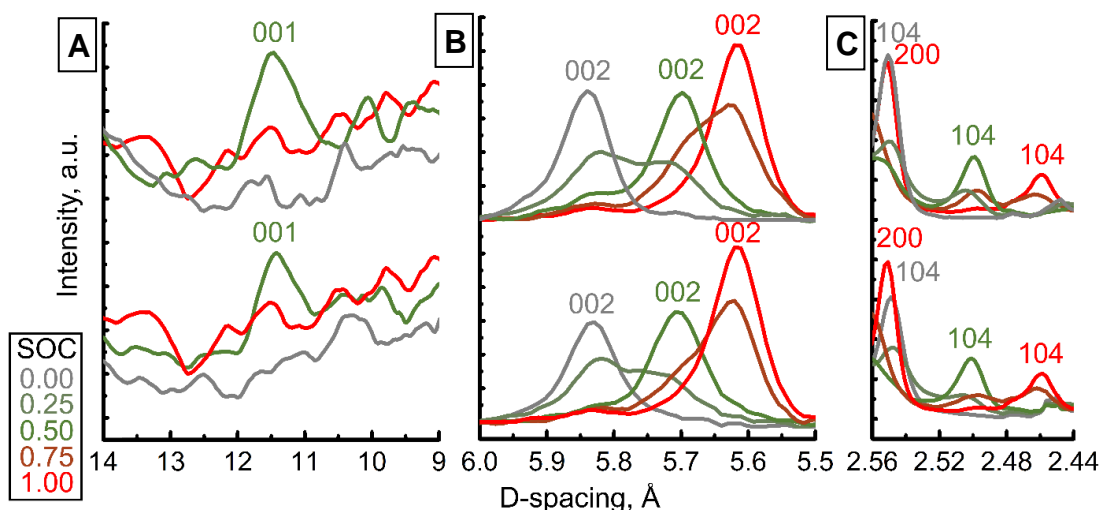
Figure 31. Selected regions of *operando* SXPD patterns of Na_2CoPO_4F acquired during charge (upper halves) and discharge (lower halves) and corresponding to SOC 0, 0.25, 0.5, 0.75 and 1; intensity maxima are supplied with assigned Miller indices.

The Rietveld refinement of the pattern obtained at ≈40% SOC confirmed that the main phase (84.7 wt.%) has a distinct $P2_1/b11$ monoclinic structure with the Rietveld-refined composition $Na_{1.44(1)}CoPO_4F$ and cell parameters a=5.2017(5) Å, b=13.850(3) Å, c=11.408(3) Å, α=90.89(3)° and V=821.8(3) Å^3 (Figure S11, Table S18). The structure of $Na_{1.44(1)}CoPO_4F$ is found to have the sodium vacancy in the same position $A2_1$ as $Na_{1.55}FePO_4F$. Clear difference in average interatomic distances of the 1st coordination spheres of two cobalt cations was observed ($<d_{Co1}>$=2.15(1) Å, $<d_{Co2}>$=1.96(1) Å); thus,

no major differences between the structures of $Na_{1.44}CoPO_4F$ and $Na_{1.55}FePO_4F$ was found. The structure model of $Na_{1.44}CoPO_4F$ in turn was used for taking into account the impurity of monoclinic $Na_{1.5-\delta}CoPO_4F$ at the charged state (4.8 V vs. Na/Na^+) and this SXPD pattern allowed to refine a second distinct structure with mass fraction 86.3%, *Pbcn* space group, zero occupancy of A2 site, significantly increased oxidation state of cobalt and unit cell parameters a=5.1021(5) Å, b=14.026(4) Å, c=11.232(4) Å and V=803.8(4) Å (Figure S12, Table S19).

The lattice constants predicted by GGA+U method for Na_2X, $Na_{1.5}X$ and NaX (X=$CoPO_4F$) are 5.28/13.85/11.75 Å, 5.25/13.97/11.49 Å, and 5.15/14.15/11.34 Å, respectively. The relative discrepancies between experimental and calculated values of Δa, Δb and Δc do not exceed 40% for $Na_2X/Na_{1.5}X$ transition and 20% for $Na_{1.5}X/NaX$ transition. The calculated average deintercalation potential for Na_2X/Na_1X is 4.06 V, the volume change is ~4 %. The average potentials for two deintercalation steps $Na_2X/Na_{1.5}X$ and $Na_{1.5}X/NaX$ are 4.02 V and 4.09 V, respectively. The increase of U value up to 5.8 eV allows to obtain average potential of 4.3 V (Na_2X/Na_1X), which is in better agreement with experiment. The step in potential is fairly small, therefore the formation of $Na_{1.5}CoPO_4F$ can be suppressed due to kinetic reasons, explaining why the corresponding potential step was almost absent in the work of Kubota et al. [130].

In order to confirm that there were little or no compositional ranges with solid-solution-like behavior, all *operando* SXPD patterns with 2θ=2÷42° (see subrange 2θ=5÷27° in Figure S13, **A**) were consequently used for the Rietveld refinement with fixed sodium occupancies but refined cell parameters in all three phases (Na_2X, $Na_{1.5}X$ and

NaX). The resulting evolution of the potential, phase composition and unit cell parameters is represented in Figure 32. The quality of refinements is comparable to that for the above-mentioned refinements for $ACoPO_4F$ (A=Na_2, $Na_{1.44}$ and Na) and can be deduced from the overall difference picture (Figure S13, **B**).
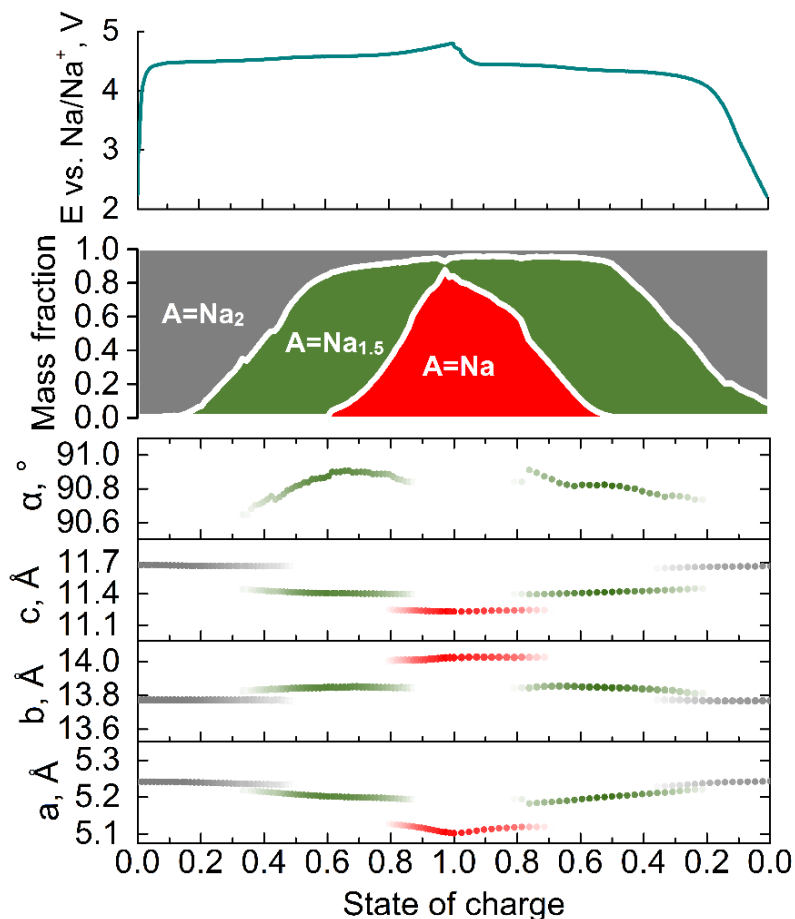
Figure 32. Overall evolution of electrochemical cell potential (vs. Na/Na$^+$), mass fractions and unit cell parameters for $ACoPO_4F$ (A=Na_2, $Na_{1.5}$ and Na) calculated from *operando* SXPD measurements; grey color is for A=Na_2, green is for A=$Na_{1.5}$ and red is for A=Na.

In Figure 32 one can find a tendency for the parameters *a* and *c* to decrease upon deintercalation slightly while for *b* an opposite trend is clear. It seems that the described transformations are reversible in the conditions of this experiment, and the overall picture strongly resembles that of the iron-bearing analogue. The sketch for the overall structural transformation is shown in Figure 33.
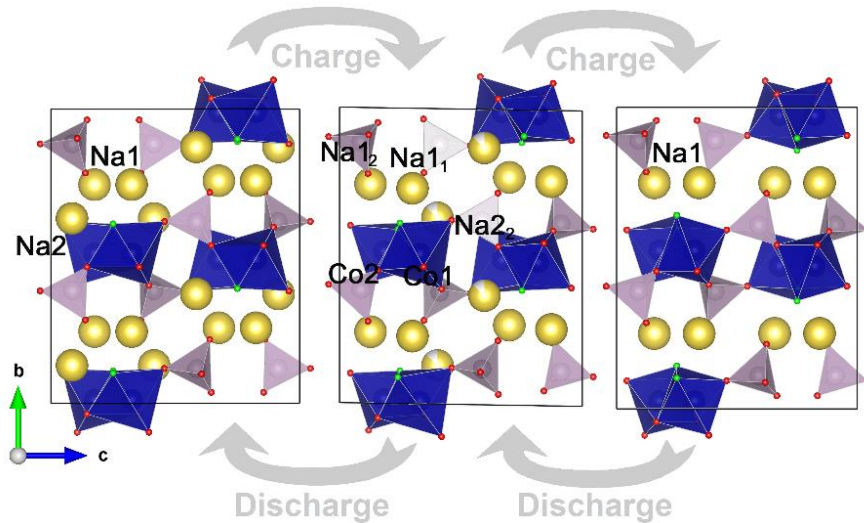
Figure 33. Sketch with crystal structure changes under charge and discharge; yellow spheres mark sodium atoms, blue octahedra – CoO_4F_2 polyhedra, small red and green spheres mark O and F atoms, respectively.

The formation of phases calculated with effective Hamiltonian obtained with cluster expansion method for $NaNa_{1-x}CoPO_4F$ system is shown in Figure 34. In this case we stick with a conservative U value of 3.4 eV, which ensures stable convergence of wave functions and does not overlocalize electrons as can happen in the case of larger U value [222]. Both DFT+U and effective Hamiltonians predict that $Na_{1.5}CoPO_4F$ is the only intermediate stable phase lying on convex hull. The stabilization of this phase is due to the charge-ordering and electrostatic interaction between Co^{3+} and Na vacancies. The

calculation of electrostatic energy using Ewald summation and formal oxidation states shows that the obtained configuration of Co charges for the given Na configuration possesses lower energy than those of the disordered configurations of Co charges.
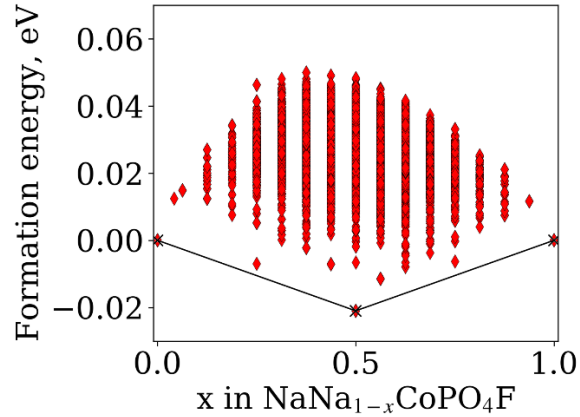
Figure 34. (**A**) Formation energies calculated using the cluster expansion method

(DFT+U).

To confirm the oxidation states we calculated local partial density of states (PDOS), which are shown in Figure 35 for Na_2CoPO_4F, $Na_{1.5}CoPO_4F$, and Na_1CoPO_4F. The Na_2CoPO_4F has only one Co position, which has two overlapping spin down e_g empty orbitals and one empty t_{2g} spin down orbital. Just below the Fermi level a localized filled t_{2g} orbital is seen. In $Na_{1.5}CoPO_4F$ initial Co position is split into two symmetry non-equivalent Co positions. The first position is oxidized to Co^{3+}, which results in 4 empty spin down orbitals and the second position stays in Co^{2+} state. The previously overlapped e_g empty orbitals of the second position are separated, though. Finally, in $NaCoPO_4F$ there is only one Co position with all Co in Co^{4+} state and no localized states below Fermi level.

The total volume shrinkage upon deintercalation amounts to less than 5% that is comparable to the volume change found in other phosphate cathodes (4.8% in

113

Na$_3$MnTi(PO$_4$)$_3$ [125], 6.6% in Na$_4$MnV(PO$_4$)$_3$ [164], ≈4% in Na$_4$Fe$_3$(PO$_4$)$_2$P$_2$O$_7$ [223], 3% in Na$_3$V$_2$(PO$_4$)$_2$F$_3$ [159]) and non-oxide cathodes (8% in Na$_2$FeMn(CN)$_6$·2H$_2$O [173], 6.9% in triplite-type NaFeSO$_4$F [224]). This and the possibility for further compositional modifications (substitution of Co with Mn, Mg for tuning the cyclic stability and redox potential) together make Na$_2$CoPO$_4$F a promising framework to make a cathode material for Na-ion batteries.
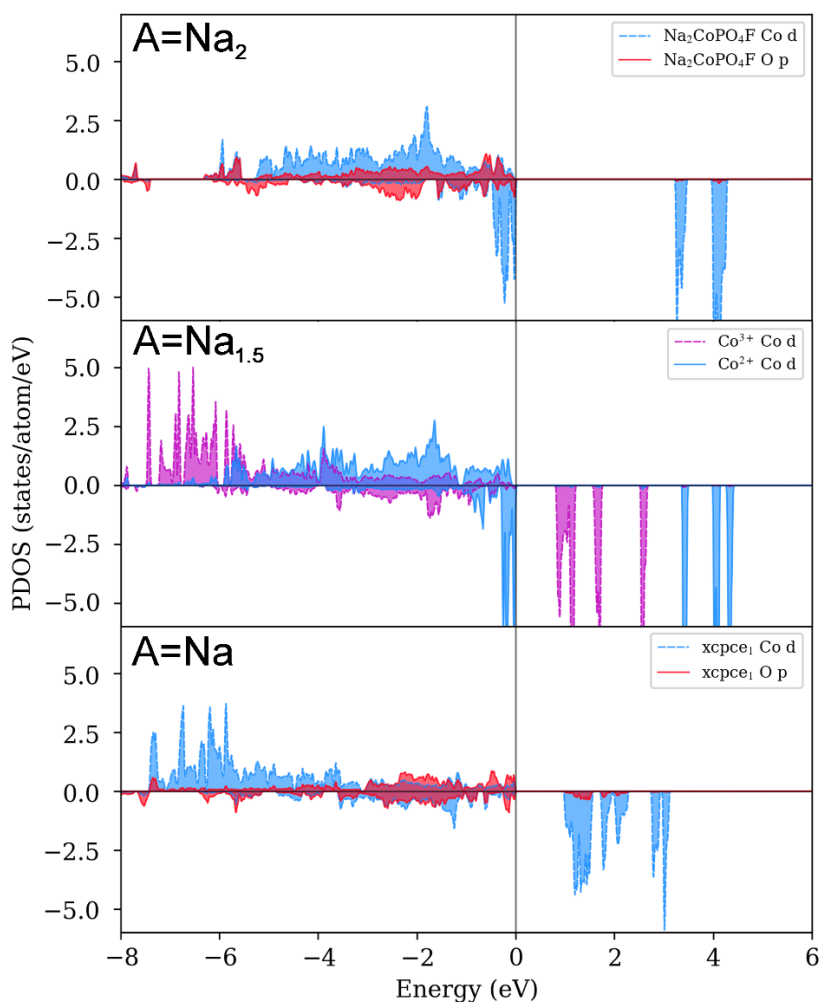
Figure 35. Partial local density of states for ACoPO$_4$F (A=Na$_2$, Na$_{1.5}$, Na). For A=Na$_2$ and Na PDOS on d Co and p O are shown and for A=Na$_{1.5}$ PDOS for Co1 and Co2 are shown.

114

3.5. $K_6(VO)_2(V_2O_3)_2(PO_4)_4(P_2O_7)$

The results of this chapter are described in "Reversible electrochemical potassium deintercalation from >4 V positive electrode material $K_6(VO)_2(V_2O_3)_2(PO_4)_4(P_2O_7)$" // I. V. Tereshchenko, D. A. Aksyonov, A. Zhugayevych, E. V. Antipov and A. M. Abakumov; Solid State Ionics 357, p. 115468. Copyright 2020, with permission from Elsevier. Available from https://www.sciencedirect.com/science/article/abs/pii/S0167273820305221.

The PXRD analysis of the phase composition identified the main phase as $K_6(VO)_2(V_2O_3)_2(PO_4)_4(P_2O_7)$ (#01-075-4707) along with impurities of $K_2VOP_2O_7$ (#01-084-0011) and β-$K_2(VO)_3(P_2O_7)_2$ (#01-080-1208). The SEM micrograph (Figure 36, **A**) demonstrates strongly inhomogeneous size of the crystallites ranging between 0.1 and 5 microns. The EDX spectra (Figure 36, **B**) show the K:V:P ratio of 1.00:1.01(6):1.04(8).
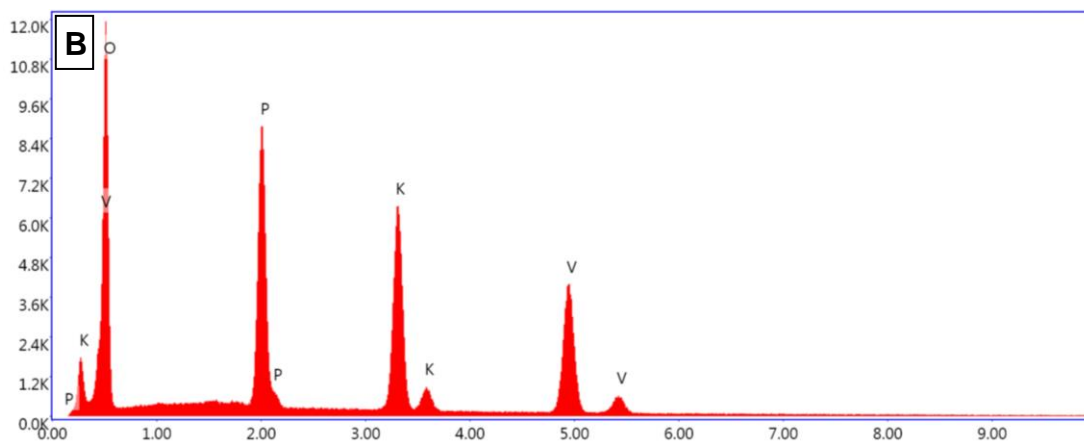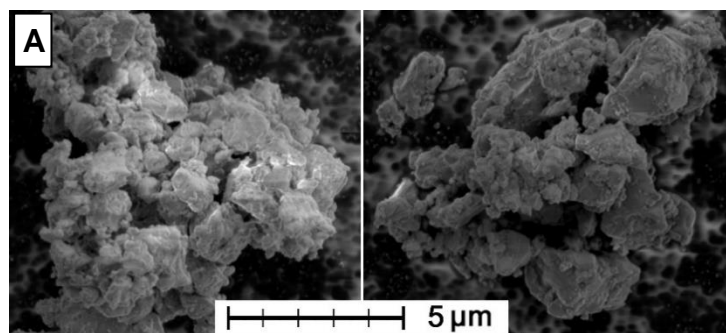
Figure 36. The FE-SEM micrographs (**A**) and typical EDX spectrum (**B**) of $K_6(VO)_2(V_2O_3)_2(PO_4)_4(P_2O_7)$.

Here is need for a short remark on the crystal structure of the $K_6(VO)_2(V_2O_3)_2(PO_4)_4(P_2O_7)$. It can be described by two different structure models, one of which corresponds to the actual structure and another one is simplified and has four times smaller unit cell than the former one [202]. The simplified structure (Figure 23, **B**) has *Pnma* space group and orthorhombic unit cell [202]; the unit cell parameters calculated from single crystal data a=6.980 Å, b=13.389 Å, c=14.235 Å [202]. Its framework can be described as consisting of infinite single chains composed of corner-sharing $V2O_6$ octahedra and coupled chains of $V1_2O_9$ dimers linked by pyrophosphate P_2O_7 groups; both single and coupled chains run along the *a* axis and are linked with each other with

phosphate PO_4 tetrahedra into the three-dimensional framework. The framework contains spacious tunnels aligned along the *b* axis and populated with the K cations. If the simplified structure has space group *Pnma* then the location of the pyrophosphate groups must be disordered: two possible energetically equivalent configurations of the P_2O_7 groups are transformed into each other by the *n*-glide plane and should stochastically occur in the structure in equal amounts. Structure solution from the single crystal diffraction data revealed an ordering of the P_2O_7 groups within a supercell which has triclinic symmetry and is four times as large as the *Pnma* cell [202]. This supercell also features charge ordering of vanadium: one half of V^{4+} cations and all V^{5+} cations are placed into the V2O6 octahedra and V1O5 tetragonal pyramids, respectively; another half of V^{4+} cations also occupies V_1O_5 pyramids along with V^{5+}, forming the superstructure; the arrangement of coupled octahedra see in [202].

As the ordered structure model of $K_6(VO)_2(V_2O_3)_2(PO_4)_4(P_2O_7)$ is prohibitively large for the Rietveld refinement from conventional PXRD data, much simpler disordered *Pnma* model was adopted. Because of large number of variables, all atomic positions were refined with common atomic displacement parameter (ADP). The occupancy factors for potassium crystallographic positions were refined revealing the values of 0.990(2) and 0.974(3) for the K1 and K2 positions, respectively, that is very close to the full occupancy, in agreement with the cationic composition measured by EDX. The $K_2VOP_2O_7$ and β-$K_2(VO)_3(P_2O_7)_2$ admixtures were also included into the refinement resulting in their mass fractions of 8.9(1) and 1.63(6) wt.%, respectively. The experimental, calculated and difference PXRD profiles after the Rietveld refinement are shown in Figure S14, main

crystallographic parameters are provided in Table 11, the atomic coordinates are listed in Table S20. Similar refinement strategy was also applied to the crystal structures of the materials at different state of charge (Figure S16-Figure S18, Table S21-Table S23).

Table 11. The main crystallographic parameters from the Rietveld refinement of $K_{6x}(VO)_2(V_2O_3)_2(PO_4)_4(P_2O_7)$ in different states of charge.

		Initial	Charged to 4.5 V	Cycled and discharged
Space group		*Pnma*		
a, Å		6.9891(1)	7.1120(4)	6.9817(2)
b, Å		13.3735(2)	13.0850(5)	13.3826(5)
c, Å		14.2495(2)	14.1822(5)	14.2480(5)
V, Å^3		1331.89(6)	1319.8(1)	1331.3(1)
Occupancy	K1	0.990(2)	0.595(5)	0.989(3)
	K2	0.974(3)	0.551(5)	1.061(5)
Average V-O distance, Å	V1	2.002(4)	1.968(7)	2.034(5)
	V2	1.936(6)	1.909(10)	1.919(7)
x in $K_{6\cdot x}(VO)_2(V_2O_3)_2(PO_4)_4(P_2O_7)$	PXRD	0.985(2)	0.580(5)	1.013(4)
	EDX	0.97(8)	0.68(4)	1.48(25)
Number of reflections		569	388	540
Number of parameters		38	37	37
R_p		0.063	0.011	0.017
R_{wp}		0.084	0.016	0.026
R_F		0.027	0.018	0.029
Goodness of fit		1.55	1.9	0.1

The galvanostatic cycling of the first ten charge-discharge cycles with the rate of C/50 (1C = 88 mA/g) and the upper potential limit of 4.4 V vs. K/K$^+$ (except the first charge having the limit of 4.5 V) is demonstrated in Figure 37, **A**. It should be noted that as both $K_2VOP_2O_7$ and β-$K_2(VO)_3(P_2O_7)_2$ admixtures in the sample are electrochemically inert, the observed electrochemical activity is attributed solely to the $K_6(VO)_2(V_2O_3)_2(PO_4)_4(P_2O_7)$ phase. The first charge occurs through two sloping plateaus centered at ~4.1 and 4.4V. Only the first plateau remains on discharge revealing a reversible

capacity of 48 mAh/g. The high-voltage plateau is attributed to electrolyte decomposition and it was the reason for lowering the upper voltage limit from 4.5 to 4.4 V vs. K/K^+ in the subsequent cycles. The remarkable shifts of peaks on differential capacity curves evidence that there is growth of overall material resistance which can be attributed to the accumulation of the products of electrolyte oxidation on the surface of active particles (Figure 37, **B**). Cycling at a higher temperature 60°C and decreased voltage cutoff 4.4 V vs. K/K+ allows to get the same discharge capacity at a higher rate C/20, as the one obtained at room temperature and slow rate of C/50, but unfortunately, the coulombic efficiency drop is disproportionately high if the temperature is increased (Figure S15).
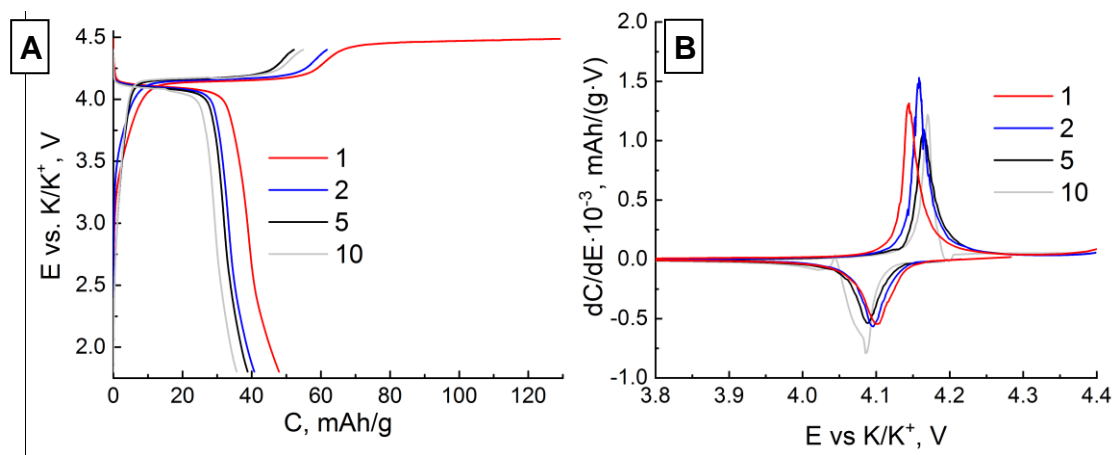
Figure 37. (**A**) Galvanostatic charge-discharge curves of $K_6(VO)_2(V_2O_3)_2(PO_4)_4(P_2O_7)$ in a potassium-ion half-cell with current density C/50 at 25°C; (**B**) dC/dE plots obtained from the GSCD curves.

Ascribing the first plateau with the ~60 mAh/g of the charge capacity to the K-ion deinsertion from the $K_6(VO)_2(V_2O_3)_2(PO_4)_4(P_2O_7)$ structure is corroborated by the Rietveld-refined occupancy factors for the K1 and K2 positions in the material charged to 4.5V (Table 11). It indicates the extraction of nearly 42% of potassium up to the

$K_{3.5}(VO)_2(V_2O_3)_2(PO_4)_4(P_2O_7)$ composition (Table S21) that corresponds to 55 mAh/g capacity, in good agreement with the experimentally measured value. There is no drastic preference of the K1 and K2 positions for the K-ion deinsertion, although the K2 position delivers slightly more potassium than the K1 one. It should be noted that charging to 4.4V allows extracting slightly less potassium (up to $K_{3.87}(VO)_2(V_2O_3)_2(PO_4)_4(P_2O_7)$ composition) corresponding to 47 mAh/g of reversible capacity (Table S22). Upon discharge, the K2 position restores its full occupancy, but about 1% of vacancies remains in the K1 position (Table S23). This corroborates the conjecture that >4.5V plateau is due to electrolyte decomposition. The average V-O distances shrink upon full charge for both V1 and V2 positions by 1.7% and 1.4%, respectively, indicating oxidation of the V cations. The concomitant volume change is, however, smaller and amounts to 0.9% only. Thus $K_6(VO)_2(V_2O_3)_2(PO_4)_4(P_2O_7)$ can virtually be considered as a "low strain" cathode, even in spite of relatively large size of deintercalated K^+ ions. Low Coulombic efficiency remaining for first 10 cycles could most probably be attributed to a reaction of cathode with the products of reduction of electrolyte with the potassium metal (so-called "chemical dialogue" [7]).

In order to get more insight into the charge-discharge mechanism, one galvanostatic cycle was conducted simultaneously with acquisition of *operando* PXRD patterns within d-spacings range between 3.2 and 2.6 Å (Figure 38). The reflections demonstrate continuous displacement which is symmetrical upon charge and discharge that is an indicator of solid-solution like behavior upon cycling. Only in the middle of charge very

slight intensity blur around the d-spacing 2.9Å can be noticed, but it can be an evidence of slowed reaction of the bulkiest particles.
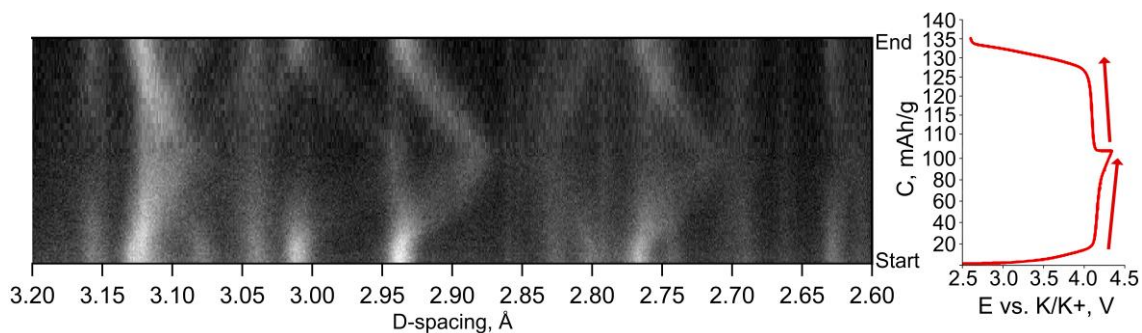
Figure 38. PXRD patterns sequence of the D-spacings range between 3.2 and 2.6 Å made *operando* with current density 2.2 mAh/g (contour plot, **left**), and the corresponding cell voltage (**right**); the lower and upper halves of the picture correspond to the charge and discharge half-cycles; since the half-cycles required different amount of time, the halves of the picture have been made to have the same height artificially; the background has been manually subtracted and the residual intensity has been normalized so that the absolute maxima and minima correspond to white and black colors.

For DFT calculations the simplified structure model with the *Pnma* space group (Figure 23, **B**) used for the Rietveld refinement is inappropriate because it contains fractional occupancies due to stochastic arrangement of the pyrophosphate groups. However, ordered variants of the $K_6(VO)_2(V_2O_3)_2(PO_4)_4(P_2O_7)$ structure can be derived from the disordered *Pnma* model by appropriate symmetry reduction. Appropriate isotropy subgroups with the (0,0,0) **k**-vector (i.e. maintaining the same unit cell volume) have been found with the ISOTROPY software [225]. Two irreducible representations Γ_2^- and Γ_4^+ provide two ordered structures with $Pnm2_1$ and $P12_1/m1$ space groups, respectively. These

hypothetical ordered structures were used for DFT analysis. It should be noted that the supercell published in [202] consists of fragments which locally can be described either by $Pnm2_1$ or by $P2_1/m$ space group and are arranged chequer-wise in ab projection (Figure 39, **A**) overlapping by their halves.

To justify our approach, we compared atomic coordinates in the $Pnm2_1$ and $P2_1/m$ models with those in the supercell after atomic relaxation with the DFT+U method. The obtained root mean square of atomic positions between the models and supercell in both cases is less than 0.04 Å. Since on the course of K migration the displacement of oxygen anions can exceed 0.4 Å, the small difference in atomic positions of 0.04 Å will have only negligible impact on the values of K^+ migration barriers.

The optimized lattice constants for both $Pnm2_1$ and $P2_1/m$ unit cells were found to be very close to each other and equal to 7.06, 13.63 and 14.56 Å, respectively that is about 2% larger than the experimental values in Table 11. Such overestimation by the generalized gradient approximation functional is a known issue for the phosphate materials [226]. Both considered ordered models contain four non-equivalent K positions resulting in six unique shortest K-K migration hops (Figure 39, **B**, **C**). The migration distances and barriers for both ordered models are collected in Table 12. We found that they have comparable migration barriers, the p4 barrier being lower in the $P2_1/m$ model and p6 barrier being lower in the $Pnm2_1$ model. The hops p1, p2, p4, and p6 have migration barriers roughly 0.3-0.4 eV, while p3 and p5 hops have barriers about 0.8 eV.
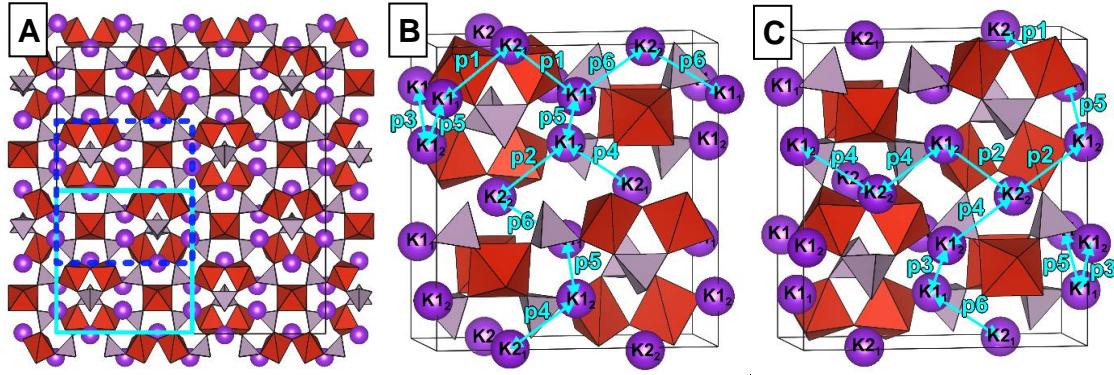
Figure 39. (**A**) Projection *ab* of the supercell described in [202] with distinguished fragments corresponding to the unit cells of the *Pnm*2$_1$ (dashed blue contour) and *P*2$_1$/*m* (solid cyan contour) ordered models; (b, c) zoomed unit cells with space group *Pnm*2$_1$ (**B**) and *P*2$_1$/*m* (**C**) along with combinations of diffusion paths p$_i$ along crystallographic axes *a*, *b* and *c* (see numeric data in Table 12). Both cells are represented in *bc* projection and additional potassium atoms are shown for better visibility of the diffusion paths.

Table 12. Length of migration hop, interatomic distance in the ideal crystal structure (Å) and the corresponding migration barriers calculated with NEB method (eV) for both crystal structures (*Pnm*2$_1$ and *P*2$_1$/*m*); n$_s$ is the number of K atom sitting at the end of the hop in the list of K atoms closest to the K sitting at the beginning of the hop.

Hop designation	Hop trajectory, n$_s$		d, Å		ΔE, eV	
	*Pnm*2$_1$	*P*2$_1$/*m*	*Pnm*2$_1$	*P*2$_1$/*m*	*Pnm*2$_1$	*P*2$_1$/*m*
p1	K1$_1$ – K2$_1$, 1	K1$_1$ – K2$_1$, 1	4.09	4.11	0.27	0.24
p2	K1$_2$ – K2$_2$, 1	K1$_2$ – K2$_2$, 1	4.21	4.19	0.32	0.31
p3	K1$_1$ – K1$_2$, 2	K1$_1$ – K1$_2$, 2	4.28	4.30	0.80	0.83
p4	K1$_2$ – K2$_1$, 3	K1$_2$ – K2$_2$, 3	4.38	4.34	0.38	0.28
p5	K1$_2$ – K1$_1$, 4	K1$_2$ – K1$_1$, 4	4.41	4.39	0.82	0.84
p6	K1$_1$ – K2$_2$, 4	K1$_1$ – K2$_1$, 4	4.47	4.51	0.27	0.42

The continuous transport of K^+ ions involves combination of several hops. All possible combinations required for migration along main crystallographic axes are provided in Table 13. Taking into account alternative migration routes and two variants of the structures, the resulting limiting barriers for K-ion transport along a, b, and c axes are 0.84, 0.31 and 0.84 eV, respectively. We conclude that the diffusivity has mainly one-dimensional nature, since barriers along a and c of 0.84 eV are dramatically higher than the barrier 0.31 eV along b; besides, 0.84 eV is a relatively high value in general [226]. At the same time, the obtained barrier of 0.31 eV for migration along b is comparable to that observed in $LiFePO_4$ [226], being only by 0.1 eV higher than in recently discovered high-rate $KVPO_4F$ cathode material [227].

Table 13. Pathways for continuous transport along main crystallographic axes and their effective migration barriers (eV) for the $Pnm2_1$ and $P2_1/m$ models and for the structure representing a mixture of both models.

Direction of diffusion	Combination of hops	ΔE_p, eV		
		$Pnm2_1$	$P2_1/m$	Mixture
along a	p3 – p5	0.82	0.84	0.84
along b	p6 – p1 – p1 – p6	0.27	0.42	0.31
	p4 – p2 – p2 – p4	0.38	0.31	
along c	p1 – p5 – p2 – p6 – p5 – p4	0.82	--	0.84
	p1 – p5 – p4 – p1 – p5 – p4			
	p6 – p3 – p4 – p1 – p3 – p2	0.80		
	p6 – p3 – p2 – p6 – p3 – p2			
	p1 – p5 – p2 – p4 – p3 – p6	--	0.84	

Overall, the mobility of K in the $K_6(VO)_2(V_2O_3)_2(PO_4)_4(P_2O_7)$ material should be fast, but because of essentially 1D character its practical realization requires dedicated shape of the crystallites with shortest dimension along the easiest diffusion direction b. Yet we

considered two additional long migration hops along the a and c axes, but the required barriers for migration in these cases are larger than 1.5 eV. However, under extraction of K these barriers could be noticeably reduced. The dependence of migration barriers on the potassium concentration requires further studies.

From Figure 40 (**A**) showing the topology of migration paths in the $Pnm2_1$ structure it is seen that the paths are almost straight with slight wriggling; the largest shuffling of P and O atoms is observed for the p3 and p5 hops with highest barriers of 0.8 eV. At saddle point the K cation crosses either triangle (p1, p4, p6) or tetragon (p2, p3, p5) formed by oxygen anions, which approximately lie in one plane. The corresponding average K-O distances at the saddle point are 2.70, 2.73, 2.6, 2.58, 2.67, and 2.64 Å for the p1-p6 hops, respectively. It is hard to withdraw any relation between these distances and migration barriers; as in the case of hop lengths (Table 12), the values underlie importance of the environment rather than of just interatomic distances. The only trend to observe here is that the saddle points sitting in "triangle" windows propose systematically lower hop barriers than ones sitting in "tetragons", excepting the "tetragonal" point with the longest average K-O distance 2.73 Å which proposes a barrier comparable to these of "triangle" windows (Figure 40, **B**). Also, one can see that potassium has energy higher by roughly 0.1 eV in $K1_2$ and $K2_1$ positions than in $K1_1$ and $K2_2$ positions (notations from Figure 39, **B**). For all hops the saddle point is located near the middle of the path.
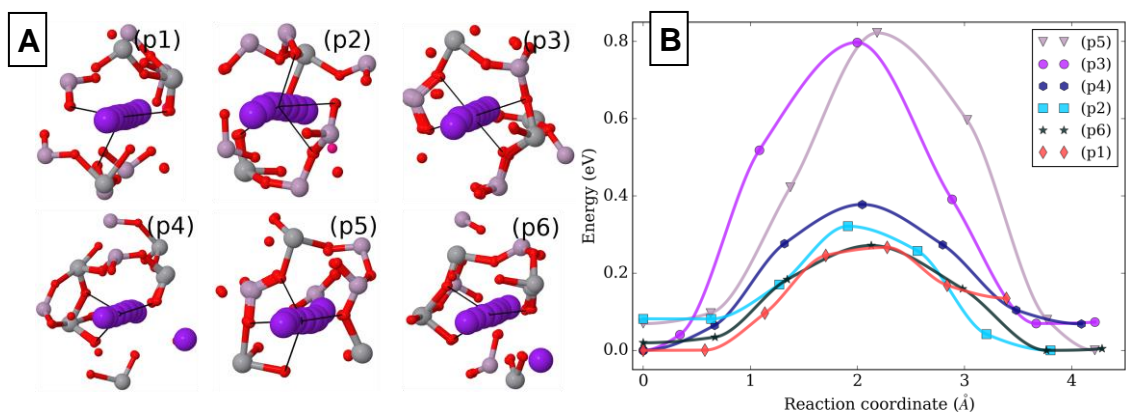
Figure 40. (**A**) Overlapped atomic positions from every image obtained from optimization with NEB method in structure with space group *Pnm*2_1 (only representative nearest neighbor atoms from each image are shown); the black lines connect the middle atom of the hop reaction pathway with the nearest neighbor oxygen atoms forming a slightly distorted plane perpendicular to the local trajectory; (**B**) corresponding energy profiles for the investigated K-K migration hops.

In order to understand the origin of higher migration barriers in the case of the p3 and p5 hops we used local descriptors, which were introduced in the recent paper [226], where it was shown that the migration barriers can be rationalized in terms of site repulsive/attractive and lattice energies. The first descriptor is the change of the average K-O distance between the saddle and minimum energy positions (Δd_{av}) on the course of K migration. The calculated values of Δd_{av} averaged by six nearest-neighbor oxygen atoms are provided in Table S24. It is seen that larger Δd_{av} values correspond to larger DFT barriers. Since the average K-O distance is smaller in the saddle point we suggest that the site repulsive energy has considerable contribution into the migration barrier. To check this conjecture we calculated migration barriers using only site repulsive energies (ΔE_{Born})

obtained from the Gilbert parametrization with parameters based on vibrational and crystallographic data [228]. The ΔE_{Born} are provided in Table S24 from which it follows that ΔE_{Born} shows good correlation with ΔE. Much larger repulsive energy barriers in the case of the p3 and p5 hops highlight that in these cases the migration channel is simply too narrow for K migration. Interestingly, in case of p1 and p6, the same DFT migration barriers correspond to different ΔE_{Born} values. As was shown in [226], this may be related either to different site attractive or to lattice energy contributions.

4. Concluding remarks

A practically phase-pure lithium cobalt borate $LiCoBO_3$ has been obtained by a solvo-hydrothermal method for the first time. Unfortunately, the particle morphology in the calcined sample was not qualitatively different from that reported in Ref. [114] and [195], and only a negligible and strongly fading reversible capacity has been obtained. Yet, a useful possibility can be seen in a compositional modification of $LiCoBO_3$, namely a partial substitution of cobalt for magnesium in order to get a more stable cathode engaging the Co^{2+}/Co^{3+} redox transition. A big work conducted in the direction of the solvo-hydrothermal synthesis of the layered Na_2MPO_4F (M = Mn, Fe, Co) also favors investigation of isostructural compounds with more complex compositions and the general formula $Na_2Mn_{1-x-y-z}Co_xNi_yMg_zPO_4F$; here a disordering of manganese and sodium atoms seems to be the only potential obstacle for the reversible electrochemical activity.

The complex investigation of the phase transitions in Na_2FePO_4F revealed the influence of the "dangling" oxygen atom O2 (which mainly imparts additional flexibility to the structure during cycling) both on kinetics and thermodynamics of intercalation, which in turn defines the practical characteristics of the material. In a lithium-ion half-cell this happens to Na_2FePO_4F through ion exchange of sodium for lithium accelerated by electrochemical extraction; in the beginning it has place in the A2 position, and after reaching some atomic fraction of lithium in the A2 position the process shifts to the A1 position. Calculations by the cluster expansion method show heavy energy gain at x around 0.5 in the modelled compositional series $Na_{1-x}LiFePO_4F$ where the sodium atoms and vacancies sit always in A1 and all A2 sites are always occupied by lithium. This calculation

explains the strong dependence of deintercalation potential in layered $(Na,Li)_{2-x}FePO_4F$ on x, contrary to the flat two-step dependence in $Na_{2-x}FePO_4F$.

For the first time $Na_{2-x}CoPO_4F$ has been shown to have the behavior similar to its ferrous analogue, the latter being known for its high cyclability and relatively low redox potential of 3.1 V vs. Na/Na^+. The dependence of deintercalation potential is flat and has two steps corresponding to the two half-reactions $Na_2CoPO_4F \rightarrow Na_{1.5}CoPO_4F$ and $Na_{1.5}CoPO_4F \rightarrow NaCoPO_4F$. This was supposed from the strikingly similar two-step deformations of unit cells of Na_2CoPO_4F and Na_2FePO_4F, though the voltage difference in two steps is roughly 50% larger for Na_2FePO_4F (it may be caused by the difference in ligand field stabilization for Fe^{3+} and Co^{3+}). Still $Na_{2-x}CoPO_4F$ demonstrates the ability of cobalt to undergo redox reactions similar to the highly reversible ones of iron, the voltage of this transition being almost 50% higher than in Na_2FePO_4F. Two main obstacles for the real application of Na_2CoPO_4F are low stability of Na_2CoPO_4F during calcination in a reductive gas media (e.g. in the presence of carbonized glucose additive) and low coulombic efficiency of this cathode with the carbonate esters- and sulfone-based electrolytes (at least in the sodium metal half-cells).

$K_6(VO)_2(V_2O_3)_2(PO_4)_4(P_2O_7)$ has been characterized as a potassium-ion cathode for the first time. This compound is chemically similar to $KVOPO_4$, and the only irremovable difference is that its theoretical specific capacity is smaller than that of $KVOPO_4$. The synthesis of its samples with higher phase purity and/or in a better morphology than it was in the present work requires completely new approaches. The reason for that is the remarkable ability of potassium to coordinate water molecules serving

as a source of chemical inhomogeneity in the calcined gel, and the diversity of possible coordination spheres of vanadium allowing this inhomogeneity to consolidate itself in the form of miscellaneous crystalline impurities. In spite of these specific drawbacks the gel synthesis allowed to get samples of $K_6(VO)_2(V_2O_3)_2(PO_4)_4(P_2O_7)$ applicable for the initial electrochemical characterization, their reversible specific capacity having exceeded 50% of the theoretical value and the redox potential being 4.1 V vs. K/K^+. The relatively poor cyclability was attributed mainly to the "chemical dialogue" phenomenon rather than structure peculiarities because the morphology of material and applied research methods could not allow to establish what might be responsible for the capacity fade on the atomic level. Finally, due to the literature data (ref. [202]) resulting from a well-conducted structural analysis it was satisfactory for the DFT calculations to approximate the superstructure existing in $K_6(VO)_2(V_2O_3)_2(PO_4)_4(P_2O_7)$ as a superposition of two simplified structures, every of which appears to be a one dimensional potassium-ion conductor from the point of DFT. For both simplified structures the barrier of potassium diffusion hop has been found to be below 0.31 eV.

Majority of the useful results constituting the present work would be very hard or impossible to get without an accurate and comprehensive approach to the application of the modern research methods for metal-ion electrode materials; SXPD and PXRD applied *operando* were such methods in the present work. Due to the recently published construction of an electrochemical cell with monocrystal sapphire X-ray windows [205] the quality of the SXPD data was as high as possible; as the consequence, the rapidity of the data treatment and the reliability of the final structural data also were at their best.

5. Short conclusions

1. For the first time techniques of combined hydro-solvothermal synthesis for reproducible synthesis of practically phase-pure powders of $LiCoBO_3$ and Na_2CoPO_4F have been proposed. Synthesis and qualitative analysis of phase composition of $Na_2Co_{1-x}Mn_xPO_4F$ (x=0.2, 0.4, 0.6, 0.8) samples has been conducted;

2. Combining *operando* powder X-ray diffraction, γ-resonance spectroscopy with ^{57}Fe nuclei and density functional theory calculations the mechanism of cycling of $(Na,Li)_{2-x}FePO_4F$ has been described, and an explanation of the strong monotonic dependence of the deintercalation potential on x throughout the whole compositional range $0 \leq x \leq 1$ is proposed. A novel electrochemical cell with single crystal sapphire windows has been successfully applied to drastically lessen the contribution of X-ray windows into synchrotron X-ray powder diffraction patterns;

3. Mechanisms of cycling of Na_2FePO_4F and Na_2CoPO_4F in a sodium-ion half-cell have been clarified using synchrotron X-ray powder diffraction; structures of $Na_{1.55}FePO_4F$, $Na_{1.44}CoPO_4F$ and $NaCoPO_4F$ have been characterized;

4. Using powder X-ray diffraction, a reversible electrochemical deintercalation of potassium from polycrystalline $K_6(VO)_2(V_2O_3)_2(PO_4)_4(P_2O_7)$ has been demonstrated; the obtained material has demonstrated more than 50% of the theoretical capacity of 88 mAh/g with the volume change not exceeding 0.9%. Using DFT+U approach the potassium diffusion barriers were estimated for basic crystallographic directions of the $K_6(VO)_2(V_2O_3)_2(PO_4)_4(P_2O_7)$ structure and the barrier for the direction *b* has been found to be below 0.31 eV.

6. References

[1]   M. S. Whittingham // Lithium Batteries and Cathode Materials // Chem. Rev. 104 (10), p. 4271–4302 (2004);

[2]   J.-M. Tarascon and M. Armand // Issues and challenges facing rechargeable lithium batteries // Nature 414, p. 359 (2001);

[3]   M. M. Thackeray, C. Wolverton and E. D. Isaacs // Electrical energy storage for transportation—approaching the limits of and going beyond, lithium-ion batteries // Energy Environ. Sci. 5 (7), p. 7854–7863 (2012);

[4]   R. A. Huggins // *Advanced batteries. Materials science aspects, New York*. Springer Science+Business Media, 2009;

[5]   S. J. An, J. Li, C. Daniel, D. Mohanty, S. Nagpure and D. L. Wood // The state of understanding of the lithium-ion-battery graphite solid electrolyte interphase (SEI) and its relationship to formation cycling // Carbon N. Y. 105, p. 52–76 (2016);

[6]   J. B. Goodenough and K. Youngsik // Challenges for Rechargeable Li Batteries // Chem. Mater. 22, p. 587–603 (2010);

[7]   L. Ellis // Probing the Causes and Effects of Parasitic Reactions in Lithium-Ion Cells // Ph.D. thesis, Dalhousie University, 2018;

[8]   Y. Jiang, X. Yan, Z. Ma, P. Mei, W. Xiao, Q. You and Y. Zhang // Development of the PEO based solid polymer electrolytes for all-solid state lithium ion batteries // , Polymers, 10 (11), p. 1237 (2018);

[9]   K. Xu // Nonaqueous Liquid Electrolytes for Lithium-Based Rechargeable Batteries // Chem. Rev. 104 (10), p. 4303–4418 (2004);

[10] Z. Chen, W. Q. Lu, J. Liu and K. Amine // LiPF$_6$/LiBOB blend salt electrolyte for high-power lithium-ion batteries // Electrochim. Acta 51 (16), p. 3322–3326 (2006);

[11] Y. Zhu, Y. Li, M. Bettge and D. P. Abraham // Positive Electrode Passivation by LiDFOB Electrolyte Additive in High-Capacity Lithium-Ion Cells // J. Electrochem. Soc. 159 (12), p. A2109–A2117 (2012);

[12] S. Tan, Y. J. Ji, Z. R. Zhang and Y. Yang // Recent progress in research on high-voltage electrolytes for lithium-ion batteries // ChemPhysChem 15 (10), p. 1956–1969 (2014);

[13] X. Zeng, G.-L. Xu, Y. Li, X. Luo, F. Maglia, C. Bauer, S. F. Lux, O. Paschos, S.-J. Kim, P. Lamp, J. Lu, K. Amine and Z. Chen // Kinetic Study of Parasitic Reactions in Lithium-Ion Batteries: A Case Study on LiNi$_{0.6}$Mn$_{0.2}$Co$_{0.2}$O$_2$ // ACS Appl. Mater. Interfaces 8 (5), p. 3446–3451 (2016);

[14] S. E. Sloop, J. K. Pugh, S. Wang, J. B. Kerr and K. Kinoshita // Chemical Reactivity of PF$_5$ and LiPF$_6$ in Ethylene Carbonate/Dimethyl Carbonate Solutions // Electrochem. Solid-State Lett. 4 (4), p. A42–A44 (2001);

[15] S. Wilken, P. Johansson and P. Jacobsson // Additives in organic electrolytes for lithium batteries // Chapter 3 in *Lithium Batteries: Advanced Technologies and Applications*, p. 39–70 (2013);

[16] B. Markovsky, A. Nimberger, Y. Talyosef, A. Rodkin, A. M. Belostotskii, G. Salitra, D. Aurbach and H.-J. Kim // On the influence of additives in electrolyte solutions on the electrochemical behavior of carbon/LiCoO$_2$ cells at elevated temperatures // J. Power Sources 136 (2), p. 296–302 (2004);

[17] K. Xu, Y. Lam, S. S. Zhang, T. R. Jow and T. B. Curtis // Solvation Sheath of Li^+ in Nonaqueous Electrolytes and Its Implication of Graphite/Electrolyte Interface Chemistry // J. Phys. Chem. C 111 (20), p. 7411–7421 (2007);

[18] M. C. Smart, B. V. Ratnakumar, C. K. Huang and S. Surampudi // Performance Characteristics of Lithium Ion Cells for Low Temperature Applications // Conference paper in *Electrochemical Society Meeting*, 1998;

[19] CRC Handbook of Chemistry and Physics, 90th ed. (2009−2010);

[20] J. Y. Song, Y. Y. Wang and C. C. Wan // Conductivity Study of Porous Plasticized Polymer Electrolytes Based on Poly(vinylidene fluoride) A Comparison with Polypropylene Separators // J. Electrochem. Soc. 147 (9), p. 3219 (2000);

[21] M. Xu, S. Dalavi and B. L. Lucht // Electrolytes for lithium-ion batteries with high-voltage cathodes // Chapter 4 in *Lithium Batteries: Advanced Technologies and Applications*, p. 71–87 (2013);

[22] Y. Abu-Lebdeh and I. Davidson // High-Voltage Electrolytes Based on Adiponitrile for Li-Ion Batteries // J. Electrochem. Soc. 156 (1), p. A60–A65 (2009);

[23] Y. Abu-Lebdeh and I. Davidson // New electrolytes based on glutaronitrile for high energy/power Li-ion batteries // J. Power Sources 189 (1), p. 576–579 (2009);

[24] P. Isken, C. Dippel, R. Schmitz, R. W. Schmitz, M. Kunze, S. Passerini, M. Winter and A. Lex-Balducci // High flash point electrolyte for use in lithium-ion batteries // Electrochim. Acta 56 (22), p. 7530–7535 (2011);

[25] L. Xue, K. Ueno, S.-Y. Lee and C. A. Angell // Enhanced performance of sulfone-based electrolytes at lithium ion battery electrodes, including the $LiNi_{0.5}Mn_{1.5}O_4$

high voltage cathode // J. Power Sources 262, p. 123–128 (2014);

[26] A. Abouimrane, I. Belharouak and K. Amine // Sulfone-based electrolytes for high-voltage Li-ion batteries // Electrochem. commun. 11 (5), p. 1073–1076 (2009);

[27] K. Xu and C. A. Angell // Sulfone-Based Electrolytes for Lithium-Ion Batteries // J. Electrochem. Soc. 149 (7), p. A920 (2002);

[28] A. Guerfi, A. Vijh and K. Zaghib // Safe Lithiium Rechargeable Batteries Based on Ionic Liquids // Chapter 14 in *Lithium Batteries: Advanced Technologies and Applications*, p. 291–326 (2013);

[29] A. Manuel Stephan // Review on gel polymer electrolytes for lithium batteries // Eur. Polym. J. 42 (1), p. 21–42 (2006);

[30] S. Yong An, I. Chen Jeong, M.-S. Won, E. Jeong and Y.-B. Shim // Effect of additives in PEO/PAA/PMAA composite solid polymer electrolytes on the ionic conductivity and Li ion battery performance // J. Appl. Electrochem. 39, p. 1573–1578 (2009);

[31] T. Itoh, M. Yoshikawa, T. Uno and M. Kubo // Solid polymer electrolytes based on poly(lithium carboxylate) salts // Ionics (Kiel). 15, p. 27–33 (2009);

[32] J. W. Fergus // Ceramic and polymeric solid electrolytes for lithium-ion batteries // J. Power Sources 195 (15), p. 4554–4569 (2010);

[33] R. Miao, B. Liu, Z. Zhu, Y. Liu, J. Li, X. Wang and Q. Li // PVDF-HFP-based porous polymer electrolyte membranes for lithium-ion batteries // J. Power Sources 184 (2), p. 420–426 (2008);

[34] A. Manuel Stephan and K. S. Nahm // Review on composite polymer electrolytes

for lithium batteries // Polymer (Guildf). 47 (16), p. 5952–5964 (2006);

[35] A. M. M. Ali, R. H. Y. Subban, H. Bahron, M. Z. A. Yahya and A. S. Kamisan // Investigation on modified natural rubber gel polymer electrolytes for lithium polymer battery // J. Power Sources 244, p. 636–640 (2013);

[36] C. Fang, X. Wang and Y. S. Meng // Key Issues Hindering a Practical Lithium-Metal Anode // Trends Chem. 1 (2), p. 152–158 (2019);

[37] B. Simon, S. Flandrois, K. Guerin, A. Fevrier-Bouvier, I. Teulat and P. Biensan // On the choice of graphite for lithium ion batteries // J. Power Sources 81–82, p. 312–316 (1999);

[38] T. Ohzuku, A. Ueda and N. Yamamoto // Zero-Strain Insertion Material of Li [$Li_{1/3}Ti_{5/3}$] O_4 for Rechargeable Lithium Cells // J. Electrochem. Soc. 142 (5), p. 1431–1435 (1995);

[39] L. Aldon, P. Kubiak, M. Womes, J. C. Jumas, J. Olivier-Fourcade, J. L. Tirado, J. I. Corredor and C. Pérez Vicente // Chemical and Electrochemical Li-Insertion into the $Li_4Ti_5O_{12}$ Spinel // Chem. Mater. 16 (26), p. 5721–5725 (2004);

[40] I. Belharouak, Y.-K. Sun, W. Lu and K. Amine // On the Safety of the $Li_4Ti_5O_{12}/LiMn_2O_4$ Lithium-Ion Battery System // J. Electrochem. Soc. 154 (12), p. A1083 (2007);

[41] K. Zaghib, A. Mauger, H. Groult, J. B. Goodenough and C. Julien // Advanced Electrodes for High Power Li-ion Batteries // Materials (Basel). 6, p. 1028–1049 (2013);

[42] X. Su, Q. Wu, J. Li, X. Xiao, A. Lott, W. Lu, B. W. Sheldon and J. Wu // Silicon-

Based Nanomaterials for Lithium-Ion Batteries: A Review // Adv. Energy Mater. 4 (1), p. 1300882 (2014);

[43] Y. R. Lim, F. Shojaei, K. Park, C. S. Jung, J. Park, W. Il Cho and H. S. Kang // Arsenic for high-capacity lithium- and sodium-ion batteries // Nanoscale 10 (15), p. 7047–7057 (2018);

[44] M. He, K. Kravchyk, M. Walter and M. V Kovalenko // Monodisperse Antimony Nanocrystals for High-Rate Li-ion and Na-ion Battery Anodes: Nano versus Bulk // Nano Lett. 14 (3), p. 1255–1262 (2014);

[45] J. Chen // Recent Progress in Advanced Materials for Lithium Ion Batteries // Materials (Basel). 6 (1), p. 156–183 (2013);

[46] S. A. Webb, L. Baggetto, C. A. Bridges and G. M. Veith // The electrochemical reactions of pure indium with Li and Na: Anomalous electrolyte decomposition, benefits of FEC additive, phase transitions and electrode performance // J. Power Sources 248, p. 1105–1117 (2014);

[47] B. Scrosati // Lithium Batteries: from early stages to the future // Lithium Batter., p. 21–38 (2013);

[48] S. Goriparti, E. Miele, F. De Angelis, E. Di Fabrizio, R. Proietti Zaccaria and C. Capiglia // Review on recent progress of nanostructured anode materials for Li-ion batteries // J. Power Sources 257, p. 421–443 (2014);

[49] K. Nobuhara, H. Nakayama, M. Nose, S. Nakanishi and H. Iba // First-principles study of alkali metal-graphite intercalation compounds // J. Power Sources 243, p. 585–587 (2013);

[50] H. Kim, J. Hong, Y. U. Park, J. Kim, I. Hwang and K. Kang // Sodium storage behavior in natural graphite using ether-based electrolyte systems // Adv. Funct. Mater. 25 (4), p. 534–541 (2015);

[51] C.-J. Yu, S.-B. Ri, S.-H. Choe, G.-C. Ri, Y.-H. Kye and S.-C. Kim // Ab initio study of sodium cointercalation with diglyme molecule into graphite // Electrochim. Acta 253 (2017);

[52] B. Jache, J. O. Binder, T. Abe and P. Adelhelm // A comparative study on the impact of different glymes and their derivatives as electrolyte solvents for graphite co-intercalation electrodes in lithium-ion and sodium-ion batteries // Phys. Chem. Chem. Phys. 18 (21), p. 14299–14316 (2016);

[53] H. Kim, J. Hong, G. Yoon, H. Kim, K.-Y. Park, M.-S. Park, W.-S. Yoon and K. Kang // Sodium intercalation chemistry in graphite // Energy Environ. Sci. 8, p. 2963–2969 (2015);

[54] X. Wang, Y. Li, Y. Gao, Z. Wang and L. Chen // Additive-free sodium titanate nanotube array as advanced electrode for sodium ion batteries // Nano Energy 13 (4), p. 687–692 (2015);

[55] K. Kataoka and J. Akimoto // Synthesis and electrochemical sodium and lithium insertion properties of sodium titanium oxide with the tunnel type structure // J. Power Sources 305, p. 151–155 (2016);

[56] P. J. P. Naeyaert, M. Avdeev, N. Sharma, H. Ben Yahia and C. D. Ling // Synthetic, Structural and Electrochemical Study of Monoclinic $Na_4Ti_5O_{12}$ as a Sodium-Ion Battery Anode Material // Chem. Mater. 26 (24), p. 7067–7072 (2014);

[57] Y. Ge, H. Jiang, J. Zhu, Y. Lu, C. Chen, Y. Hu, Y. Qiu and X. Zhang // High cyclability of carbon-coated TiO_2 nanoparticles as anode for sodium-ion batteries // Electrochim. Acta 157, p. 142–148 (2015);

[58] C. Xu, Y. Xu, C. Tang, Q. Wei, J. Meng, L. Huang, L. Zhou, G. Zhang, L. He and L. Mai // Carbon-coated hierarchical $NaTi_2(PO_4)_3$ mesoporous microflowers with superior sodium storage performance // Nano Energy 28, p. 224–231 (2016);

[59] Z. Jian, Z. Xing, C. Bommier, Z. Li and X. Ji // Hard Carbon Microspheres: Potassium-Ion Anode Versus Sodium-Ion Anode // Adv. Energy Mater. 6 (3), p. 1501874 (2015);

[60] Y. An, H. Fei, Z. Zhang, L. Ci, S. Xiong and J. Feng // A titanium-based metal–organic framework as an ultralong cycle-life anode for PIBs // Chem. Commun. 125 (Cmc) (2017);

[61] M. S. Whittingham and F. R. Gamble // The lithium intercalates of the transition metal dichalcogenides // Mater. Res. Bull. 10 (5), p. 363–371 (1975);

[62] E. J. Frazer and S. Phang // Titanium disulphide as a cathode material in lithium batteries — a review // J. Power Sources 6 (4), p. 307–317 (1981);

[63] K. Mizushima, P. C. Jones, P. J. Wiseman and J. B. Goodenough // Li_xCoO_2 (0<x<-1): A new cathode material for batteries of high energy density // Mater. Res. Bull. 15 (6), p. 783–789 (1980);

[64] B. Xu, D. Qian, Z. Wang and Y. S. Meng // Recent progress in cathode materials research for advanced lithium ion batteries // Mater. Sci. Eng. R Reports 73 (5–6), p. 51–65 (2012);

[65]   G. G. Amatucci, J. M. Tarascon and L. C. Klein // CoO_2, The End Member of the Li_xCoO_2 Solid Solution // J. Electrochem. Soc. 143 (3), p. 1114 (1996);

[66]   S. T. Myung, N. Kumagai, S. Komaba and H. T. Chung // Effects of Al doping on the microstructure of $LiCoO_2$ cathode materials // Solid State Ionics 139 (1–2), p. 47–56 (2001);

[67]   T. Ohzuku and Y. Makimura // Layered Lithium Insertion Material of $LiCo_{1/3}Ni_{1/3}Mn_{1/3}O_2$ for Lithium-Ion Batteries // Chem. Lett. 30 (7), p. 642–643 (2001);

[68]   E. Rossen, C. D. W. Jones and J. R. Dahn // Structure and electrochemistry of $Li_xMn_yNi_{1-y}O_2$ // Solid State Ionics 57 (3), p. 311–318 (1992);

[69]   D. K. Kim, P. Muralidharan, H.-W. Lee, R. Ruffo, Y. Yang, C. K. Chan, H. Peng, R. A. Huggins and Y. Cui // Spinel $LiMn_2O_4$ Nanorods as Lithium Ion Battery Cathodes // Nano Lett. 8 (11), p. 3948–3952 (2008);

[70]   J. M. Tarascon, D. Guyomard and G. L. Baker // An update of the Li metal-free rechargeable battery based on $Li_{1+\chi}Mn_2O_4$ cathodes and carbon anodes // J. Power Sources 44 (1), p. 689–700 (1993);

[71]   A. K. Padhi, K. S. Nanjundaswamy and J. B. Goodenough // Phospho-olivines as Positive-Electrode Materials for Rechargeable Lithium Batteries // J. Electrochem. Soc. 144 (4), p. 1188–1194 (1997);

[72]   J. Jiang and J. R. Dahn // ARC studies of the thermal stability of three different cathode materials: $LiCoO_2$; $Li[Ni_{0.1}Co_{0.8}Mn_{0.1}]O_2$; and $LiFePO_4$, in $LiPF_6$ and LiBoB EC/DEC electrolytes // Electrochem. commun. 6 (1), p. 39–43 (2004);

[73] T. Drezen, N.-H. Kwon, P. Bowen, I. Teerlinck, M. Isono and I. Exnar // Effect of particle size on LiMnPO$_4$ cathodes // J. Power Sources 174 (2), p. 949–953 (2007);

[74] T. N. L. Doan and I. Taniguchi // Preparation of LiCoPO$_4$/C nanocomposite cathode of lithium batteries with high rate performance // J. Power Sources 196 (13), p. 5679–5684 (2011);

[75] S. Adams // Lithium ion pathways in LiFePO$_4$ and related olivines // J. Solid State Electrochem. 14, p. 1787–1792 (2010);

[76] W.-J. Zhang // Structure and performance of LiFePO$_4$ cathode materials: A review // J. Power Sources 196 (6), p. 2962–2970 (2011);

[77] F. Omenya, N. A. Chernova, R. Zhang, J. Fang, Y. Huang, F. Cohen, N. Dobrzynski, S. Senanayake, W. Xu and M. S. Whittingham // Why substitution enhances the reactivity of LiFePO$_4$ // Chem. Mater. 25 (1), p. 85–89 (2013);

[78] S.-Y. Chung, J. T. Bloking and Y.-M. Chiang // Electronically conductive phosphor-olivines as lithium storage electrodes // Nat. Mater.(1), p. 123–128 (2002);

[79] A. V Churikov, A. V Ivanishchev, I. A. Ivanishcheva, V. O. Sycheva, N. R. Khasanova and E. V Antipov // Determination of lithium diffusion coefficient in LiFePO$_4$ electrode by galvanostatic and potentiostatic intermittent titration techniques // Electrochim. Acta 55 (8), p. 2939–2950 (2010);

[80] H.-K. Song, K. T. Lee, M. G. Kim, L. F. Nazar and J. Cho // Recent Progress in Nanostructured Cathode Materials for Lithium Secondary Batteries // Adv. Funct. Mater. 20 (22), p. 3818–3834 (2010);

[81] H. Huang, S.-C. Yin and L. F. Nazar // Approaching Theoretical Capacity of

LiFePO$_4$ at Room Temperature at High Rates // Electrochem. Solid-State Lett. 4 (10), p. A170–A172 (2001);

[82] D. Wang, H. Buqa, M. Crouzet, G. Deghenghi, T. Drezen, I. Exnar, N.-H. Kwon, J. H. Miners, L. Poletto and M. Grätzel // High-performance, nano-structured LiMnPO$_4$ synthesized via a polyol method // J. Power Sources 189 (1), p. 624–628 (2009);

[83] Y.-T. Cui, N. Xu, L.-Q. Kou, M.-T. Wu and L. Chen // Enhanced electrochemical performance of different morphological C/LiMnPO$_4$ nanoparticles from hollow-sphere Li$_3$PO$_4$ precursor via a delicate polyol-assisted hydrothermal method // J. Power Sources 249, p. 42–47 (2014);

[84] J.-N. Zhu, W.-C. Li, F. Cheng and A.-H. Lu // Synthesis of LiMnPO$_4$/C with superior performance as Li-ion battery cathodes by a two-stage microwave solvothermal process // J. Mater. Chem. A 3 (26), p. 13920–13925 (2015);

[85] X.-L. Pan, C.-Y. Xu, D. Hong, H.-T. Fang and L. Zhen // Hydrothermal synthesis of well-dispersed LiMnPO$_4$ plates for lithium ion batteries cathode // Electrochim. Acta 87 (0), p. 303–308 (2013);

[86] Z. Qin, X. Zhou, Y. Xia, C. Tang and Z. Liu // Morphology controlled synthesis and modification of high-performance LiMnPO$_4$ cathode materials for Li-ion batteries // J. Mater. Chem. 22 (39), p. 21144 (2012);

[87] D. Zhang, X. Yu, Y. Wang, R. Cai, Z. Shao, X.-Z. Liao and Z.-F. Ma // Ballmilling-Assisted Synthesis and Electrochemical Performance of LiFePO$_4$ / C for Lithium-Ion Battery Adopting Citric Acid as Carbon Precursor // J. Electrochem. Soc. 156

(10), p. A802 (2009);

[88] B. Pei, H. Yao, W. Zhang and Z. Yang // Hydrothermal synthesis of morphology-controlled $LiFePO_4$ cathode material for lithium-ion batteries // J. Power Sources 220, p. 317–323 (2012);

[89] C. Xu, L. Li, F. Qiu, C. An, Y. Xu, Y. Wang, Y. Wang, L. Jiao and H. Yuan // Graphene oxide assisted facile hydrothermal synthesis of $LiMn_{0.6}Fe_{0.4}PO_4$ nanoparticles as cathode material for lithium ion battery // J. Energy Chem. 23 (3), p. 397–402 (2014);

[90] C. A. J. Fisher, N. Kuganathan and M. S. Islam // Defect chemistry and lithium-ion migration in polymorphs of the cathode material Li_2MnSiO_4 // J. Mater. Chem. A 1 (13), p. 4207–4214 (2013);

[91] R. Dominko, M. Bele, M. Gaberšček, A. Meden, M. Remškar and J. Jamnik // Structure and electrochemical performance of Li_2MnSiO_4 and Li_2FeSiO_4 as potential Li-battery cathode materials // Electrochem. commun. 8 (2), p. 217–222 (2006);

[92] V. V Politaev, A. A. Petrenko, V. B. Nalbandyan, B. S. Medvedev and E. S. Shvetsova // Crystal structure, phase relations and electrochemical properties of monoclinic Li_2MnSiO_4 // J. Solid State Chem. 180 (3), p. 1045–1050 (2007);

[93] S. Nishimura, S. Hayase, R. Kanno, M. Yashima, N. Nakayama and A. Yamada // Structure of Li_2FeSiO_4 // J. Am. Chem. Soc. Commun. 130 (40), p. 13212–13213 (2008);

[94] A. R. Armstrong, N. Kuganathan, M. S. Islam and P. G. Bruce // Structure and

Lithium Transport Pathways in Li_2FeSiO_4 Cathodes for Lithium Batteries // J. Am. Chem. Soc. 133 (33), p. 13031–13035 (2011);

[95] R. J. Gummow, N. Sharma, V. K. Peterson and Y. He // Crystal chemistry of the *Pmnb* polymorph of Li_2MnSiO_4 // J. Solid State Chem. 188, p. 32–37 (2012);

[96] H. Duncan, A. Kondamreddy, P. H. J. Mercier, Y. Le Page, Y. Abu-Lebdeh, M. Couillard, P. S. Whitfield and I. J. Davidson // Novel *Pn* Polymorph for Li_2MnSiO_4 and Its Electrochemical Activity As a Cathode Material in Li-Ion Batteries // Chem. Mater. 23 (24), p. 5446–5456 (2011);

[97] J. Yang, X. Kang, D. He, T. Peng, L. Hu and S. Mu // Hierarchical shuttle-like Li_2FeSiO_4 as a highly efficient cathode material for lithium-ion batteries // J. Power Sources 242, p. 171–178 (2013);

[98] T. Masese, C. Tassel, Y. Orikasa, Y. Koyama, H. Arai, N. Hayashi, J. Kim, T. Mori, K. Yamamoto, Y. Kobayashi, H. Kageyama, Z. Ogumi and Y. Uchimoto // Crystal Structural Changes and Charge Compensation Mechanism during Two Lithium Extraction/Insertion between Li_2FeSiO_4 and $FeSiO_4$ // J. Phys. Chem. C 119 (19), p. 10206–10211 (2015);

[99] D. Sun, H. Wang, P. Ding, N. Zhou, X. Huang, S. Tan and Y. Tang // In-situ synthesis of carbon coated Li_2MnSiO_4 nanoparticles with high rate performance // J. Power Sources 242, p. 865–871 (2013);

[100] V. Legagneur, Y. An, A. Mosbah, R. Portal, A. Le Gal La Salle, A. Verbaere, D. Guyomard and Y. Piffard // $LiMBO_3$ (M=Mn, Fe, Co):: synthesis, crystal structure and lithium deinsertion/insertion properties // Solid State Ionics 139 (1), p. 37–46

(2001);

[101] A. Yamada, N. Iwane, Y. Harada, S. Nishimura, Y. Koyama, Y. Koyama and I. Tanaka // Lithium Iron Borates as High-Capacity Battery Electrodes // Adv. Mater. 22 (32), p. 3583–3587 (2010);

[102] D.-H. Seo, Y.-U. Park, S.-W. Kim, I. Park, R. A. Shakoor and K. Kang // First-principles study on lithium metal borate cathodes for lithium rechargeable batteries // Phys. Rev. B 83 (20), p. 205127 (2011);

[103] D. Morgan, A. Van der Ven and G. Ceder // Li Conductivity in Li_x MPO_4 (M = Mn , Fe , Co , Ni) Olivine Materials // Electrochem. Solid-State Lett. 7 (2), p. A30–A32 (2004);

[104] K. Kang and G. Ceder // Factors that affect Li mobility in layered lithium transition metal oxides // Phys. Rev. B 74 (9), p. 94105 (2006);

[105] X. Ma, B. Kang and G. Ceder // High Rate Micron-Sized Ordered $LiNi_{0.5}Mn_{1.5}O_4$ // J. Electrochem. Soc. 157 (8), p. A925–A931 (2010);

[106] Y. Z. Dong, Y. M. Zhao, Z. D. Shi, X. N. An, P. Fu and L. Chen // The structure and electrochemical performance of $LiFeBO_3$ as a novel Li-battery cathode material // Electrochim. Acta 53 (5), p. 2339–2345 (2008);

[107] A. Abouimrane, M. Armand and N. Ravet // Carbon Nano-Painting: Application to non-Phosphate Oxyanions, e.g. Borates // Thesis in *New trends in intercalation compounds for energy storage conversion*, ECS Proceedings, Vol. 20 (2003);

[108] J. C. Kim, C. J. Moore, B. Kang, G. Hautier, A. Jain and G. Ceder // Synthesis and Electrochemical Properties of Monoclinic $LiMnBO_3$ as a Li Intercalation Material

// J. Electrochem. Soc. 158 (3), p. A309–A315 (2011);

[109] V. Aravindan, K. Karthikeyan, S. Amaresh and Y. S. Lee // LiMnBO$_3$/C: A Potential Cathode Material for Lithium Batteries // Bull. Korean Chem. Soc. 31 (6), p. 1506–1508 (2010);

[110] S. Afyon, D. Kundu, F. Krumeich and R. Nesper // Nano LiMnBO$_3$, a high-capacity cathode material for Li-ion batteries // J. Power Sources 224, p. 145–151 (2013);

[111] L. Chen, Y. Zhao, X. An, J. Liu, Y. Dong, Y. Chen and Q. Kuang // Structure and electrochemical properties of LiMnBO$_3$ as a new cathode material for lithium-ion batteries // J. Alloys Compd. 494 (1–2), p. 415–419 (2010);

[112] K.-J. Lee, L.-S. Kang, S. Uhm, J. S. Yoon, D.-W. Kim and H. S. Hong // Synthesis and characterization of LiMnBO$_3$ cathode material for lithium ion batteries // Curr. Appl. Phys. 13 (7), p. 1440–1443 (2013);

[113] A. Yamada, N. Iwane, S. Nishimura, Y. Koyama and I. Tanaka // Synthesis and electrochemistry of monoclinic Li(Mn$_x$Fe$_{1-x}$)BO$_3$: a combined experimental and computational study // J. Mater. Chem. 21 (29), p. 10690 (2011);

[114] Y. Yamashita, P. Barpanda, Y. Yamada and A. Yamada // Demonstration of Co^{3+}/Co^{2+} Electrochemical Activity in LiCoBO$_3$ Cathode at 4.0 V // ECS Electrochem. Lett. 2 (8), p. A75–A77 (2013);

[115] Y. Fang, Q. Liu, L. Xiao, X. Ai, H. Yang and Y. Cao // High-Performance Olivine NaFePO$_4$ Microsphere Cathode Synthesized by Aqueous Electrochemical Displacement Method for Sodium Ion Batteries // ACS Appl. Mater. Interfaces 7 (32), p. 17977–17984 (2015);

[116] W. Tang, X. Song, Y. Du, C. Peng, M. Lin, S. Xi, B. Tian, J. Zheng, Y. Wu, F. Pan and K. P. Loh // High-performance $NaFePO_4$ formed by aqueous ion-exchange and its mechanism for advanced sodium ion batteries // J. Mater. Chem. A 4 (13), p. 4882–4892 (2016);

[117] G. Li, D. Jiang, H. Wang, X. Lan, H. Zhong and Y. Jiang // Glucose-assisted synthesis of $Na_3V_2(PO_4)_3$/C composite as an electrode material for high-performance sodium-ion batteries // J. Power Sources 265, p. 325–334 (2014);

[118] C. Zhu, K. Song, P. A. van Aken, J. Maier and Y. Yu // Carbon-coated $Na_3V_2(PO_4)_3$ embedded in porous carbon matrix: an ultrafast Na-storage cathode with the potential of outperforming Li cathodes // Nano Lett. 14 (4), p. 2175–2180 (2014);

[119] Y. Jiang, Z. Yang, W. Li, L. Zeng, F. Pan, M. Wang, X. Wei, G. Hu, L. Gu and Y. Yu // Nanoconfined Carbon-Coated $Na_3V_2(PO_4)_3$ Particles in Mesoporous Carbon Enabling Ultralong Cycle Life for Sodium-Ion Batteries // Adv. Energy Mater. 5 (10) (2015);

[120] H. Wang, D. Jiang, Y. Zhang, G. Li, X. Lan, H. Zhong, Z. Zhang and Y. Jiang // Self-combustion synthesis of $Na_3V_2(PO_4)_3$ nanoparticles coated with carbon shell as cathode materials for sodium-ion batteries // Electrochim. Acta 155, p. 23–28 (2015);

[121] J. Liu, K. Tang, K. Song, P. A. van Aken, Y. Yu and J. Maier // Electrospun $Na_3V_2(PO_4)_3$/C nanofibers as stable cathode materials for sodium-ion batteries // Nanoscale 6 (10), p. 5081–5086 (2014);

[122] S.-J. Lim, D.-W. Han, D.-H. Nam, K.-S. Hong, J.-Y. Eom, W.-H. Ryu and H.-S.

Kwon // Structural enhancement of $Na_3V_2(PO_4)_3$/C composite cathode materials by pillar ion doping or high power and long cycle life sodium-ion atteries // J. Mater. Chem. A 2, p. 19623–19632 (2014);

[123] W. Duan, Z. Zhu, H. Li, Z. Hu, K. Zhang, F. Cheng and J. Chen // $Na_3V_2(PO_4)_3$@C core–shell nanocomposites for rechargeable sodium-ion batteries // J. Mater. Chem. A 2 (23), p. 8668 (2014);

[124] Z. Jian, L. Zhao, H. Pan, Y.-S. Hu, H. Li, W. Chen and L. Chen // Carbon coated $Na_3V_2(PO_4)_3$ as novel electrode material for sodium ion batteries // Electrochem. commun. 14 (1), p. 86–89 (2012);

[125] H. Gao, Y. Li, K. Park and J. B. Goodenough // Sodium extraction from NASICON-structured $Na_3MnTi(PO_4)_3$ through Mn(III)/Mn(II) and Mn(IV)/Mn(III) redox couples // Chem. Mater. 28 (18), p. 6553–6559 (2016);

[126] F. Li, Y. Zhao, L. Xia, Z. Yang, J. Wei and Z. Zhou // Well-dispersed $Na_3V_2(PO_4)_2F_3$@rGO with improved kinetics for high-power sodium-ion batteries // J. Mater. Chem. A 8 (25), p. 12391–12397 (2020);

[127] S. Demirel, E. Oz, E. Altin, S. Altin, A. Bayri, P. Kaya, S. Turan and S. Avci // Growth mechanism and magnetic and electrochemical properties of $Na_{0.44}MnO_2$ nanorods as cathode material for Na-ion batteries // Mater. Charact. 105, p. 104–112 (2015);

[128] X. Tang, H. Liu, D. Su, P. H. L. Notten and G. Wang // Hierarchical sodium-rich Prussian blue hollow nanospheres as high-performance cathode for sodium-ion batteries // Nano Res. 11 (8), p. 3979–3990 (2018);

[129] J. Yan, X. Liu and B. Li // Nano-assembled Na_2FePO_4F/carbon nanotube multi-layered cathodes for Na-ion batteries // Electrochem. commun. 56, p. 46–50 (2015);

[130] K. Kubota, K. Yokoh, N. Yabuuchi and S. Komaba // Na_2CoPO_4F as a High-voltage Electrode Material for Na-ion Batteries // Electrochemistry 82 (10), p. 909–911 (2014);

[131] H. Kim, J. C. Kim, S.-H. Bo, T. Shi, D.-H. Kwon and G. Ceder // K-Ion Batteries Based on a P2-Type $K_{0.6}CoO_2$ Cathode // Adv. Energy Mater. 7 (17), p. 1700098 (2017);

[132] K. Chihara, A. Katogi, K. Kubota and S. Komaba // $KVPO_4F$ and $KVOPO_4$ toward 4 volt-class potassium-ion batteries // Chem. Commun. 53 (37), p. 5208–5211 (2017);

[133] N. Recham, G. Rousse, M. T. Sougrati, J.-N. Chotard, C. Frayret, S. Mariyappan, B. C. Melot, J.-C. Jumas and J.-M. Tarascon // Preparation and Characterization of a Stable $FeSO_4F$-Based Framework for Alkali Ion Insertion Electrodes // Chem. Mater. 24 (22), p. 4363–4370 (2012);

[134] C. Zhang, Y. Xu, M. Zhou, L. Liang, H. Dong, M. Wu, Y. Yang and Y. Lei // Potassium Prussian Blue Nanoparticles: A Low-Cost Cathode Material for Potassium-Ion Batteries // Adv. Funct. Mater. 27 (4), p. 1604307 (2016);

[135] X. Bie, T. Hosaka, K. Kubota, K. Chihara and S. Komaba // Synthesis and Electrochemical Properties of K-Rich Prussian Blue for Non-Aqueous Potassium Batteries // Meet. Abstr. MA2016-03 (2), p. 369 (2016);

[136] X. Jiang, T. Zhang, L. Yang, G. Li and J. Y. Lee // A Fe/Mn-Based Prussian Blue

Analogue as a K-Rich Cathode Material for Potassium-Ion Batteries // ChemElectroChem 4 (9), p. 2237–2242 (2017);

[137] F. Sauvage, J.-M. Tarascon, E. Baudrin and L. Laffont // Study of the Insertion/Deinsertion Mechanism of Sodium into $Na_{0.44}MnO_2$ // Inorg. Chem. 46, p. 3289−3294 (2007);

[138] W. G. Mumme // The structure of $Na_4Mn_4Ti_5O_{18}$ // Acta Crystallogr. Sect. B 24 (8), p. 1114–1120 (1968);

[139] C. Ferrara, C. Tealdi, V. Dall'Asta, D. Buchholz, L. Chagas, E. Quartarone, V. Berbenni and S. Passerini // High-Performance $Na_{0.44}MnO_2$ Slabs for Sodium-Ion Batteries Obtained through Urea-Based Solution Combustion Synthesis // Batteries 4 (1), p. 8 (2018);

[140] C. Liu, W. Guo, Q. Wang, J. Li and X.-P. Yang // Parametric study of hydrothermal soft chemical synthesis and application of $Na_{0.44}MnO_2$ nanorods for Li-ion battery cathode materials: Synthesis conditions and electrochemical performance // J. Alloys Compd. 658, p. 588–594 (2016);

[141] E. Hosono, T. Saito, J. Hoshino, M. Okubo, Y. Saito, D. Nishio-Hamane, T. Kudo and H. Zhou // High power Na-ion rechargeable battery with single-crystalline $Na_{0.44}MnO_2$ nanowire electrode // J. Power Sources 217, p. 43–46 (2012);

[142] B. L. Ellis and L. F. Nazar // Sodium and sodium-ion energy storage batteries // Curr. Opin. Solid State Mater. Sci. 16 (4), p. 168–177 (2012);

[143] X. Li, D. Wu, Y.-N. Zhou, L. Liu, X.-Q. Yang and G. Ceder // O3-type $Na(Mn_{0.25}Fe_{0.25}Co_{0.25}Ni_{0.25})O_2$: A quaternary layered cathode compound for

rechargeable Na ion batteries // Electrochem. commun. 49, p. 51–54 (2014);

[144] D. Buchholz, C. Vaalma, L. G. Chagas and S. Passerini // Mg-doping for improved long-term cyclability of layered Na-ion cathode materials – The example of P2-type $NaxMg_{0.11}Mn_{0.89}O_2$ // J. Power Sources 282, p. 581–585 (2015);

[145] S. C. Han, H. Lim, J. Jeong, D. Ahn, W. B. Park, K.-S. Sohn and M. Pyo // Ca-doped Na_xCoO_2 for improved cyclability in sodium ion batteries // J. Power Sources 277, p. 9–16 (2015);

[146] W. Zhao, H. Kirie, A. Tanaka, M. Unno, S. Yamamoto and H. Noguchi // Synthesis of metal ion substituted $P2-Na_{2/3}Ni_{1/3}Mn_{2/3}O_2$ cathode material with enhanced performance for Na ion batteries // Mater. Lett. 135, p. 131–134 (2014);

[147] X. Wu, J. Guo, D. Wang, G. Zhong, M. J. McDonald and Y. Yang // P2-type $Na_{0.66}Ni_{0.33-x}Zn_xMn_{0.67}O_2$ as new high-voltage cathode materials for sodium-ion batteries // J. Power Sources 281, p. 18–26 (2015);

[148] Y. Zhang, R. Zhang and Y. Huang // Air-Stable Na_xTMO_2 Cathodes for Sodium Storage // Front Chem. 7, p. 335 (2019);

[149] X. Zhang, Y. Yang, X. Qu, Z. Wei, G. Sun, K. Zheng, H. Yu and F. Du // Layered P2-Type $K_{0.44}Ni_{0.22}Mn_{0.78}O_2$ as a High-Performance Cathode for Potassium-Ion Batteries // Adv. Funct. Mater. 29 (49), p. 1905679 (2019);

[150] B. L. Ellis, W. R. M. Makahnouk, W. N. Rowan-Weetaluktuk, D. H. Ryan and L. F. Nazar // Crystal Structure and Electrochemical Properties of A_2MPO_4F Fluorophosphates (A = Na, Li; M = Fe, Mn, Co, Ni)† // Chem. Mater. 22 (3), p. 1059–1070 (2010);

[151] N. V Kosova, V. R. Podugolnikov, E. T. Devyatkina and A. B. Slobodyuk // Structure and electrochemistry of $NaFePO_4$ and Na_2FePO_4F cathode materials prepared *via* mechanochemical route // Mater. Res. Bull. 60, p. 849–857 (2014);

[152] H. Kim, R. a. Shakoor, C. Park, S. Y. Lim, J.-S. Kim, Y. N. Jo, W. Cho, K. Miyasaka, R. Kahraman, Y. Jung and J. W. Choi // $Na_2FeP_2O_7$: A Safe Cathode for Rechargeable Sodium-ion Batteries // Adv. Funct. Mater., p. 3480–3487 (2012);

[153] A. J. Fernández-Ropero, M. Zarrabeitia, M. Reynaud, T. Rojo and M. Casas-Cabanas // Toward Safe and Sustainable Batteries: $Na_4Fe_3(PO_4)_2P_2O_7$ as a Low-Cost Cathode for Rechargeable Aqueous Na-Ion Batteries // J. Phys. Chem. C 122 (1), p. 133–142 (2018);

[154] P. Barpanda, G. Oyama, S. I. Nishimura, S. C. Chung and A. Yamada // A 3.8-V earth-abundant sodium battery electrode // Nat. Commun. 5, p. 1–8 (2014);

[155] B. Rousseau, V. Timoshevskii, N. Mousseau, M. Côté and K. Zaghib // $Na_3Fe_2(SO_4)_2(SO_3N)$ as a potential high capacity cathode material // Mater. Sci. Eng. B 211, p. 185–190 (2016);

[156] R. B. Araujo, S. Chakraborty, P. Barpanda and R. Ahuja // $Na_2M_2(SO_4)_3$ (M = Fe, Mn, Co and Ni): Towards high-voltage sodium battery applications // Phys. Chem. Chem. Phys. 18 (14), p. 9658–9665 (2016);

[157] J. Gao, X. Sha, X. Liu, L. Song and P. Zhao // Preparation, structure and properties of $Na_2Mn_3(SO_4)_4$: a new potential candidate with high voltage for Na-ion batteries // J. Mater. Chem. A 4 (30), p. 11870–11877 (2016);

[158] W. Ko, T. Park, H. Park, Y. Lee, K. E. Lee and J. Kim // $Na_{0.97}KFe(SO_4)_2$: an iron-

based sulfate cathode material with outstanding cyclability and power capability for Na-ion batteries // J. Mater. Chem. A 6 (35), p. 17095–17100 (2018);

[159] S. Park, J. Song, S. Kim, B. Sambandam, V. Mathew, S. Kim, J. Jo, S. Kim and J. Kim // Phase-pure $Na_3V_2(PO_4)_2F_3$ embedded in carbon matrix through a facile polyol synthesis as a potential cathode for high performance sodium-ion batteries // Nano Res. 12 (4), p. 911–917 (2019);

[160] Z.-Y. Gu, J.-Z. Guo, Y. Yang, H.-Y. Yu, X.-T. Xi, X.-X. Zhao, H.-Y. Guan, X. He and X.-L. Wu // Precisely controlled preparation of an advanced $Na_3V_2(PO_4)_2O_2F$ cathode material for sodium ion batteries: the optimization of electrochemical properties and electrode kinetics // Inorg. Chem. Front. 6 (4), p. 988–995 (2019);

[161] W. B. Park, S. C. Han, C. Park, S. U. Hong, U. Han, S. P. Singh, Y. H. Jung, D. Ahn, K.-S. Sohn and M. Pyo // KVP_2O_7 as a Robust High-Energy Cathode for Potassium-Ion Batteries: Pinpointed by a Full Screening of the Inorganic Registry under Specific Search Conditions // Adv. Energy Mater. 8 (13), p. 1703099 (2018);

[162] O. A. Drozhzhin, I. V Tertov, A. M. Alekseeva, D. A. Aksyonov, K. J. Stevenson, A. M. Abakumov and E. V Antipov // β-$NaVP_2O_7$ as a Superior Electrode Material for Na-Ion Batteries // Chem. Mater. 31 (18), p. 7463–7469 (2019);

[163] J. Liao, Q. Hu, J. Mu, X. He, S. Wang and C. Chen // A vanadium-based metal–organic phosphate framework material $K_2[(VO)_2(HPO_4)_2(C_2O_4)]$ as a cathode for potassium-ion batteries // Chem. Commun. 55 (5), p. 659–662 (2019);

[164] M. V Zakharkin, O. A. Drozhzhin, I. V Tereshchenko, D. Chernyshov, A. M. Abakumov, E. V Antipov and K. J. Stevenson // Enhancing Na^+ Extraction Limit

through High Voltage Activation of the NASICON-Type $Na_4MnV(PO_4)_3$ Cathode // ACS Appl. Energy Mater. 1 (11), p. 5842–5846 (2018);

[165] W. Zhou, L. Xue, X. Lü, H. Gao, Y. Li, S. Xin, G. Fu, Z. Cui, Y. Zhu and J. B. Goodenough // $Na_xMV(PO_4)_3$ (M = Mn, Fe, Ni) Structure and Properties for Sodium Extraction // Nano Lett. 16 (12), p. 7836–7841 (2016);

[166] A. Criado, P. Lavela, C. Pérez-Vicente, G. F. Ortiz and J. L. Tirado // Effect of chromium doping on $Na_3V_2(PO_4)_2F_3$@C as promising positive electrode for sodium-ion batteries // J. Electroanal. Chem. 856, p. 113694 (2020);

[167] X. Rui, Q. Yan, M. Skyllas-Kazacos and T. M. Lim // $Li_3V_2(PO_4)_3$ cathode materials for lithium-ion batteries: A review // J. Power Sources 258, p. 19–38 (2014);

[168] R. K. B. Gover, P. Burns, A. Bryan, M. Y. Saidi, J. L. Swoyer and J. Barker // $LiVPO_4F$: A new active material for safe lithium-ion batteries // Solid State Ionics 177 (26), p. 2635–2638 (2006);

[169] S. S. Fedotov, N. R. Khasanova, A. S. Samarin, O. A. Drozhzhin, D. Batuk, O. M. Karakulina, J. Hadermann, A. M. Abakumov and E. V. Antipov // $AVPO_4F$ (A = Li, K): A 4 V Cathode Material for High-Power Rechargeable Batteries // Chem. Mater. 28 (2), p. 411–415 (2016);

[170] A. Paolella, C. Faure, V. Timoshevskii, S. Marras, G. Bertoni, A. Guerfi, A. Vijh, M. Armand and K. Zaghib // A review on hexacyanoferrate-based materials for energy storage and smart windows: challenges and perspectives // J. Mater. Chem. A 5 (36), p. 18919–18932 (2017);

[171] D. B. Brown, D. F. Shriver and L. H. Schwartz // Solid-State Reactions of Iron(II)

Hexacyanochromate(III) // Inorg. Chem. 7 (1), p. 77–83 (1968);

[172] E. Reguera, J. A. Bertrán and L. Nuñez // Study of the Linkage Isomerization Process in Hexacyanometallates // Polyhedron 13 (10), p. 1619–1624 (1994);

[173] X. Bie, K. Kubota, T. Hosaka, K. Chihara and S. Komaba // Synthesis and electrochemical properties of Na-rich Prussian blue analogues containing Mn, Fe, Co and Fe for Na-ion batteries // J. Power Sources 378, p. 322–330 (2018);

[174] X. Bie, K. Kubota, T. Hosaka, K. Chihara and S. Komaba // A novel K-ion battery: hexacyanoferrate(ii)/graphite cell // J. Mater. Chem. A 5 (9), p. 4325–4330 (2017);

[175] L. Xue, Y. Li, H. Gao, W. Zhou, X. Lü, W. Kaveevivitchai, A. Manthiram and J. B. Goodenough // Low-Cost High-Energy Potassium Cathode // J. Am. Chem. Soc. 139 (6), p. 2164–2167 (2017);

[176] Y. Sun, C. Liu, J. Xie, D. Zhuang, W. Zheng and X. Zhao // Potassium manganese hexacyanoferrate/graphene as a high-performance cathode for potassium-ion batteries // New J. Chem. 43 (29), p. 11618–11625 (2019);

[177] S. Mukherjee, A. Bates, N. Schuppert, B. Son, J. G. Kim, J. S. Choi, M. J. Choi, D.-H. Lee, O. Kwon, J. Jasinski and S. Park // A study of a novel Na ion battery and its anodic degradation using sodium rich prussian blue cathode coupled with different titanium based oxide anodes // J. Power Sources 286, p. 276–289 (2015);

[178] Y. Yang, E. Liu, X. Yan, C. Ma, W. Wen, X.-Z. Liao and Z.-F. Ma // Influence of Structural Imperfection on Electrochemical Behavior of Prussian Blue Cathode Materials for Sodium Ion Batteries // J. Electrochem. Soc. 163 (9), p. A2117–A2123 (2016);

[179] G. He and L. F. Nazar // Crystallite Size Control of Prussian White Analogues for Nonaqueous Potassium-Ion Batteries // ACS Energy Lett. 2 (5), p. 1122–1127 (2017);

[180] J. Song, L. Wang, Y. Lu, J. Liu, B. Guo, P. Xiao, J.-J. Lee, X.-Q. Yang, G. Henkelman and J. B. Goodenough // Removal of Interstitial H_2O in Hexacyanometallates for a Superior Cathode of a Sodium-Ion Battery // J. Am. Chem. Soc. 137 (7), p. 2658–2664 (2015);

[181] H.-C. Dinh, S. Mho, Y. Kang and I.-H. Yeo // Large discharge capacities at high current rates for carbon-coated $LiMnPO_4$ nanocrystalline cathodes // J. Power Sources 244, p. 189–195 (2013);

[182] N. Meethong, Y.-H. Kao, S. A. Speakman and Y.-M. Chiang // Aliovalent Substitutions in Olivine Lithium Iron Phosphate and Impact on Structure and Properties // Adv. Funct. Mater. 19 (7), p. 1060–1070 (2009);

[183] K. Byrappa and M. Yoshimura // Hydrothermal Technology for Nanotechnology—A Technology for Processing of Advanced Materials. // Chapter 10 in *Handbook of Hydrothermal Technology*, 2nd ed., p. 615–762 (2013);

[184] X. Huang, J. Ma, P. Wu, Y. Hu, J. Dai, Z. Zhu, H. Chen and H. Wang // Hydrothermal synthesis of $LiCoPO_4$ cathode materials for rechargeable lithium ion batteries // Mater. Lett. 59 (5), p. 578–582 (2005);

[185] J. Chen, S. Wang and M. S. Whittingham // Hydrothermal synthesis of cathode materials // J. Power Sources 174 (2), p. 442–448 (2007);

[186] J. Chen, M. J. Vacchio, S. Wang, N. Chernova, P. Y. Zavalij and M. S. Whittingham

// The hydrothermal synthesis and characterization of olivines and related compounds for electrochemical applications // Solid State Ionics 178 (31–32), p. 1676–1693 (2008);

[187] F. Wang, J. Yang, Y. NuLi and J. Wang // Novel hedgehog-like 5 V LiCoPO$_4$ positive electrode material for rechargeable lithium battery // J. Power Sources 196 (10), p. 4806–4810 (2011);

[188] R. Zhao, I. M. Hung, Y.-T. Li, H. Chen and C.-P. Lin // Synthesis and properties of Co-doped LiFePO$_4$ as cathode material via a hydrothermal route for lithium-ion batteries // J. Alloys Compd. 513 (0), p. 282–288 (2012);

[189] A. Douy // Polyacrylamide gel: an efficient tool for easy synthesis of multicomponent oxide precursors of ceramics and glasses // Int. J. Inorg. Mater. 3 (7), p. 699–707 (2001);

[190] G. Carabalí, E. Chavira, I. Castro, E. Bucio, L. Huerta and J. Jiménez-Mier // Novel sol–gel methodology to produce LaCoO$_3$ by acrylamide polymerization assisted by γ-irradiation // Radiat. Phys. Chem. 81 (5), p. 512–518 (2012);

[191] S. Wu, Y. Liu, L. He and F. Wang // Preparation of β-spodumene-based glass–ceramic powders by polyacrylamide gel process // Mater. Lett. 58 (22), p. 2772–2775 (2004);

[192] K. Kubota, M. Dahbi, T. Hosaka, S. Kumakura and S. Komaba // Towards K-Ion and Na-Ion Batteries as "Beyond Li-Ion" // Chem. Rec. 18 (4), p. 459–479 (2018);

[193] S. Venkatraman and A. Manthiram // Synthesis and Characterization of P3-Type CoO$_{2-\delta}$ // Chem. Mater. 14 (9), p. 3907–3912 (2002);

[194] S.-H. Bo, G. M. Veith, M. R. Saccomanno, H. Huang, P. V Burmistrova, A. C. Malingowski, R. L. Sacci, K. R. Kittilstved, C. P. Grey and P. G. Khalifah // Thin-film and bulk investigations of $LiCoBO_3$ as a Li-ion battery cathode. // ACS Appl. Mater. Interfaces 6 (14), p. 10840–8 (2014);

[195] S. Afyon, C. Mensing, F. Krumeich and R. Nesper // The electrochemical activity for nano-$LiCoBO_3$ as a cathode material for Li-ion batteries // Solid State Ionics 256, p. 103–108 (2014);

[196] F. Sanz, C. Parada and C. Ruíz-Valero // Crystal growth, crystal structure and magnetic properties of disodium cobalt fluorophosphate // J. Mater. Chem. 11 (1), p. 208–211 (2001);

[197] J. Zhou, J. Zhou, Y. Tang, Y. Bi, C. Wang, D. Wang and S. Shi // Synthesis of Na_2FePO_4F/C and its electrochemical performance // Ceram. Int. 39 (5), p. 5379–5385 (2013);

[198] R. Berthelot, D. Carlier and C. Delmas // Electrochemical investigation of the P2–Na_xCoO_2 phase diagram // Nat. Mater. 10 (1), p. 74–80 (2011);

[199] Y. S. Meng, Y. Hinuma and G. Ceder // An investigation of the sodium patterning in Na_xCoO_2 ($0.5 \leq x \leq 1$) by density functional theory methods // J. Chem. Phys. 128 (10), p. 104708 (2008);

[200] R. Qiao, K. Dai, J. Mao, T.-C. Weng, D. Sokaras, D. Nordlund, X. Song, V. S. Battaglia, Z. Hussain, G. Liu and W. Yang // Revealing and suppressing surface Mn(II) formation of $Na_{0.44}MnO_2$ electrodes for Na-ion batteries // Nano Energy 16, p. 186–195 (2015);

[201] O. V. Yakubovich, O. Karimova and O. K. Mel'nikov // The Mixed Anionic Framework in the Structure of $Na_2\{MnF[PO_4]\}$ // Acta Crystallogr. Sect. C 53 (4), p. 395–397 (1997);

[202] A. Leclaire and B. Raveau // The actual structure of $K_6(VO)_2(V_2O_3)_2(PO_4)_4(P_2O_7)$: Ordered distribution of P_2O_7 groups and charge ordering of vanadium // J. Solid State Chem. 179 (1), p. 205–211 (2006);

[203] R. Lian, D. Wang, X. Ming, R. Zhang, Y. Wei, J. Feng, X. Meng and G. Chen // Phase transformation, ionic diffusion and charge transfer mechanisms of $KVOPO_4$ in potassium ion batteries: first-principles calculations // J. Mater. Chem. A 6 (33), p. 16228–16234 (2018);

[204] J. B. Leriche, S. Hamelet, J. Shu, M. Morcrette, C. Masquelier, G. Ouvrard, M. Zerrouki, P. Soudan, S. Belin, E. Elkaïm and F. Baudelet // An Electrochemical Cell for *Operando* Study of Lithium Batteries Using Synchrotron Radiation // J. Electrochem. Soc. 157 (5), p. A606–A610 (2010);

[205] O. A. Drozhzhin, I. V. Tereshchenko, H. Emerich, E. V. Antipov, A. M. Abakumov and D. Y. Chernyshov // An electrochemical cell with sapphire windows for *operando* synchrotron X-ray powder diffraction and spectroscopy studies of high-power and high-voltage electrodes for metal-ion batteries // J. Synchrotron Radiat. 25 (2), p. 468–472 (2018);

[206] K. Momma and F. Izumi // *VESTA 3* for three-dimensional visualization of crystal, volumetric and morphology data // J. Appl. Crystallogr. 44 (6), p. 1272–1276 (2011);

[207] Rodriguez-Carvajal and T. J Roisnel // FullProf.98 and WinPLOTR: New Windows 95/NT Applications for Diffraction // Comm. Powder Diffr. Int. Union Crystallogr. 20 (May-August) (1998);

[208] V. Petříček, M. Dušek and L. Palatinus // Crystallographic Computing System JANA2006: General features // Zeitschrift für Kristallographie - Crystalline Materials, 229 (5), p. 345–352 (2014);

[209] G. Kresse and J. Furthmüller // Efficiency of ab-initio total energy calculations for metals and semiconductors using a plane-wave basis set // Comput. Mater. Sci. 6 (1), p. 15–50 (1996);

[210] J. P. Perdew, K. Burke and M. Ernzerhof // Generalized Gradient Approximation Made Simple // Phys. Rev. Lett. 77 (18), p. 3865–3868 (1996);

[211] S. L. Dudarev, G. A. Botton, S. Y. Savrasov, C. J. Humphreys and A. P. Sutton // Electron-energy-loss spectra and the structural stability of nickel oxide: An LSDA+U study // Phys. Rev. B 57 (3), p. 1505–1509 (1998);

[212] B. Meredig, A. Thompson, H. A. Hansen, C. Wolverton and A. van de Walle // Method for locating low-energy solutions within DFT+U // Phys. Rev. B 82 (19), p. 195128 (2010);

[213] A. van de Walle, M. Asta and G. Ceder // The alloy theoretic automated toolkit: A user guide // Calphad 26 (4), p. 539–553 (2002);

[214] A. Togo and I. Tanaka // First principles phonon calculations in materials science // Scr. Mater. 108, p. 1–5 (2015);

[215] Y. Piffard, K. K. Rangan, Y. An, D. Guyomard and M. Tournoux // Cobalt Lithium

Orthoborate, $LiCoBO_3$ // Acta Crystallogr. Sect. C Cryst. Struct. Commun. 54 (11), p. 1561–1563 (1998);

[216] H. Yamaguchi, K. Akatsuka, M. Setoguchi and Y. Takaki // Structure of cobalt dilithium silicate β_{II}-Li_2CoSiO_4 // Acta Crystallogr. Sect. B 35 (11), p. 2680–2682 (1979);

[217] J. Ludwig, D. Nordlund, M. M. Doeff and T. Nilges // Synthesis and characterization of metastable, 20 nm-sized *Pna*2_1-$LiCoPO_4$ nanospheres // J. Solid State Chem. 248, p. 9–17 (2017);

[218] M. Wintenberger and B. Lambert-Andron // Structures magnétiques de Na_2CoSio_4 et Na_2CoGeO_4 // Phys. status solidi 18 (1), p. 209–213 (1973);

[219] I. V. Tereshchenko, D. A. Aksyonov, O. A. Drozhzhin, I. A. Presniakov, A. V Sobolev, A. Zhugayevych, D. Striukov, K. J. Stevenson, E. V Antipov and A. M. Abakumov // The Role of Semilabile Oxygen Atoms for Intercalation Chemistry of the Metal-Ion Battery Polyanion Cathodes. // J. Am. Chem. Soc. 140 (11), p. 3994–4003 (2018);

[220] M. E. Arroyo y de Dompablo, A. Van der Ven and G. Ceder // First-principles calculations of lithium ordering and phase stability on Li_xNiO_2 // Phys. Rev. B 66 (6), p. 64112 (2002);

[221] H. Zou, S. Li, X. Wu, M. J. McDonald and Y. Yang // Spray-Drying Synthesis of Pure Na_2CoPO_4F as Cathode Material for Sodium Ion Batteries // ECS Electrochem. Lett. 4 (6), p. A53–A55 (2015);

[222] J. A. Santana, J. Kim, P. R. C. Kent and F. A. Reboredo // Successes and failures of

Hubbard-corrected density functional theory: The case of Mg doped $LiCoO_2$ // J. Chem. Phys. 141 (16), p. 164706 (2014);

[223] S. M. Wood, C. Eames, E. Kendrick and M. S. Islam // Sodium-Ion Diffusion and Voltage Trends in Phosphates $Na_4M_3(PO_4)_2P_2O_7$ (M = Fe, Mn, Ni, Co) for Possible High Rate Cathodes // J. Phys. Chem. C 119 (28), p. 15935–15941 (2015);

[224] M. Kim, D. Kim, W. Lee, H. M. Jang and B. Kang // New Class of 3.7 V Fe-Based Positive Electrode Materials for Na-Ion Battery Based on Cation-Disordered Polyanion Framework // Chem. Mater. 30 (18), p. 6346–6352 (2018);

[225] H. T. Stokes, D. M. Hatch, B. J. Campbell and D. E. Tanner // *ISODISPLACE*: a web-based tool for exploring structural distortions // J. Appl. Crystallogr. 39 (4), p. 607–614 (2006);

[226] D. A. Aksyonov, S. S. Fedotov, K. J. Stevenson and A. Zhugayevych // Understanding migration barriers for monovalent ion insertion in transition metal oxide and phosphate based cathode materials: A DFT study // Comput. Mater. Sci. 154, p. 449–458 (2018);

[227] S. S. Fedotov, A. S. Samarin, V. A. Nikitina, D. A. Aksyonov, S. A. Sokolov, A. Zhugayevych, K. J. Stevenson, N. R. Khasanova, A. M. Abakumov and E. V Antipov // Reversible facile Rb^+ and K^+ ions de/insertion in a $KTiOPO_4$-type $RbVPO_4F$ cathode material // J. Mater. Chem. A 6 (29), p. 14420–14430 (2018);

[228] M. Kunz and T. Armbruster // Applications and limitations of the ionic potential model with empirically derived ion-specific repulsion parameters // Acta Crystallogr. Sect. B 48 (5), p. 609–622 (1992).

7. Supplementary information

Figure S1. PXRD pattern and Rietveld refinement profile of the $LiCoBO_3$ obtained hydrothermally (λ=1.78897Å) and the SEM micrograph (inset) of the sample of $LiCoBO_3$/C calcined at 500°C. Adapted from "Novel synthetic approaches to $LiCoBO_3$ cathode material and its electrochemical properties" // O. A. Drozhzhin, I. V. Tereshchenko, E. V. Antipov, Ceram. Int. 43 (5), p. 4670-4673. Copyright 2017, with permission from Elsevier. Available from https://www.sciencedirect.com/science/article/pii/S0272884216324178.
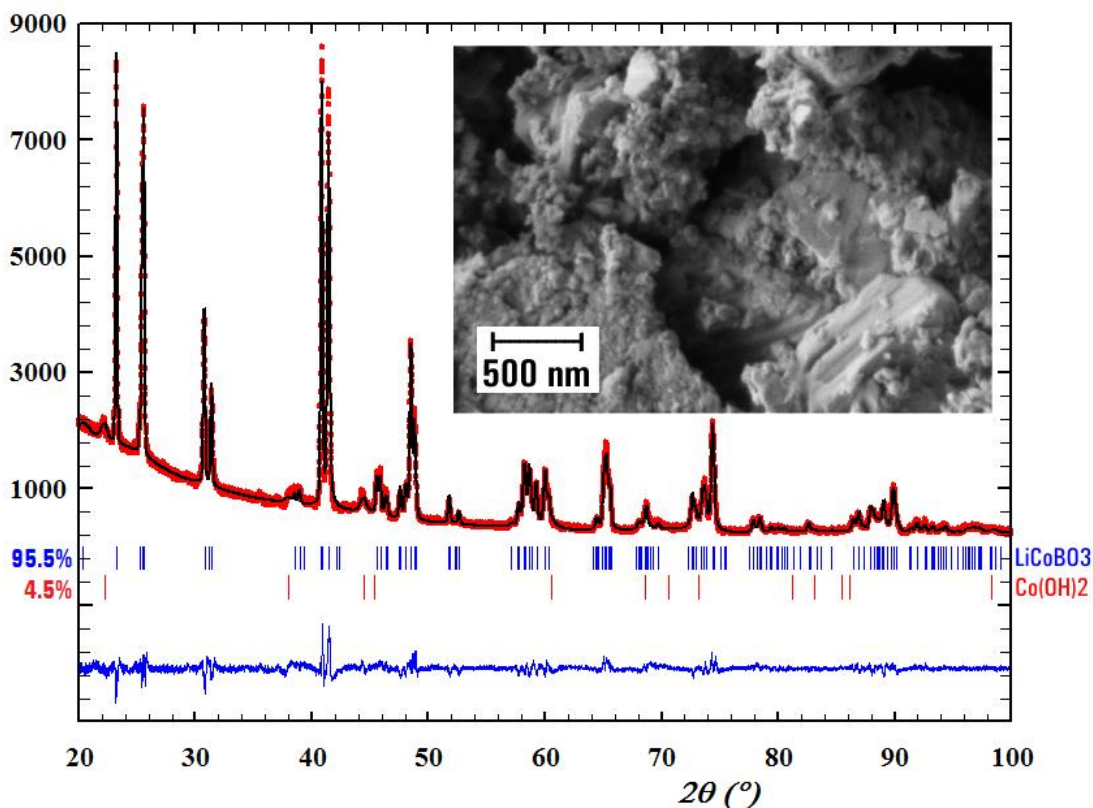
Table S1. Atomic coordinates and occupancies of LiCoBO$_3$ refined with isotropic thermal parameters using PXRD data from Figure S1. Rp=0.05, Rwp=0.06, Rf=0.05, GOF=1.80; mass fraction of Co(OH)$_2$=4.5%±0.4%. Adapted from "Novel synthetic approaches to LiCoBO$_3$ cathode material and its electrochemical properties" // O. A. Drozhzhin, I. V. Tereshchenko, E. V. Antipov, Ceram. Int. 43 (5), p. 4670-4673. Copyright 2017, with permission from Elsevier. Available from https://www.sciencedirect.com/science/article/pii/S0272884216324178.

Label	x/a	y/b	z/c	Occupancy	Uiso, Å^2
Co	0.159(2)	0.330(2)	0.123(1)	0.89(2)	0.003(1)
Li	0.13(2)	-0.03(2)	0.122(8)	1	0.03(1)
B	0.67(1)	0.16(1)	0.132(5)	1	0.01(1)
O1	0.395(4)	0.165(3)	0.093(2)	1	0.003(1)
O2	0.772(4)	0.307(3)	0.152(3)	1	0.03(1)

Figure S2. SXPD pattern, Rietveld refinement profile and SEM micrograph (inset) of the Na$_2$FePO$_4$F/C (λ=0.78508Å); three strongest aluminum reflections are used as internal standard for the refinement of the sample shift and were excluded after refinement for clearer picture.
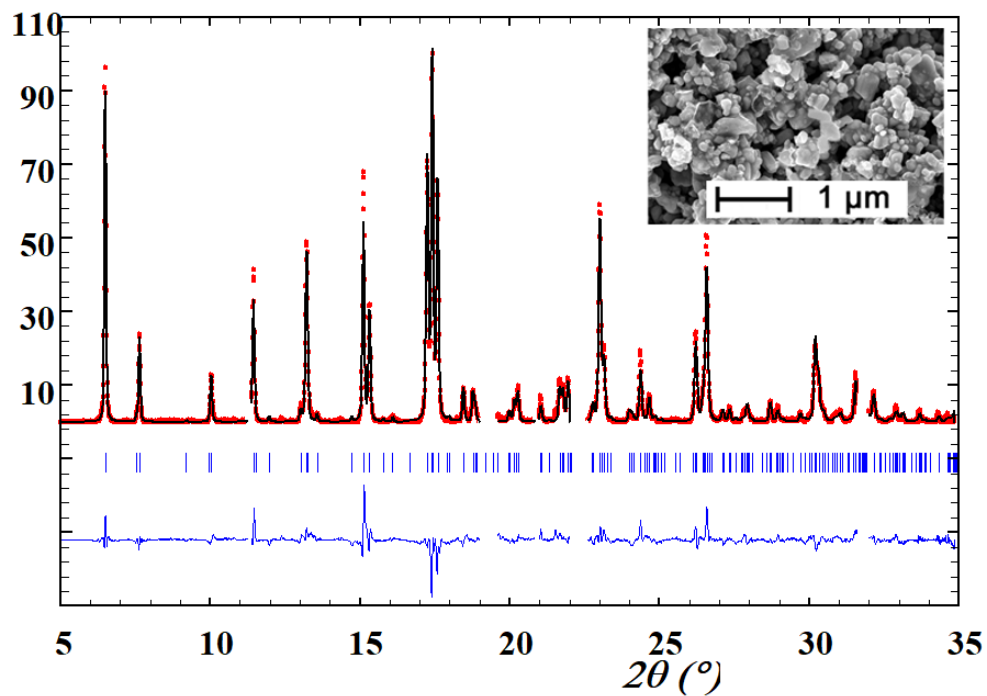
Figure S3. PXRD pattern, Rietveld refinement profile and SEM micrograph (inset) of the Na$_2$CoPO$_4$F/C (λ=1.78897Å).
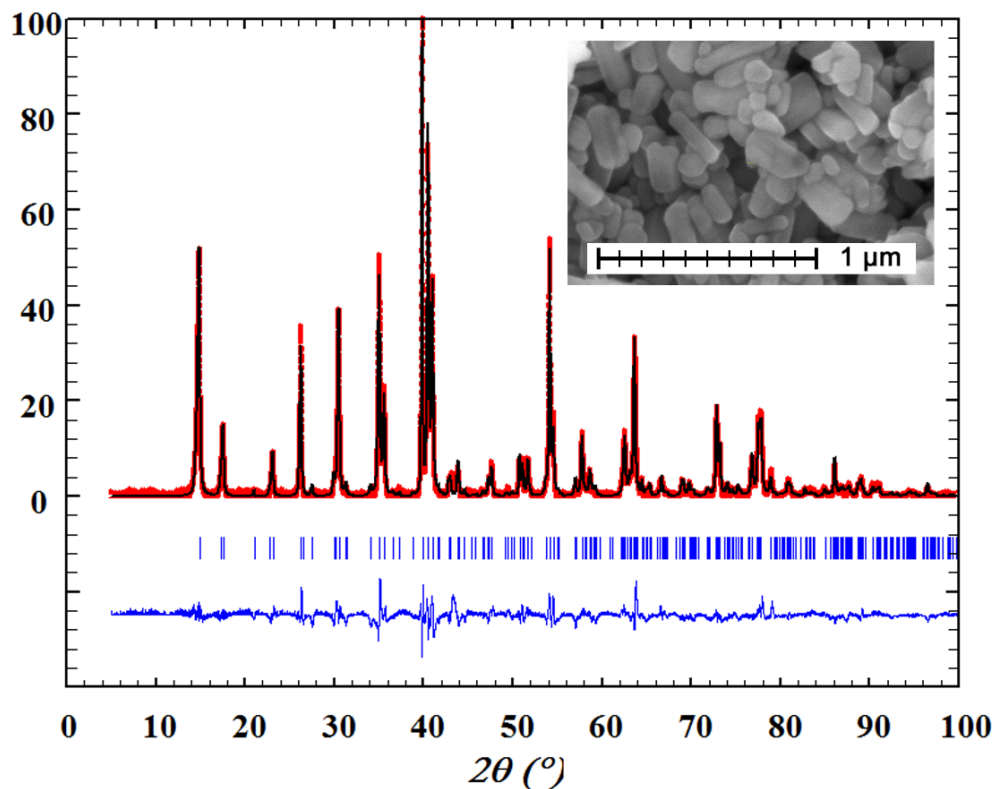
Table S2. Unit cell parameters for compounds with formula Na$_2$Mn$_{1-x}$Fe$_x$PO$_4$F with space group $P2_1/n$ refined by Le Bail method with a fixed structure model of Na$_2$MnPO$_4$F (#01-087-0467).

x in Na$_2$Mn$_{1-x}$Fe$_x$A (A=PO$_4$F)	0 (Rietveld)	0.2	0.4	0.6	0.8
a, Å	13.681(9)	13.6574(15)	13.649(4)	13.626(7)	Two-phase sample with strong overlapping of reflections of both phases
b, Å	5.316(2)	5.3051(4)	5.2975(6)	5.290(1)	
c, Å	13.709(8)	13.695(1)	13.672(2)	13.649(4)	
β, °	119.69(3)	119.63(1)	119.61(1)	119.59(2)	
V, Å^3	866.2(9)	862.55(14)	859.5(3)	855.6(6)	
R$_p$	0.024	0.021	0.013	0.013	
R$_{wp}$	0.035	0.034	0.020	0.019	
GOF	1.94	8.11	5.14	4.03	

Table S3. Unit cell parameters for compounds with formula $Na_2Fe_{1-x}Mg_xPO_4F$ with space group *Pbcn* refined by Le Bail method (except x=0).

x in $Fe_{1-x}Mg_x$	0 (Rietveld)	0.1	0.25	0.5
a, Å	5.2344(2)	5.2222(4)	5.228(1)	5.230(1)
b, Å	13.8443(5)	13.827(2)	13.821(3)	13.744(2)
c, Å	11.7757(4)	11.759(1)	11.750(2)	11.751(2)
V, Å^3	853.34(6)	849.1(1)	849.0(2)	844.7(2)
R_p	0.160	0.023	0.031	0.007
R_{wp}	0.122	0.030	0.047	0.009
GOF	1.6	1.26	2.38	2.01

Table S4. Unit cell parameters for compounds with formula $Na_2Co_{1-x}Mn_xPO_4F$ with space groups *Pbcn* and $P2_1/n$ refined by Le Bail method (except x=0 and x=1)

x in $Co_{1-x}Mn_x$	0 (Rietveld)	0.2	0.4	0.6	0.8	1 (Rietveld)
Space group	Pbcn			P2$_1$/n		
a, Å	5.2416(7)	5.2562(2)	5.2715(3)	13.601(1)	13.635(1)	13.681(9)
b, Å	13.779(2)	13.8008(6)	13.8298(8)	5.2974(3)	5.3069(2)	5.316(2)
c, Å	11.688(2)	11.7237(5)	11.7616(6)	13.642(1)	13.674(1)	13.709(8)
β, °	90	90	90	119.619(4)	119.625(3)	119.69(3)
V, Å^3	844.2(2)	850.5(1)	857.5(1)	854.5(1)	860.1(1)	866.2(9)
R_p	0.208	0.006	0.008	0.093	0.084	0.024
R_{wp}	0.117	0.007	0.012	0.139	0.129	0.035
GOF	0.8	2.17	3.42	1.89	1.73	1.94

Table S5. Results of the analysis of metallic composition in $Na_2Fe_{1-x}Mg_xPO_4F$ by ICP-MS (number of measurements = 3) normalized per the total content of Fe and Mg for better clarity.

x in $Na_2Fe_{1-x}Mg_xPO_4F$		0	0.1	0.25	0.5
Number of atoms per formula unit	Na	2.098±0.058	1.822±0.047	1.888±0.060	1.952±0.057
	Fe	0.994±0.003	0.876±0.012	0.721±0.014	0.453±0.009
	Mg	0.006±0.0001	0.124±0.003	0.279±0.007	0.547±0.017

Figure S4. A representative EDX spectrum of the obtained sample of Na_2CoPO_4F/C.
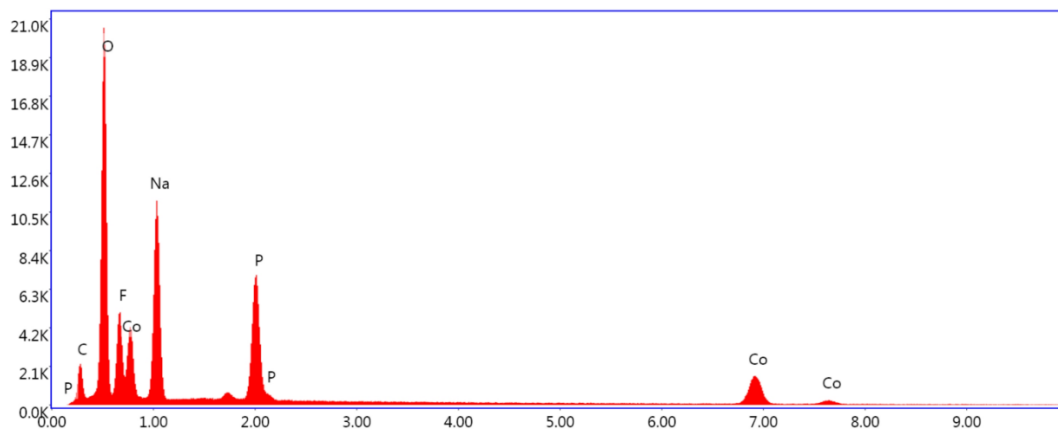
Figure S5. PXRD patterns of calcined samples of $Na_2Co_{1-x}Mn_xPO_4F$ ($\lambda=1.5406Å$).
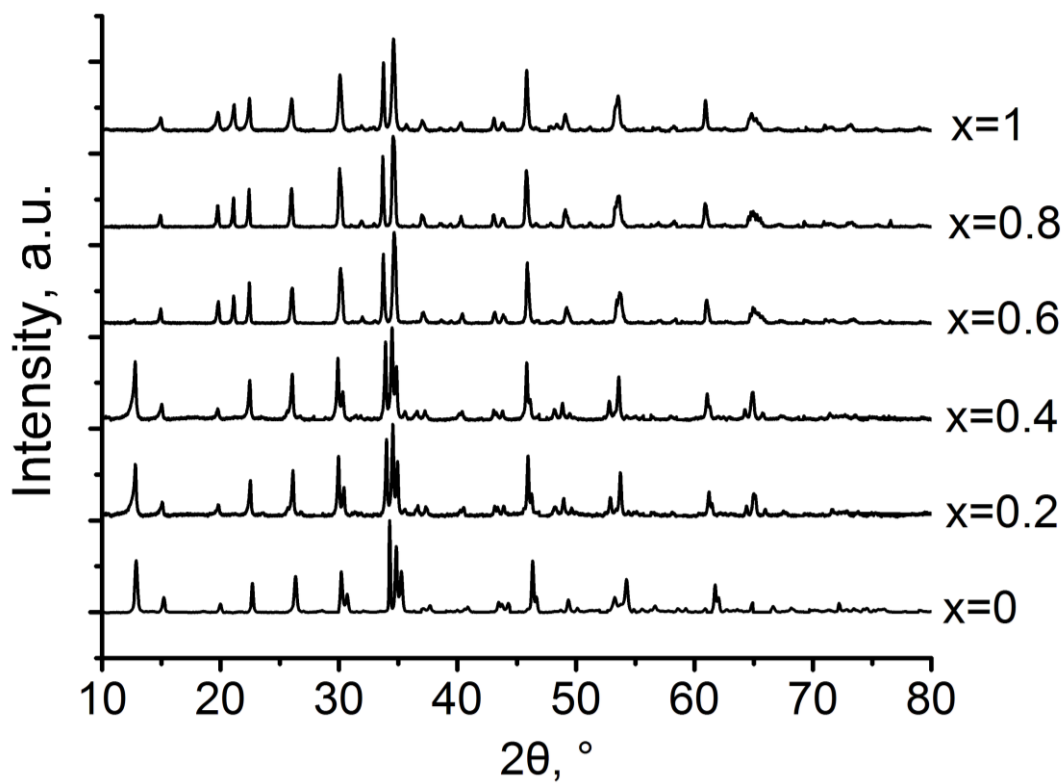
Table S6. Unit cell parameters for compounds with formula $(Na,Li)_{2-x}FePO_4F$ and $Na_{2-x}CoPO_4F$ refined by Rietveld method along with the R-factors of the refinements. Adapted with permission from "The Role of Semilabile Oxygen Atoms for Intercalation Chemistry of the Metal-Ion Battery Polyanion Cathodes" // I. V. Tereshchenko et al., J. Am. Chem. Soc. 140 (11), p. 3994–4003 (2018). Copyright 2018 American Chemical Society. Available from https://pubs.acs.org/articlesonrequest/AOR-YJh64uPKIstIQxXrxm5f.

X in XPO_4F	Na_2Fe	$Na_{1.55}Fe$	NaFe	$Li_{0.88}Na_{0.73}Fe$	$Li_{0.72}Na_{0.28}Fe$
Space group	Pbcn	$P2_1/b$	Pbcn		
a, Å	5.2344(2)	5.2039(4)	5.1288(4)	5.0137(4)	4.9714(5)
b, Å	13.8443(5)	13.912(1)	14.085(1)	13.904(1)	13.971(2)
c, Å	11.7757(4)	11.5377(8)	11.4041(8)	11.1839(7)	11.047(1)
α, °	90	91.275(3)	90		
V, Å^3	853.3(1)	835.1(1)	823.8(1)	779.6(1)	767.3(2)
Rp	0.160	0.019	0.030	0.022	0.021
Rwp	0.122	0.026	0.043	0.030	0.031
Rf	0.770	0.040	0.032	0.045	0.058
GOF	1.6	2.6	3	4.3	3

X in XPO_4F	Na_2Co	$Na_{1.44}Co$	NaCo
Space group	Pbcn	$P2_1/b$	Pbcn
a, Å	5.2416(7)	5.2017(5)	5.1021(5)
b, Å	13.779(2)	13.850(3)	14.026(4)
c, Å	11.688(2)	11.408(3)	11.232(4)
α, °	90	90.89(3)	90
V, Å^3	844.2(2)	821.8(3)	803.8(4)
Rp	0.208	0.213	0.267
Rwp	0.117	0.140	0.178
Rf	0.100	0.177	0.230
GOF	0.8	0.6	0.9

Figure S6. ^{57}Fe Mössbauer spectra of the Na$_2$FePO$_4$F electrodes half-charged in the Na-ion (**A**) and Li-ion (**B**) half-cells (^{57}Fe). The Fe^{3+} and Fe^{2+} doublets are marked with red and green, respectively. Reprinted with permission from "The Role of Semilabile Oxygen Atoms for Intercalation Chemistry of the Metal-Ion Battery Polyanion Cathodes" // I. V. Tereshchenko et al., J. Am. Chem. Soc. 140 (11), p. 3994–4003 (2018). Copyright 2018 American Chemical Society. Available from https://pubs.acs.org/articlesonrequest/AOR-YJh64uPKIstIQxXrxm5f.
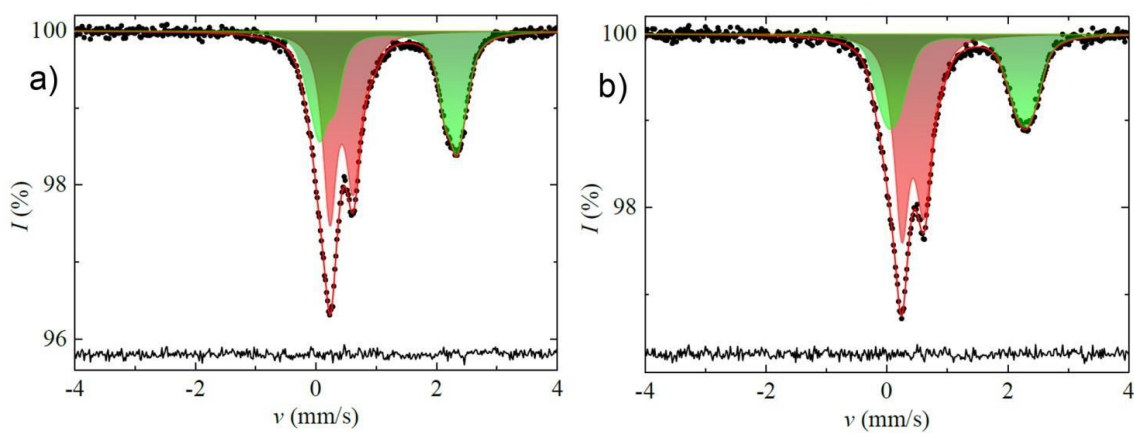
Table S7. Parameters of the ^{57}Fe Mössbauer spectra for the Na_2FePO_4F electrodes half-charged in the Na-ion and Li-ion cells (δ – isomer shift, Δ – quadrupole splitting, W – linewidth, I – relative peak area). Reprinted with permission from "The Role of Semilabile Oxygen Atoms for Intercalation Chemistry of the Metal-Ion Battery Polyanion Cathodes" // I. V. Tereshchenko et al., J. Am. Chem. Soc. 140 (11), p. 3994–4003 (2018). Copyright 2018 American Chemical Society. Available from https://pubs.acs.org/articlesonrequest/AOR-YJh64uPKIstIQxXrxm5f.

Sample		δ_{Fe}, mm/s	Δ_{Fe}, mm/s	W, mm/s	I, %
Half-charged in the Na-ion cell	Fe^{3+}	0.434(2)	0.417(4)	0.244(6)	48.6(3)
	Fe^{2+}	1.202(2)	2.183(4)	0.244(6)	51.4(3)
Half-charged in the Li-ion cell	Fe^{3+}	0.437(2)	0.395(5)	0.250(7)	54.7(3)
	Fe^{2+}	1.171(3)	2.201(6)	0.250(7)	45.3(3)

Table S8. Atomic coordinates and occupancies of Na_2CoPO_4F refined with isotropic thermal parameter U=0.005(1) $Å^2$ refined using PXRD data from Figure S3. Number of reflections – 303, number of points/parameters – 19000/40, Rp=0.208, Rwp=0.117, Rf=0.100, GOF=0.77.

Label	Position	x/a	y/b	z/c	Occupancy	BVS
Na1		0.249(2)	0.2420(6)	0.3229(6)		1.13(2)
Na2		0.243(1)	0.1268(6)	0.0842(5)		1.21(2)
Co		0.2546(6)	0.0104(3)	0.3266(3)		1.95(3)
P1	8d	0.295(1)	0.3821(5)	0.0866(5)		4.87(8)
O1		0.232(2)	0.3840(9)	-0.043(1)	1	1.96(5)
O2		0.216(2)	0.2832(8)	0.1374(8)		2.01(5)
O3		0.147(2)	0.4640(8)	0.148(1)		1.90(4)
O4		0.584(2)	0.3974(9)	0.1039(9)		2.07(4)
F1	4c	0	0.101(1)	0.25		1.24(2)
F2		0.5	0.108(1)	0.25		1.21(3)

Figure S7. SXPD pattern and Rietveld refinement profile of $Na_{1.55}FePO_4F$ with space group $P2_1/b$ ($\lambda=0.7121$Å). $2\theta=2.6\div41.2°$, number of reflections of $Na_{1.55}FePO_4F$ – 988; number of refined parameters – 40. Adapted with permission from "The Role of Semilabile Oxygen Atoms for Intercalation Chemistry of the Metal-Ion Battery Polyanion Cathodes" // I. V. Tereshchenko et al., J. Am. Chem. Soc. 140 (11), p. 3994–4003 (2018). Copyright 2018 American Chemical Society. Available from https://pubs.acs.org/articlesonrequest/AOR-YJh64uPKIstIQxXrxm5f.
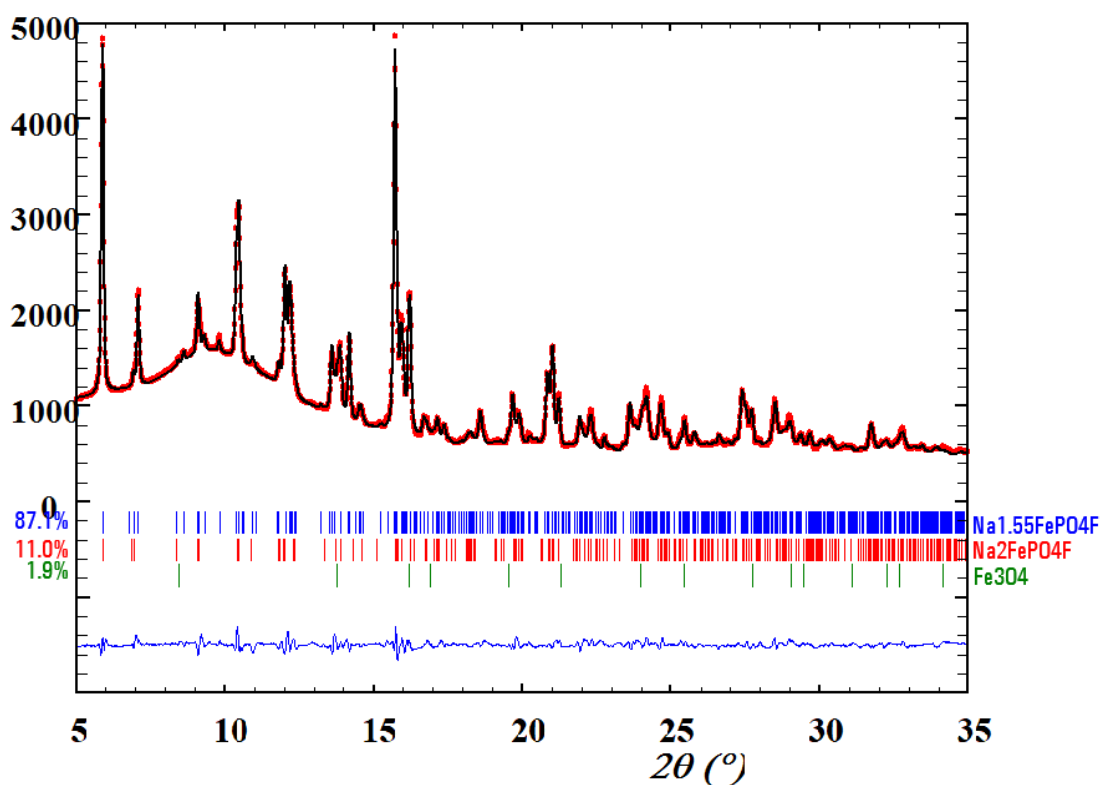
Figure S8. SXPD pattern and Rietveld refinement profile of $NaFePO_4F$ with space group *Pbcn* (λ=0.7121Å). 2θ=2.6÷41.2°, number of reflections of $NaFePO_4F$ – 358; number of refined parameters – 16. Adapted with permission from "The Role of Semilabile Oxygen Atoms for Intercalation Chemistry of the Metal-Ion Battery Polyanion Cathodes" // I. V. Tereshchenko et al., J. Am. Chem. Soc. 140 (11), p. 3994–4003 (2018). Copyright 2018 American Chemical Society. Available from https://pubs.acs.org/articlesonrequest/AOR-YJh64uPKIstIQxXrxm5f.
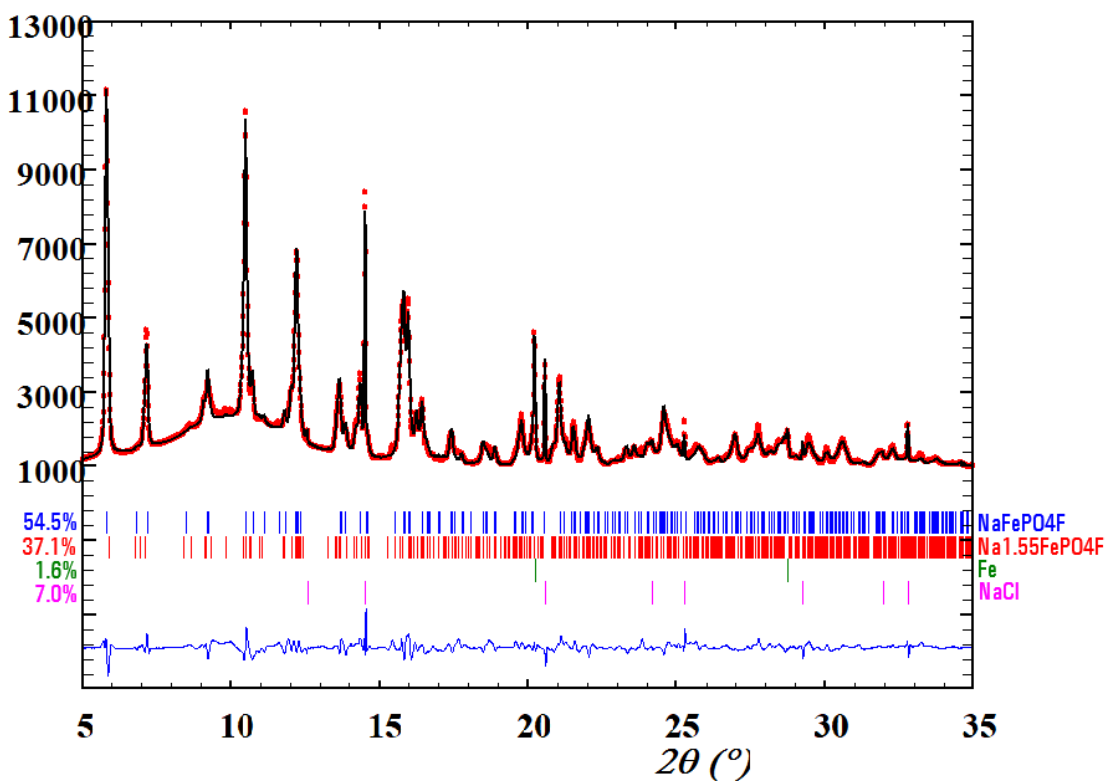
Table S9. Atomic coordinates and occupancies of $Na_{1.55}FePO_4F$ refined with isotropic thermal parameter $U=0.016(1)$ $Å^2$ using SXPD data from Figure S7. Reprinted with permission from "The Role of Semilabile Oxygen Atoms for Intercalation Chemistry of the Metal-Ion Battery Polyanion Cathodes" // I. V. Tereshchenko et al., J. Am. Chem. Soc. 140 (11), p. 3994–4003 (2018). Copyright 2018 American Chemical Society. Available from https://pubs.acs.org/articlesonrequest/AOR-YJh64uPKIstIQxXrxm5f.

Label		x/a	y/b	z/c	Multiplicity	Occupancy
$A1_1$	Na	0.267(3)	0.2389(8)	0.3079(9)	4	1
$A1_2$		0.743(4)	0.2448(7)	0.1309(7)		0.91(1)
$A2_1$		0.150(9)	0.128(4)	0.102(4)		0.18(1)
$A2_2$		0.739(4)	0.1423(8)	0.4164(8)		1
Fe1		0.2337(15)	0.0096(3)	0.3316(3)		1
Fe2		0.7641(16)	0.0146(3)	0.1765(4)		1
P1		0.216(2)	0.3832(4)	0.0839(5)		1
P2		0.803(2)	0.3819(4)	0.4064(5)		1
O1		0.261(4)	0.4000(7)	0.9536(8)		1
O2		0.283(4)	0.2781(7)	0.1115(8)		1
O3		0.389(2)	0.452(1)	0.156(1)		1
O4		0.932(2)	0.403(1)	0.114(1)		1
O5		0.729(3)	0.3818(8)	0.5361(9)		1
O6		0.709(3)	0.2876(8)	0.3472(9)		1
O7		0.675(2)	0.4684(9)	0.348(1)		1
O8		0.097(2)	0.3898(9)	0.394(1)		1
F1		0.984(4)	0.1163(13)	0.254(2)		1
F2		0.501(4)	0.1032(11)	0.244(2)		1

Table S10. Atomic coordinates and occupancies of NaFePO$_4$F refined with isotropic thermal parameter U=0.006(1) Å^2 using SXPD data from Figure S8. Reprinted with permission from "The Role of Semilabile Oxygen Atoms for Intercalation Chemistry of the Metal-Ion Battery Polyanion Cathodes" // I. V. Tereshchenko et al., J. Am. Chem. Soc. 140 (11), p. 3994–4003 (2018). Copyright 2018 American Chemical Society. Available from https://pubs.acs.org/articlesonrequest/AOR-YJh64uPKIstIQxXrxm5f.

Label		x/a	y/b	z/c	Multiplicity	Occupancy
A1	Na	0.252(3)	0.2508(6)	0.3425(7)	8	1
Fe1		0.229(1)	0.0198(2)	0.3314(3)		
P1		0.199(1)	0.3865(3)	0.0928(3)		
O1		0.244(3)	0.3884(7)	0.9590(7)		
O2		0.277(3)	0.2882(7)	0.1413(7)		
O3		0.366(2)	0.4642(9)	0.1518(9)		
O4		0.908(2)	0.4081(9)	0.1193(9)		
F1		0	0.102(2)	0.25	4	
F2		0.5	0.091(2)	0.25		

Table S11. Main interatomic distances for $Na_{1.55}FePO_4F$. Adapted with permission from "The Role of Semilabile Oxygen Atoms for Intercalation Chemistry of the Metal-Ion Battery Polyanion Cathodes" // I. V. Tereshchenko et al., J. Am. Chem. Soc. 140 (11), p. 3994–4003 (2018). Copyright 2018 American Chemical Society. Available from https://pubs.acs.org/articlesonrequest/AOR-YJh64uPKIstIQxXrxm5f.

$A1_1$-O2	2.34(1)	$A2_1$-O1	2.16(5)	Fe1-O3	2.25(1)
$A1_1$-O5	2.50(2)	$A2_1$-O2	2.20(6)	Fe1-O5	2.12(1)
$A1_1$-O6	2.44(2)	$A2_1$-O3	2.56(6)	Fe1-O7	2.21(1)
$A1_1$-O8	2.47(2)	$A2_1$-O4	2.92(5)	Fe1-O8	2.03(1)
$A1_1$-F1	2.33(2)	$A2_1$-F1	1.97(6)	Fe1-F1	2.18(2)
$A1_1$-F2	2.70(2)	$A2_1$-F2	2.49(5)	Fe1-F2	2.17(2)
BVS	0.98(2)	*BVS*	1.37(10)	*BVS*	1.86(3)
$A1_2$-O1	2.22(1)	$A2_2$-O5	2.63(2)	Fe2-O1	1.93(1)
$A1_2$-O2	2.45(3)	$A2_2$-O5	2.73(2)	Fe2-O3	2.02(1)
$A1_2$-O2	2.86(3)	$A2_2$-O6	2.20(2)	Fe2-O4	1.98(2)
$A1_2$-O2	2.82(1)	$A2_2$-O7	2.57(2)	Fe2-O7	2.12(1)
$A1_2$-O4	2.42(2)	$A2_2$-O8	2.36(2)	Fe2-F1	2.01(2)
$A1_2$-O6	2.56(1)	$A2_2$-F1	2.29(3)	Fe2-F2	1.99(2)
$A1_2$-F1	2.63(3)	$A2_2$-F2	2.39(2)	*BVS*	2.78(5)
$A1_2$-F2	2.70(2)	*BVS*	1.11(2)		
BVS	0.97(2)			P – O	1.544(1)

Table S12. Main interatomic distances for $NaFePO_4F$. Adapted with permission from "The Role of Semilabile Oxygen Atoms for Intercalation Chemistry of the Metal-Ion Battery Polyanion Cathodes" // I. V. Tereshchenko et al., J. Am. Chem. Soc. 140 (11), p. 3994–4003 (2018). Copyright 2018 American Chemical Society. Available from https://pubs.acs.org/articlesonrequest/AOR-YJh64uPKIstIQxXrxm5f.

A1-O1	2.37(1)	Fe1-O1	1.951(9)
A1-O2	2.36(1)	Fe1-O3	2.03(1)
A1-O2	2.48(2)	Fe1-O3	2.25(1)
A1-O2	2.77(2)	Fe1-O4	1.94(1)
A1-O4	2.36(2)	Fe1-F1	1.90(2)
A1-F1	2.68(2)	Fe1-F2	1.95(1)
A1-F2	2.79(2)	*BVS*	3.03(4)
BVS	0.90(2)	P – O	1.544(9)

Table S13. EDX data for the Na_2FePO_4F electrodes at different SOCs (C/10 current) and after ion exchange of sodium for lithium. Reprinted with permission from "The Role of Semilabile Oxygen Atoms for Intercalation Chemistry of the Metal-Ion Battery Polyanion Cathodes" // I. V. Tereshchenko et al., J. Am. Chem. Soc. 140 (11), p. 3994–4003 (2018). Copyright 2018 American Chemical Society. Available from https://pubs.acs.org/articlesonrequest/AOR-YJh64uPKIstIQxXrxm5f.

Sample	Na/(Fe+P) expected from the charge passed	Na/(Fe+P) expected from EDX, ±0.05
Initial	1	1.04
Half-charged in Li-ion cell at -10°C	0.75	0.76
Half-charged in Li-ion cell at room	0.75	0.50
Half-charged in Li-ion cell at 75°C	0.75	0.32
Half-charged in Na-ion cell	0.75	0.77
Charged in Li-ion cell	0.50	0.09
Charged in Na-ion cell	0.50	0.67*
Soaked in 30-fold excess of Li-ion electrolyte for 10 h		0.71
Soaked in 30-fold excess of Li-ion electrolyte for 48 h		0.39
Soaked in 30-fold excess of Li-ion electrolyte for 168 h		0.21

*some Na excess with respect to expected value may appear due to incomplete charge of the electrode

Figure S9. SXPD pattern and Rietveld refinement profile of $Li_{0.88}Na_{0.73}FePO_4F$ with space group *Pbcn* (λ=0.7121Å). 2θ=2.7÷41.2°, number of reflections of $NaFePO_4F$ – 508; number of refined parameters – 21. Adapted with permission from "The Role of Semilabile Oxygen Atoms for Intercalation Chemistry of the Metal-Ion Battery Polyanion Cathodes" // I. V. Tereshchenko et al., J. Am. Chem. Soc. 140 (11), p. 3994–4003 (2018). Copyright 2018 American Chemical Society. Available from https://pubs.acs.org/articlesonrequest/AOR-YJh64uPKIstIQxXrxm5f.
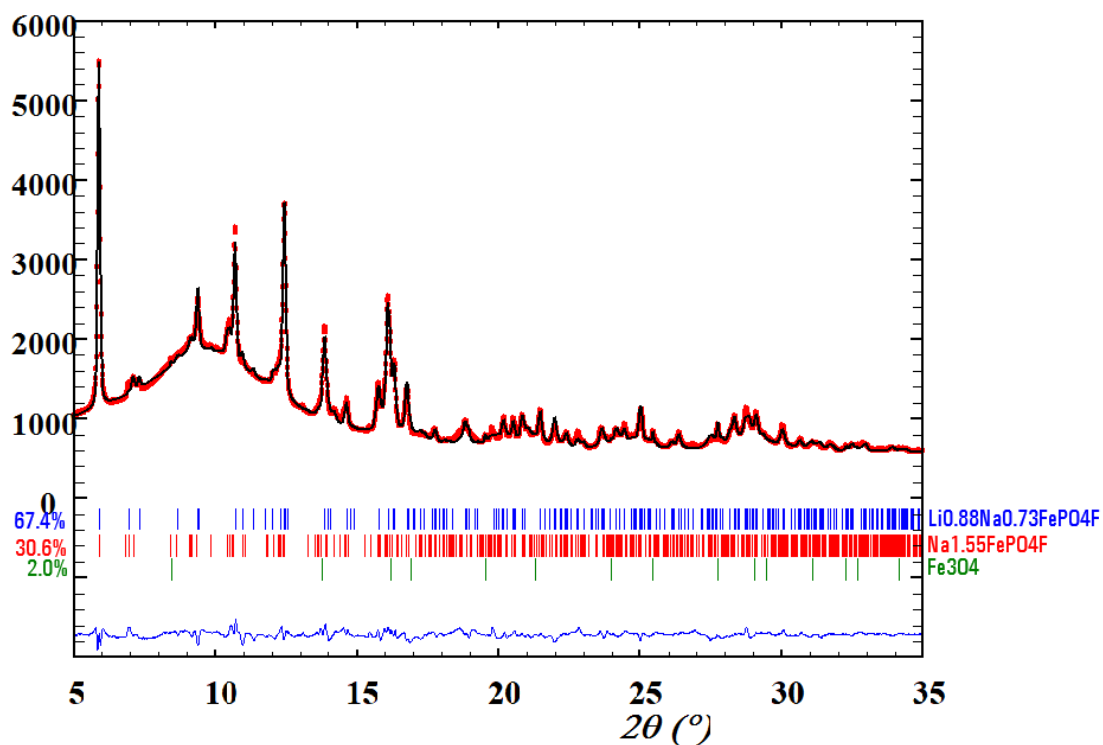
Figure S10. SXPD pattern and Rietveld refinement profile of $Li_{0.72}Na_{0.28}FePO_4F$ with space group *Pbcn* (λ=0.7121Å). 2θ=2.3÷41.4°, number of reflections of $NaFePO_4F$ – 510; number of refined parameters – 17. Adapted with permission from "The Role of Semilabile Oxygen Atoms for Intercalation Chemistry of the Metal-Ion Battery Polyanion Cathodes" // I. V. Tereshchenko et al., J. Am. Chem. Soc. 140 (11), p. 3994–4003 (2018). Copyright 2018 American Chemical Society. Available from https://pubs.acs.org/articlesonrequest/AOR-YJh64uPKIstIQxXrxm5f.
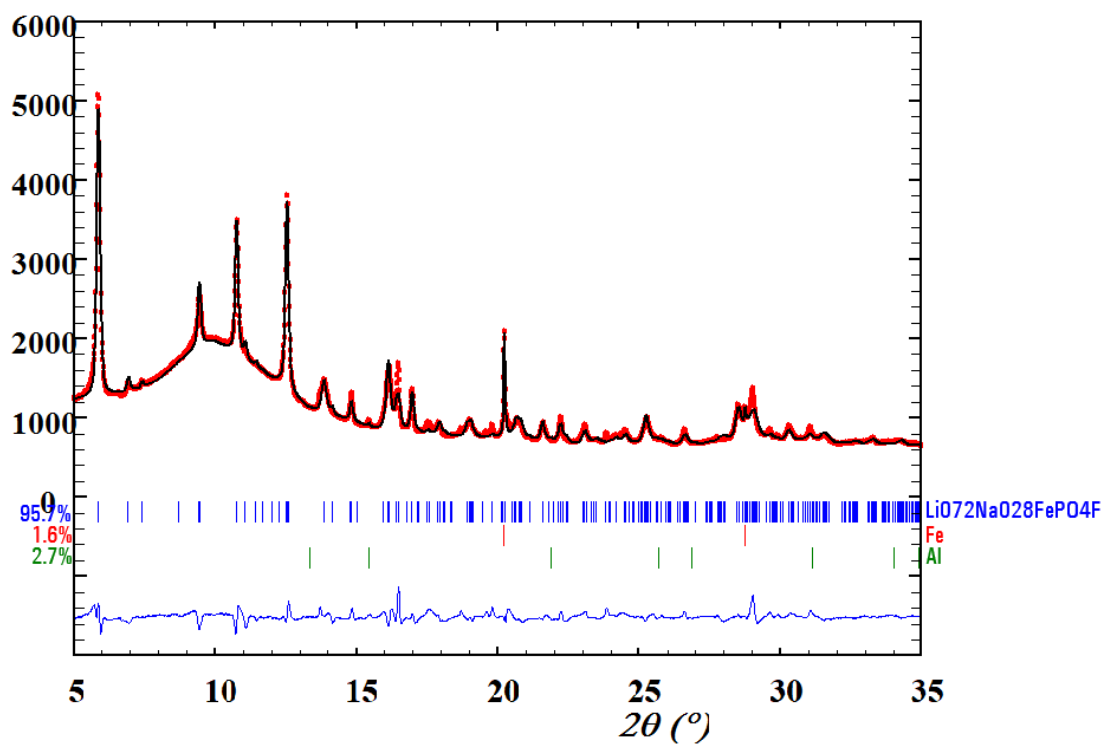
Table S14. Atomic coordinates and occupancies of $Li_{0.88}Na_{0.73}FePO_4F$ refined with isotropic thermal parameter U=0.008(1) $Å^2$ using SXPD data from Figure S9. Reprinted with permission from "The Role of Semilabile Oxygen Atoms for Intercalation Chemistry of the Metal-Ion Battery Polyanion Cathodes" // I. V. Tereshchenko et al., J. Am. Chem. Soc. 140 (11), p. 3994–4003 (2018). Copyright 2018 American Chemical Society. Available from https://pubs.acs.org/articlesonrequest/AOR-YJh64uPKIstIQxXrxm5f.

Label		x/a	y/b	z/c	Multiplicity	Occupancy
A1	Na	0.311(3)	0.245(2)	0.333(1)	8	0.61(1)
A2		0.234(10)	0.137(2)	0.072(3)		0.12(1)
	Li					0.88(1)
Fe1		0.244(2)	0.0070(4)	0.3352(3)		1
P1		0.234(1)	0.3750(6)	0.0778(6)		
O1		0.358(3)	0.3849(6)	0.9519(8)		
O2		0.244(3)	0.2686(6)	0.1175(8)		
O3		0.393(2)	0.4372(9)	0.1672(9)		
O4		0.941(2)	0.4093(9)	0.0745(9)		
F1		0	0.085(2)	0.25	4	
F2		0.5	0.088(2)	0.25		

Table S15. Atomic coordinates and occupancies of $Li_{0.72}Na_{0.28}FePO_4F$ refined with isotropic thermal parameter U=0.002(1) $Å^2$ using SXPD data from Figure S10. Reprinted with permission from "The Role of Semilabile Oxygen Atoms for Intercalation Chemistry of the Metal-Ion Battery Polyanion Cathodes" // I. V. Tereshchenko et al., J. Am. Chem. Soc. 140 (11), p. 3994–4003 (2018). Copyright 2018 American Chemical Society. Available from https://pubs.acs.org/articlesonrequest/AOR-YJh64uPKIstIQxXrxm5f.

Label		x/a	y/b	z/c	Multiplicity	Occupancy
A1	Na	0.272(7)	0.254(3)	0.338(2)		0.28
	Li					0.72
Fe1		0.245(2)	0.0036(6)	0.3366(3)	8	1
P1		0.236(1)	0.3783(3)	0.0769(5)		
O1		0.362(3)	0.3950(6)	0.9511(8)		
O2		0.239(3)	0.2702(6)	0.1061(8)		
O3		0.398(2)	0.433(1)	0.1736(8)		
O4		0.942(2)	0.415(1)	0.0768(8)		
F1		0	0.078(3)	0.25	4	
F2		0.5	0.074(3)	0.25		

Table S16. Main interatomic distances for $Li_{0.88}Na_{0.73}FePO_4F$. Adapted with permission from "The Role of Semilabile Oxygen Atoms for Intercalation Chemistry of the Metal-Ion Battery Polyanion Cathodes" // I. V. Tereshchenko et al., J. Am. Chem. Soc. 140 (11), p. 3994–4003 (2018). Copyright 2018 American Chemical Society. Available from https://pubs.acs.org/articlesonrequest/AOR-YJh64uPKIstIQxXrxm5f.

A1-O1	2.39(2)	Fe1-O1	2.06(1)
A1-O2	2.32(2)	Fe1-O3	2.01(1)
A1-O2	2.46(2)	Fe1-O3	2.22(1)
A1-O2	2.85(2)	Fe1-O4	1.96(1)
A1-O4	2.81(2)	Fe1-F1	1.89(2)
A1-F1	2.87(3)	Fe1-F2	1.96(2)
A1-F2	2.55(3)	*BVS*	2.74(4)
BVS	0.79(2)	P – O	1.544(1)
A2-O1	1.93(5)		
A2-O2	1.90(3)		
A2-O4	2.05(4)		
A2-F1	2.42(4)		
A2-F2	2.49(4)		
BVS(Na)	2.01(11)		
BVS(Li)	0.88(3)		

Table S17. Main interatomic distances for $Li_{0.72}Na_{0.28}FePO_4F$. Adapted with permission from "The Role of Semilabile Oxygen Atoms for Intercalation Chemistry of the Metal-Ion Battery Polyanion Cathodes" // I. V. Tereshchenko et al., J. Am. Chem. Soc. 140 (11), p. 3994–4003 (2018). Copyright 2018 American Chemical Society. Available from

A1-O1	2.52(4)	Fe1-O1	1.97(1)
A1-O2	2.58(2)	Fe1-O3	1.99(1)
A1-O2	2.98(2)	Fe1-O3	2.17(1)
A1-O2	2.63(4)	Fe1-O4	1.85(1)
A1-O2	2.51(4)	Fe1-F1	1.87(3)
A1-O3	2.99(5)	Fe1-F2	1.87(2)
A1-O4	2.66(5)	*BVS*	3.46(7)
A1-F1	2.97(6)	P – O	1.54(1)
A1-F2	2.93(6)		
BVS(Na)	0.68(3)		
BVS(Li)	0.62(1)		

Figure S11. SXPD pattern and Rietveld refinement profile of the half-charged state of Na_2CoPO_4F made *operando* (λ=0.68987Å); area with 2θ=7÷7.5° was excluded because of a detector defect; moment of acquisition – 4.47 hours; number of reflections – 1108, number of points/parameters – 2891/67, Rp=0.213, Rwp=0.140, Rf=0.177, GOF=0.60.
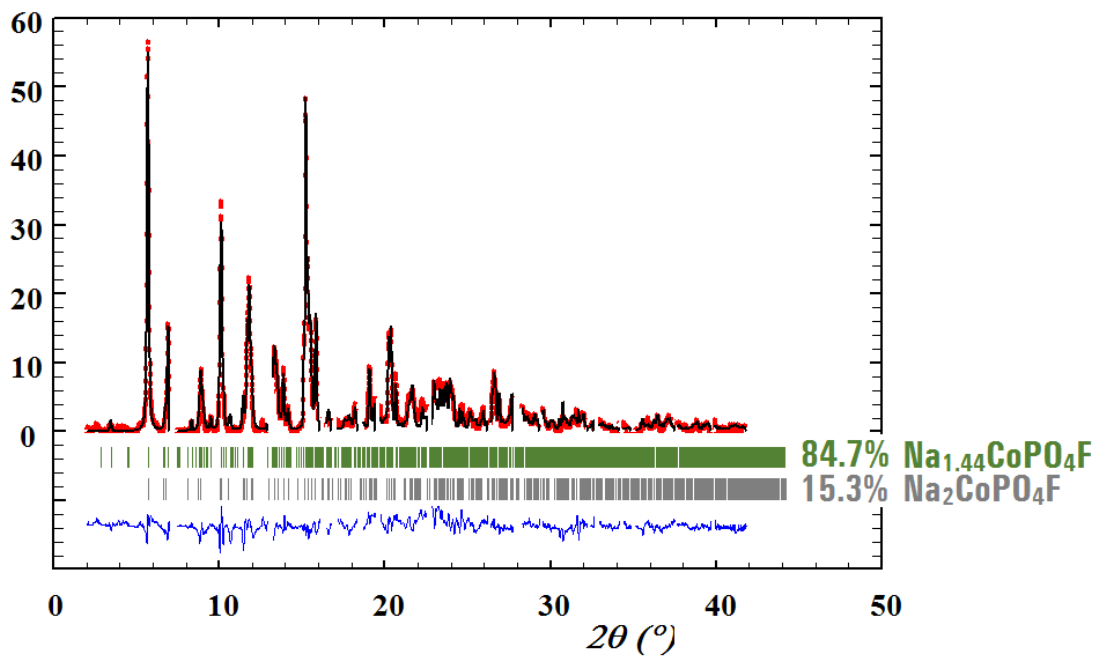
Figure S12. SXPD pattern and Rietveld refinement profile of the charged state of Na_2CoPO_4F/C made *operando* (λ=0.68987Å); area with 2θ=7÷7.5° was excluded because of a detector defect; moment of acquisition – 7.42 hours; number of reflections – 543, number of points/parameters – 2891/37, Rp=0.267, Rwp=0.178, Rf=0.230, GOF=0.88.

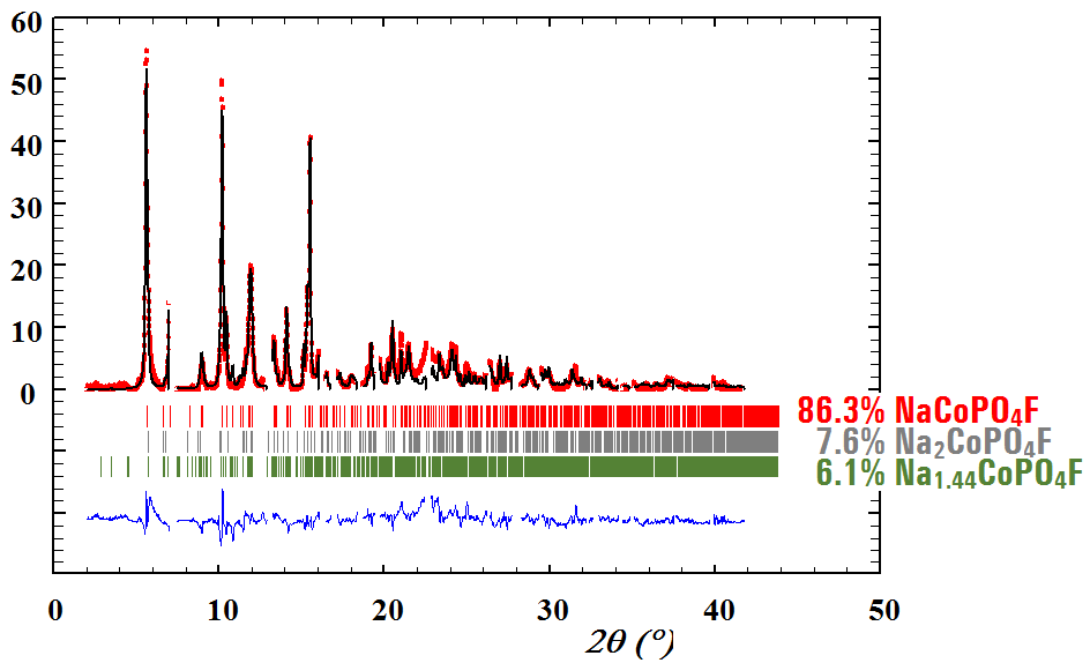Table S18. Atomic coordinates and occupancies of $Na_{1.44}CoPO_4F$ refined with isotropic thermal parameter $U=0.024(1)$ $Å^2$ using SXPD data from Figure S11.

Label	Position	x/a	y/b	z/c	Occupancy	BVS
$Na1_1$		0.219(4)	0.229(1)	0.301(2)	1	1.15(5)
$Na1_2$		0.724(4)	0.241(1)	0.128(1)		1.07(4)
$Na2_1$		0.249	0.128	0.085	0	1.26(1)
$Na2_2$		0.801(5)	0.131(2)	0.403(2)	0.87(2)	1.50(7)
Co1		0.290(2)	0.009(1)	0.331(1)		1.69(5)
Co2		0.738(2)	0.015(1)	0.182(1)		2.50(8)
P1		0.271(4)	0.384(1)	0.088(2)		4.9(2)
P2		0.697(3)	0.378(1)	0.413(1)		4.9(2)
$O1≡O1_1$	4e	0.230(7)	0.400(2)	0.955(3)		2.0(1)
$O2≡O2_1$		0.214(6)	0.277(2)	0.117(2)		1.8(1)
$O3≡O3_1$		0.552(5)	0.408(2)	0.120(3)	1	1.8(1)
$O4≡O4_1$		0.088(5)	0.450(2)	0.158(2)		1.9(1)
$O5≡O1_2$		0.811(6)	0.376 (2)	0.538(3)		1.8(1)
$O6≡O2_2$		0.762(8)	0.283(2)	0.348(2)		1.8(1)
$O7≡O3_2$		0.402(5)	0.390(2)	0.420(3)		1.9(1)
$O8≡O4_2$		0.812(5)	0.464(2)	0.346(2)		2.0(1)
F1		0.022(4)	0.089(2)	0.240(3)		1.17(5)
F2		0.512(5)	0.111(2)	0.249(3)		1.18(5)

Table S19. Atomic coordinates and occupancies of $NaCoPO_4F$ refined with isotropic thermal parameter $U=0.029(1)$ $Å^2$ using SXPD data from Figure S12.

Label	Position	x/a	y/b	z/c	Occupancy	BVS
Na1		0.255(2)	0.250(1)	0.343(1)		0.96(2)
Co		0.280(1)	0.0259(3)	0.3236(4)		2.39(5)
P1		0.298(2)	0.390(1)	0.091(1)		4.9(1)
O1	8d	0.242(4)	0.407(1)	0.957(1)		2.04(7)
O2		0.239(5)	0.285(1)	0.123(1)	1	1.58(7)
O3		0.122(3)	0.457(1)	0.166(2)		1.90(7)
O4		0.588(3)	0.412(1)	0.117(1)		1.78(6)
F1	4c	0	0.102(2)	0.25		0.92(3)
F2		0.5	0.142(2)	0.25		0.94(3)

Figure S13. (**A**) Overall *operando* SXPD picture for $2\theta=5\div27°$ after background subtraction and exclusion of aluminum reflections and detector defects (red regions). Intensity is normalized so that black and white colors correspond to the intensity maximum and minimum over the whole picture; (**B**) contour map for $2\theta=5\div27°$ showing absolute difference between theoretical Rietveld fit and the experimental SXPD data normalized by the intensity maximum of the given pattern.
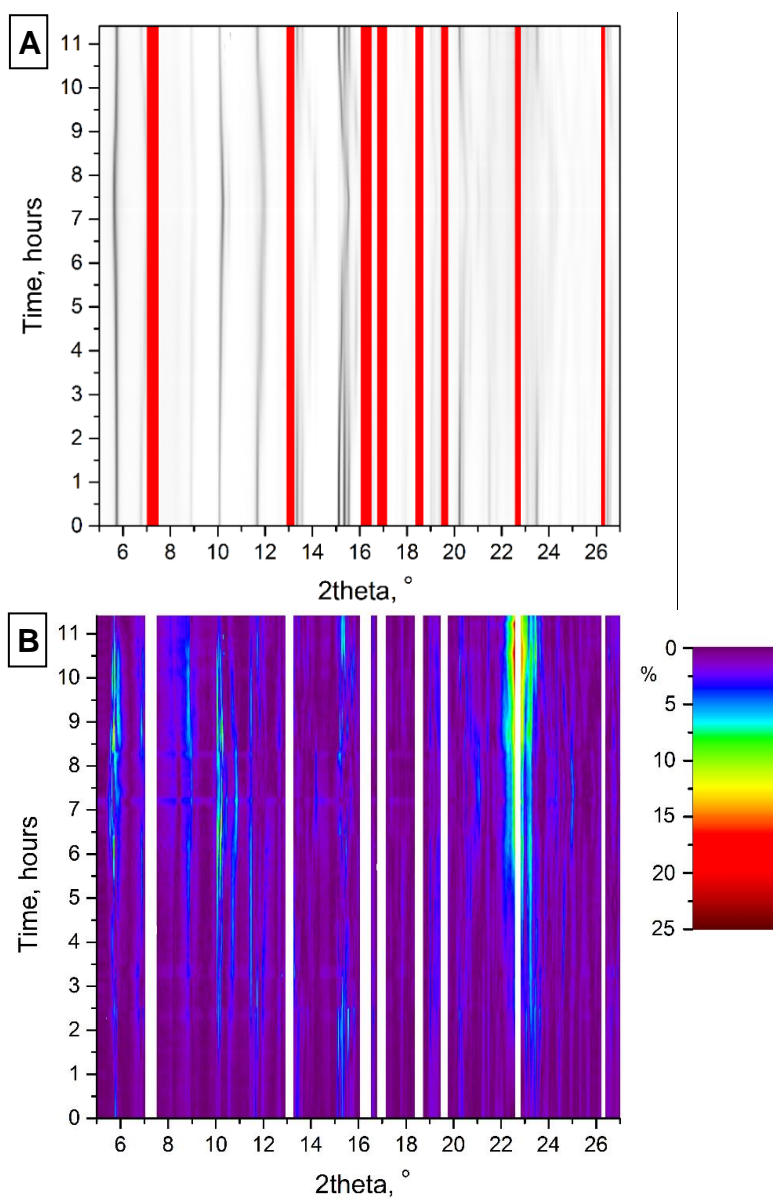
Figure S14. PXRD pattern and Rietveld refinement profile of the initial powder of $K_6(VO)_2(V_2O_3)_2(PO_4)_4(P_2O_7)$ (λ_1=1.5406Å, λ_2=1.5444Å). The Bragg reflection positions for the main phase $K_6(VO)_2(V_2O_3)_2(PO_4)_4(P_2O_7)$ (1) and the admixture phases β-$K_2(VO)_3(P_2O_7)_2$ (2) and $K_2VOP_2O_7$ (3) are marked. Reprinted from "Reversible electrochemical potassium deintercalation from >4 V positive electrode material $K_6(VO)_2(V_2O_3)_2(PO_4)_4(P_2O_7)$" // I. V. Tereshchenko, D. A. Aksyonov, A. Zhugayevych, E. V. Antipov and A. M. Abakumov; Solid State Ionics 357, p. 115468. Copyright 2020, with permission from Elsevier. Available from https://www.sciencedirect.com/science/article/abs/pii/S0167273820305221.
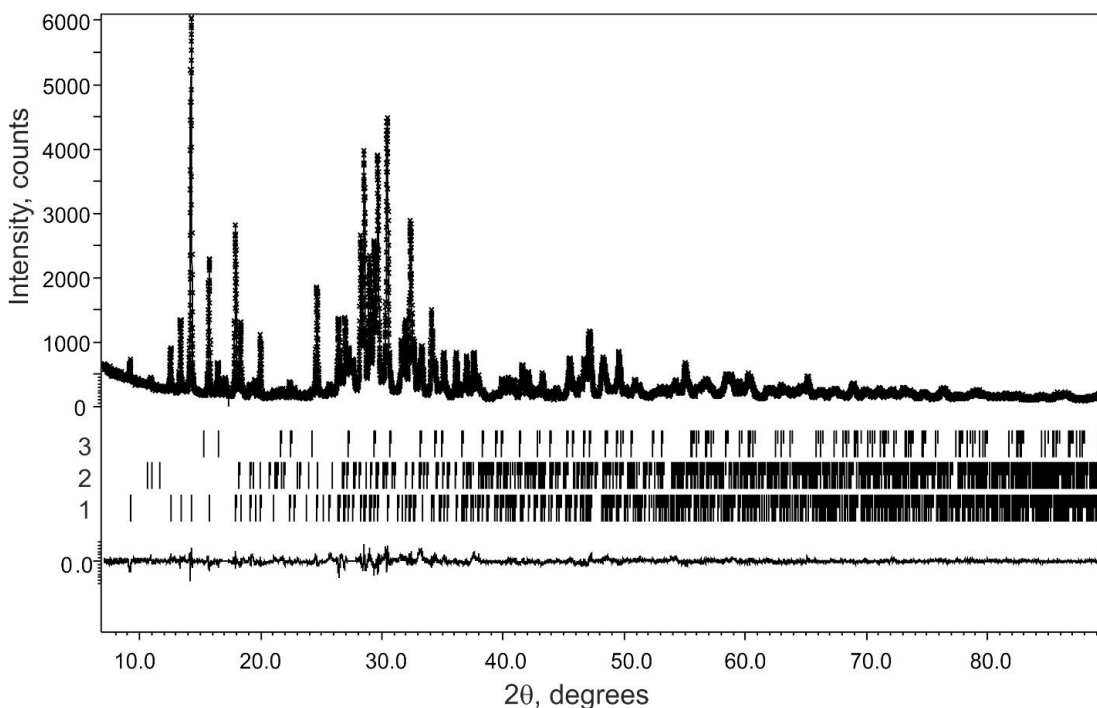
Table S20. Atomic coordinates and occupancies of the initial state of $K_6(VO)_2(V_2O_3)_2(PO_4)_4(P_2O_7)$ with isotropic thermal parameter U=0.0080(4) Å^2. Adapted from "Reversible electrochemical potassium deintercalation from >4 V positive electrode material $K_6(VO)_2(V_2O_3)_2(PO_4)_4(P_2O_7)$" // I. V. Tereshchenko, D. A. Aksyonov, A. Zhugayevych, E. V. Antipov and A. M. Abakumov; Solid State Ionics 357, p. 115468. Copyright 2020, with permission from Elsevier. Available from https://www.sciencedirect.com/science/article/abs/pii/S0167273820305221.

Label	Position	x/a	y/b	z/c	Occupancy
K1	8d	0.0990(3)	0.0088(2)	0.3350(1)	0.990(2)
K2	4c	0.1208(4)	0.25	0.5077(2)	0.974(3)
V1	8d	0.1592(2)	0.1252(1)	0.0789(1)	1
V2	4c	0.2420(4)	0.25	0.7600(2)	1
P1	8d	0.0387(2)	0.5986(1)	0.1190(1)	1
P2	4c	0.3686(4)	0.25	0.2435(2)	0.5
P3	4c	0.2809(6)	0.25	0.2639(2)	0.5
O1	4c	0.460(1)	0.25	0.8047(5)	1
O2	8d	0.3294(8)	0.0625(4)	0.0323(4)	1
O3	4c	0.2256(9)	0.25	0.0342(5)	1
O4	4c	0.060(2)	0.25	0.317(1)	0.5
O5	8d	0.2140(5)	0.6472(3)	0.1643(2)	1
O6	8d	0.0480(5)	0.6127(3)	0.0126(2)	1
O7	8d	0.0360(5)	0.4869(2)	0.1421(3)	1
O8	8d	-0.1433(5)	0.6476(2)	0.1571(3)	1
O9	8d	0.2795(6)	0.1547(3)	0.2070(2)	1
O10	4c	0.4151(8)	0.25	0.3470(3)	1

Figure S15. The 1st GSCD curves obtained at 25°C with current density C/50 (red) and C/20 (light grey) and the ones obtained at 60°C with current density C/50 (black) and C/20 60°C (blue). Adapted from "Reversible electrochemical potassium deintercalation from >4 V positive electrode material $K_6(VO)_2(V_2O_3)_2(PO_4)_4(P_2O_7)$" // I. V. Tereshchenko, D. A. Aksyonov, A. Zhugayevych, E. V. Antipov and A. M. Abakumov; Solid State Ionics 357, p. 115468. Copyright 2020, with permission from Elsevier. Available from https://www.sciencedirect.com/science/article/abs/pii/S0167273820305221.
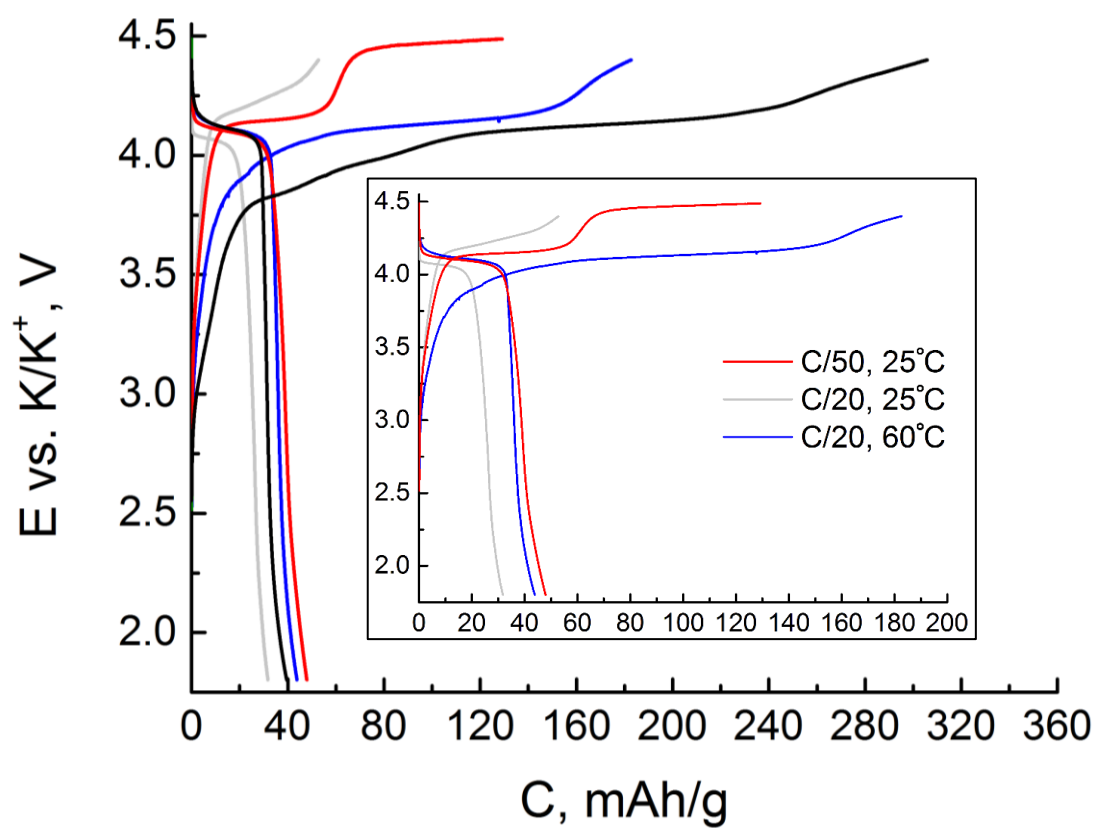
Figure S16. PXRD pattern and Rietveld refinement profile of $K_6(VO)_2(V_2O_3)_2(PO_4)_4(P_2O_7)$ after charge to 4.5V vs. K/K$^+$ at i=1.76 mA/g (λ_1=1.5406Å, λ_2=1.5444Å). The Bragg reflection positions for the main phase $K_6(VO)_2(V_2O_3)_2(PO_4)_4(P_2O_7)$ (1) and the admixture phase $K_2VOP_2O_7$ (2) are marked. Reprinted from "Reversible electrochemical potassium deintercalation from >4 V positive electrode material $K_6(VO)_2(V_2O_3)_2(PO_4)_4(P_2O_7)$" // I. V. Tereshchenko, D. A. Aksyonov, A. Zhugayevych, E. V. Antipov and A. M. Abakumov; Solid State Ionics 357, p. 115468. Copyright 2020, with permission from Elsevier. Available from https://www.sciencedirect.com/science/article/abs/pii/S0167273820305221.

Table S21. Atomic coordinates and occupancies of $K_6(VO)_2(V_2O_3)_2(PO_4)_4(P_2O_7)$ after charge to 4.5V vs. K/K^+ (i=1.76 mA/g) with isotropic thermal parameter U=0.0125(7) Å^2. Adapted from "Reversible electrochemical potassium deintercalation from >4 V positive electrode material $K_6(VO)_2(V_2O_3)_2(PO_4)_4(P_2O_7)$" // I. V. Tereshchenko, D. A. Aksyonov, A. Zhugayevych, E. V. Antipov and A. M. Abakumov; Solid State Ionics 357, p. 115468. Cop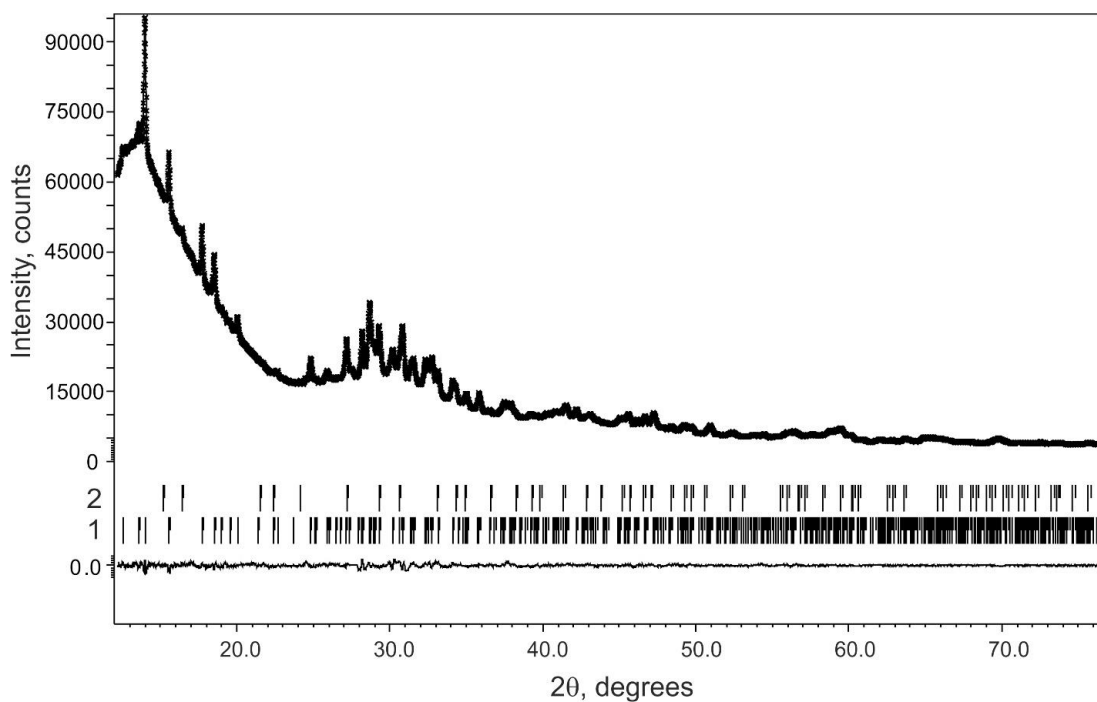yright 2020, with permission from Elsevier. Available from https://www.sciencedirect.com/science/article/abs/pii/S0167273820305221.

Label	Position	x/a	y/b	z/c	Occupancy
K1	8d	0.1080(8)	0.0295(4)	0.3382(4)	0.595(5)
K2	4c	0.130(1)	0.25	0.5035(6)	0.551(5)
V1	8d	0.1589(4)	0.1245(2)	0.0779(2)	1
V2	4c	0.2607(6)	0.25	0.7579(4)	1
P1	8d	0.0272(4)	0.6000(3)	0.1200(2)	1
P2	4c	0.3645(8)	0.25	0.2421(4)	0.5
P3	4c	0.2772(8)	0.25	0.2614(4)	0.5
O1	4c	0.464(2)	0.25	0.8007(8)	1
O2	8d	0.322(1)	0.0668(5)	0.0289(7)	1
O3	4c	0.237(2)	0.25	0.0394(9)	1
O4	4c	0.046(4)	0.25	0.309(2)	0.5
O5	8d	0.1990(9)	0.6512(6)	0.1646(3)	1
O6	8d	0.0288(9)	0.6188(6)	0.0135(3)	1
O7	8d	0.0333(9)	0.4850(4)	0.1393(5)	1
O8	8d	-0.1523(9)	0.6451(4)	0.1626(5)	1
O9	8d	0.279(1)	0.1525(5)	0.2042(4)	1
O10	4c	0.404(1)	0.25	0.3468(5)	1

Figure S17. PXRD pattern and Rietveld refinement profile of $K_6(VO)_2(V_2O_3)_2(PO_4)_4(P_2O_7)$ after charge to 4.4V vs. K/K$^+$ at i=1.76 mA/g (λ_1=1.5406Å, λ_2=1.5444Å). The Bragg reflection positions for the main phase $K_6(VO)_2(V_2O_3)_2(PO_4)_4(P_2O_7)$ (1) and the admixture phase $K_2VOP_2O_7$ (2) are marked. Reprinted from "Reversible electrochemical potassium deintercalation from >4 V positive electrode material $K_6(VO)_2(V_2O_3)_2(PO_4)_4(P_2O_7)$" // I. V. Tereshchenko, D. A. Aksyonov, A. Zhugayevych, E. V. Antipov and A. M. Abakumov; Solid State Ionics 357, p. 115468. Copyright 2020, with permission from Elsevier. Available from https://www.sciencedirect.com/science/article/abs/pii/S0167273820305221.

Table S22. Atomic coordinates and occupancies of $K_6(VO)_2(V_2O_3)_2(PO_4)_4(P_2O_7)$ after charge to 4.4V vs. K/K^+ (i=1.76 mA/g) with isotropic thermal parameter U=0.0137(9) $Å^2$ (a=7.1380(6) Å, b=13.0879(7) Å, c=14.1809(9) Å, V=1324.8(2) $Å^3$, Rp=0.032, Rwp=0.040, Rf=0.023). Adapted from "Reversible electrochemical potassium deintercalation from >4 V positive electrode material $K_6(VO)_2(V_2O_3)_2(PO_4)_4(P_2O_7)$" // I. V. Tereshchenko, D. A. Aksyonov, A. Zhugayevych, E. V. Antipov and A. M. Abakumov; Solid State Ionics 357, p. 115468. Copyright 2020, with permission from Elsevier. Available from

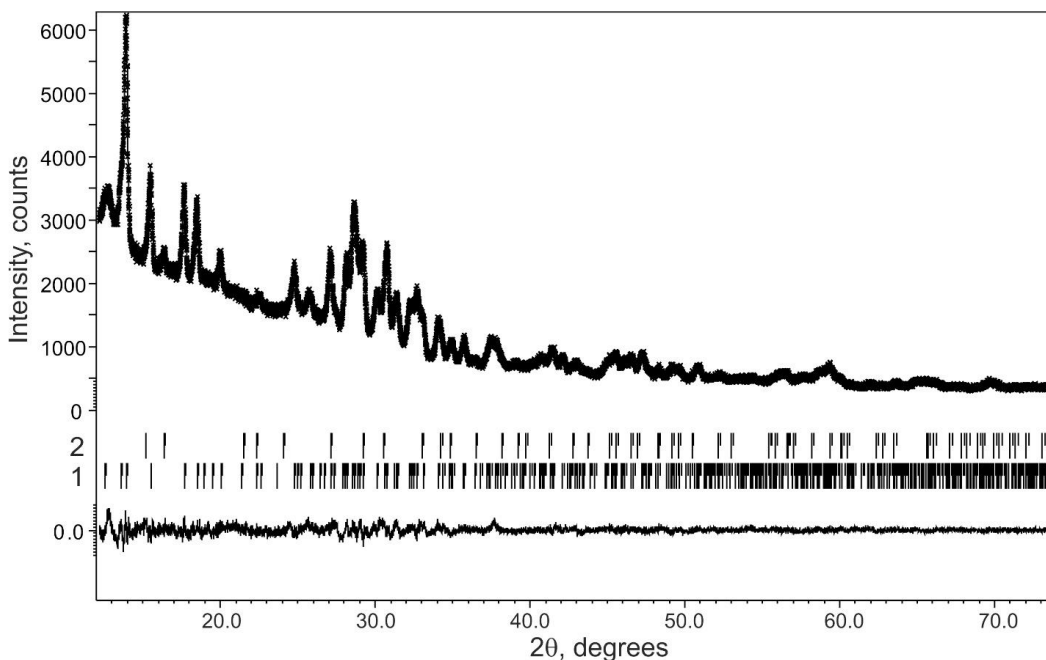| Label	Position	x/a	y/b	z/c	Occupancy
K1	8d	0.1030(9)	0.0233(5)	0.3389(4)	0.661(6)
K2	4c	0.125(1)	0.25	0.4985(7)	0.611(6)
V1	8d	0.1609(5)	0.1236(3)	0.0794(3)	1
V2	4c	0.2630(8)	0.25	0.7580(5)	1
P1	8d	0.0246(5)	0.5968(3)	0.1205(2)	1
P2	4c	0.378(1)	0.25	0.2409(5)	0.5
P3	4c	0.293(1)	0.25	0.2618(5)	0.5
O1	4c	0.489(2)	0.25	0.8061(9)	1
O2	8d	0.324(2)	0.0637(6)	0.0329(9)	1
O3	4c	0.220(2)	0.25	0.037(1)	1
O4	4c	0.095(5)	0.25	0.311(2)	0.5
O5	8d	0.198(1)	0.6486(8)	0.1624(4)	1
O6	8d	0.026(1)	0.6101(8)	0.0133(4)	1
O7	8d	0.027(1)	0.4829(5)	0.1447(6)	1
O8	8d	-0.152(1)	0.6455(5)	0.1615(6)	1
O9	8d	0.290(1)	0.1526(6)	0.2047(5)	1
O10	4c	0.426(2)	0.25	0.3447(6)	1

Figure S18. PXRD pattern and Rietveld of the powder of $K_6(VO)_2(V_2O_3)_2(PO_4)_4(P_2O_7)$ discharged to 1.8 V vs. K/K^+ at i=1.76mA/g (λ_1=1.5406Å, λ_2=1.5444Å); The Bragg reflection positions for the main phase $K_6(VO)_2(V_2O_3)_2(PO_4)_4(P_2O_7)$ (1) and the admixture phase $K_2VOP_2O_7$ (2) are marked. Reprinted from "Reversible electrochemical potassium deintercalation from >4 V positive electrode material $K_6(VO)_2(V_2O_3)_2(PO_4)_4(P_2O_7)$" // I. V. Tereshchenko, D. A. Aksyonov, A. Zhugayevych, E. V. Antipov and A. M. Abakumov; Solid State Ionics 357, p. 115468. Copyright 2020, with permission from Elsevier. Available from https://www.sciencedirect.com/science/article/abs/pii/S0167273820305221.

Table S23. Atomic coordinates and occupancies of the $K_6(VO)_2(V_2O_3)_2(PO_4)_4(P_2O_7)$ discharged to 1.8 V vs. K/K^+ (i=1.76mA/g) with isotropic thermal parameter U=0.0131(5) $Å^2$. Adapted from "Reversible electrochemical potassium deintercalation from >4 V positive electrode material $K_6(VO)_2(V_2O_3)_2(PO_4)_4(P_2O_7)$" // I. V. Tereshchenko, D. A. Aksyonov, A. Zhugayevych, E. V. Antipov and A. M. Abakumov; Solid State Ionics 357, p. 115468. Copyright 20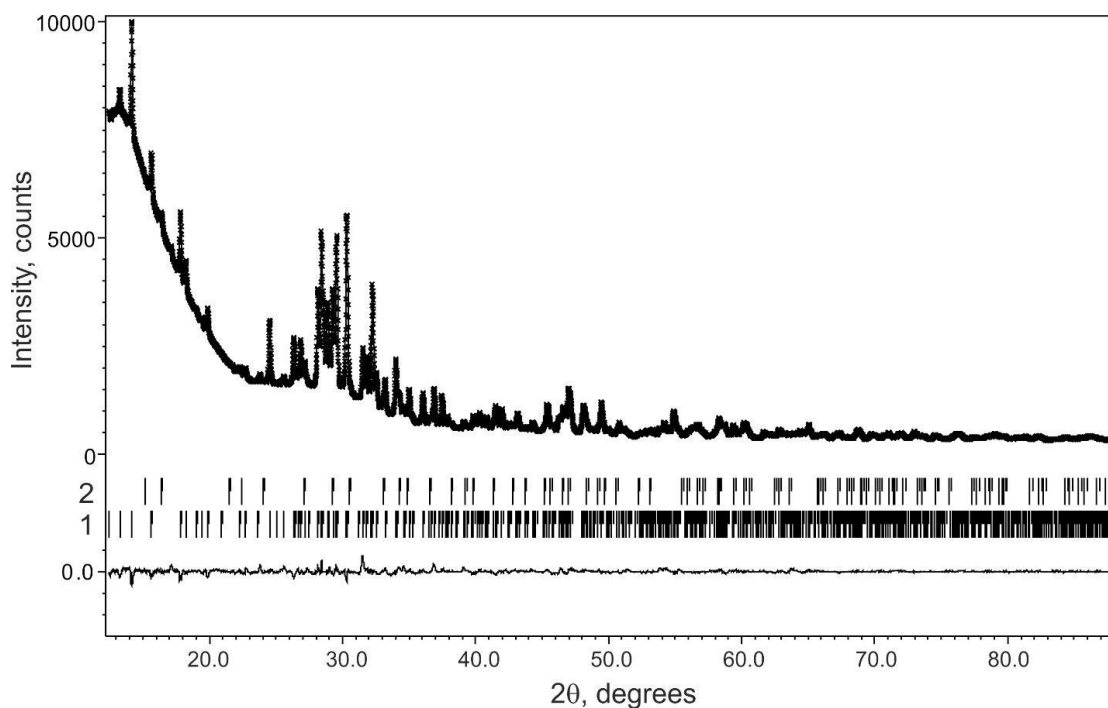20, with permission from Elsevier. Available from https://www.sciencedirect.com/science/article/abs/pii/S0167273820305221.

Label	Position	x/a	y/b	z/c	Occupancy
K1	8d	0.0958(4)	0.0076(2)	0.3358(2)	0.989(3)
K2	4c	0.1140(4)	0.25	0.5086(2)	1.062(5)
V1	8d	0.1600(3)	0.1243(2)	0.0800(2)	1
V2	4c	0.2416(4)	0.25	0.7594(2)	1
P1	8d	0.0375(3)	0.5986(2)	0.1204(2)	1
P2	4c	0.3653(5)	0.25	0.2468(3)	0.5
P3	4c	0.2741(5)	0.25	0.2638(3)	0.5
O1	4c	0.467(1)	0.25	0.7998(6)	1
O2	8d	0.3399(9)	0.0595(5)	0.0340(4)	1
O3	4c	0.225(1)	0.25	0.0383(6)	1
O4	4c	0.054(2)	0.25	0.323(1)	0.5
O5	8d	0.2148(6)	0.6444(4)	0.1665(3)	1
O6	8d	0.0503(6)	0.6119(4)	0.0140(2)	1
O7	8d	0.0272(7)	0.4872(3)	0.1440(3)	1
O8	8d	-0.1424(7)	0.6508(3)	0.1572(3)	1
O9	8d	0.2820(7)	0.1547(4)	0.2071(3)	1
O10	4c	0.394(1)	0.25	0.3519(3)	1

Table S24. Comparison of DFT-NEB migration barriers ΔE (eV) with two site energy barrier descriptors: migration barrier ΔE_{Born} (eV), calculated from site Born repulsive energy and change of average K-O distance between the saddle and initial points (Å) calculated using six nearest neighbor oxygen atoms; unit cell with space group $Pnm2_1$ was selected for calculations. Adapted from "Reversible electrochemical potassium deintercalation from >4 V positive electrode material $K_6(VO)_2(V_2O_3)_2(PO_4)_4(P_2O_7)$" // I. V. Tereshchenko, D. A. Aksyonov, A. Zhugayevych, E. V. Antipov and A. M. Abakumov; Solid State Ionics 357, p. 115468. Copyright 2020, with permission from Elsevier. Available   from

https://www.sciencedirect.com/science/article/abs/pii/S0167273820305221.

Hop designation	ΔE, eV	ΔE_{Born}, eV	Δd_{av}, Å
p5	0.82	1.86	0.26
p3	0.80	1.77	0.25
p4	0.38	1.28	0.20
p2	0.32	0.96	0.15
p6	0.27	1.11	0.17
p1	0.27	0.60	0.10